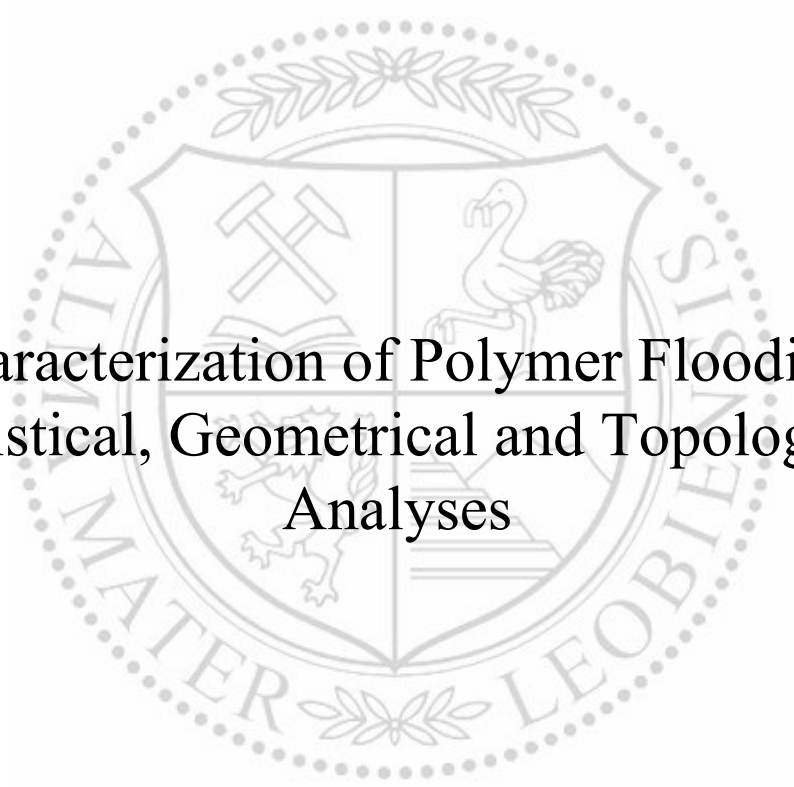




Chair of Reservoir Engineering

Master's Thesis



Characterization of Polymer Flooding:
Statistical, Geometrical and Topological
Analyses

Arash Nasiri

June 2020

Arash Nasiri

Master Thesis 2020 supervised by:

Univ.-Prof. Dipl.-Phys. Dr.rer.nat. Dr.Habil. Holger Ott

Dipl.-Ing. Ahmad Kharrat

Characterization of Polymer Flooding: Statistical, Geometrical and Topological Analyses

AFFIDAVIT

I declare on oath that I wrote this thesis independently, did not use other than the specified sources and aids, and did not otherwise use any unauthorized aids.

I declare that I have read, understood, and complied with the guidelines of the senate of the Montanuniversität Leoben for "Good Scientific Practice".

Furthermore, I declare that the electronic and printed version of the submitted thesis are identical, both, formally and with regard to content.

Date 25.06.2020



Signature Author Arash, Nasiri

Declaration

I hereby declare that except where specific reference is made to the work of others, the contents of this dissertation are original and have not been published elsewhere. This dissertation is the outcome of my own work using only cited literature

Erklärung

Hiermit erkläre ich, dass der Inhalt dieser Dissertation, sofern nicht ausdrücklich auf die Arbeit Dritter Bezug genommen wird, ursprünglich ist und nicht an anderer Stelle veröffentlicht wurde. Diese Dissertation ist das Ergebnis meiner eigenen Arbeit mit nur zitierter Literatur.



Arash Nasiri, 25 June 2020

In loving memory of my sister Azadeh (1985-2000)

Acknowledgements

I wish to express my sincere appreciation to my supervisor, Professor Holger Ott, for his creative ideas, immense knowledge, thoughtful feedback and continuous support. Without his persistent help and guidance, the goal of this project would not have been realized.

I acknowledge the Jungbunzlauer company that financed this research.

On a professional and personal level, I want to thank my co-supervisor, Ahmad Kharrat. He has supported me during my entire time and offered expert feedbacks.

Further, Pit Arnold has been available for a critical discussion where he provided many helpful advises.

Office managers Patrizia Haberl, Marlies Helbl, and especially Bettina Matzer, created the helpful and productive environment that made it possible to follow through the process of this thesis, for which I am very grateful.

I would like Peyman, Mohammad, Tim, Manuella, Michael, Maryam, Neda, Mostafa and Markus to know about my immense gratitude for all their support.

My deep and sincere gratitude to my family for their continuous and unparalleled love, help and support. I am grateful to you all.

Eventually yet importantly I wish to acknowledge the support and unconditional love of Mildred, you showed me some aspects of life to which I was blind! Thank you.

Abstract

Almost half a century has passed since the early innovative work on polymer flooding. In the meantime, to increase the recovery factor and as an attempt to better understand the transport phenomena in porous media, reservoir engineers started to combine various mathematical tools with traditional experimental investigations in the late eighties and early nineties. They began with geometry and statistics and later with topology. Only recently, have we seen studies that use mainly two of these aspects. Nonetheless, a combined study, gathering all four aforementioned subjects (polymer flooding, geometrical, topological and statistical analyses) was missing and this thesis is the pioneering effort on that.

The main objective of this thesis is to conduct a comprehensive analysis of polymer flooding, owing to the observation that recovery factor alone, as the main traditional criterion to evaluate polymer flooding, does not provide consistent results in microfluidics. To achieve a complete view, the evaluation consists of three categories of statistical, topological and geometrical analysis. These categories cover different aspects of the flooding including its stability, efficiency and phases mobility.

Regarding the methodology, sequences of polymer flooding and water flooding were conducted mainly in two rates of 0.01(High rate/HR) and 0.0019(Low rate/LR) [ml/hr] as well as two phases of secondary and tertiary flooding in a uniform micromodel to control the effect of pore network geometry. All these experiments were performed with crude oil of the target field from Vienna basin, which has a high viscosity and TAN number. Flooding records (duration, injection rate and polymer concentration) as well as images of the micromodel were collected as the primary experimental data and later processed to extract more data. The extraction process was mainly done by image processing and image analysis that proved to be extremely useful and necessary.

As for the findings, a new quantitative description of the observed flow regimes in secondary flooding was developed by plotting the RF versus fractal number. The fractal number was extracted using morphological image analysis and it corresponds to the complexity of the perimeter of the areal sweep. The author observed that above a critical polymer concentration the stabilizing effects of polymer agent overcomes the instability caused by viscous or capillary fingering. Furthermore, in the tertiary flooding, ganglion dynamic flow regime has been observed and characterized by employing Euler characteristic. It has been noted that oil clusters become immobile around a higher oil saturation for lower injection rate.

As the result of this work, a better insight into the displacement patterns of the flooding phenomena has been achieved. Moreover, these findings should and could be used to combine with traditionally modelling techniques of fluid flow to increase the accuracy of the model simultaneously with the reduction of the computational expense. For example, by running the model over a representative elementary volume.

Zusammenfassung

Fast ein halbes Jahrhundert ist seit den frühen innovativen Arbeiten zur Polymerflutung vergangen. In der Zwischenzeit begannen die Lagerstätten-ingenieure Ende der Achtziger und Anfang der Neunziger Jahre mit verschiedenen mathematischen Werkzeugen zu arbeiten, zunächst mit Geometrie und Statistik, und später mit der Topologie. Erst in jüngster Zeit haben wir Studien gesehen, die hauptsächlich zwei dieser Aspekte verwenden. Dennoch fehlte eine kombinierte Studie, die alle vier oben genannten Themen (Polymerflutung, geometrische, topologische und statistische Analysen) zusammenfasst, und diese Masterarbeit ist der wegweisende Ansatz dazu.

Aufgrund der Beobachtung, dass der Gewinnungsfaktor allein als traditionelles Hauptkriterium zur Bewertung der Polymerflutung in der Mikrofluidik keine konsistenten Ergebnisse liefert, ist es das Hauptziel dieser Arbeit eine umfassende Analyse der Polymerflutung durchzuführen. Um einen vollständigen Überblick zu erhalten, besteht die Auswertung aus drei Kategorien der statistischen, topologischen und geometrischen Analyse. Diese Kategorien decken verschiedene Aspekte der Flutung ab, einschließlich ihrer Stabilität, Effizienz und Phasenmobilität.

Was die Methodik betrifft, so wurden Sequenzen von Polymerflutung und Wasserflutung hauptsächlich in zwei Raten von 0,01 (hohe Rate /HR) und 0,0019 (niedrige Rate / LR) [ml/hr] sowie zwei Phasen der sekundären und tertiären Flutung im einheitlichen Mikromodel durchgeführt, um den Effekt der Porennetzgeometrie zu kontrollieren. Alle Experimente wurden mit Rohöl des Zielfeldes aus dem Wiener Becken durchgeführt, das eine hohe Viskosität und TAN-Zahl aufweist. Flutungsaufzeichnungen (Dauer, Injektionsrate und Polymerkonzentration) sowie Bilder des Mikromodells wurden als primäre experimentelle Daten gesammelt und später verarbeitet, um weitere Daten zu extrahieren. Der Extraktionsprozess wurde hauptsächlich durch Bildverarbeitung und Bildanalyse durchgeführt, die sich als äußerst nützlich und notwendig erwiesen.

Was die Ergebnisse betrifft, so wurde eine neue quantitative Beschreibung der beobachteten Abflussregime bei sekundären Flutungen entwickelt, indem die RF vs. Fraktalzahl aufgetragen wurde. Die Fraktalzahl wurde mittels morphologischer Bildanalyse extrahiert und entspricht der Komplexität des Perimeters der Arealabtastung. Der Autor beobachtete, dass oberhalb einer kritischen Polymerkonzentration die stabilisierende Wirkung des Polymermittels die durch viskose oder kapillare Griffweise verursachte Instabilität überwindet. Darüber hinaus wurde bei der tertiären Flutung ein gangliodynamisches Strömungsregime beobachtet und durch die Verwendung der Euler-Charakteristik charakterisiert. Es wurde festgestellt, dass Ölcluster bei höherer Ölsättigung und niedriger Injektionsrate unbeweglich werden.

Als Ergebnis dieser Arbeit konnte ein besserer Einblick in die Verdrängungsmuster der Flutungsphänomene gewonnen werden. Darüber hinaus können und sollten diese Erkenntnisse mit traditionellen Modellierungstechniken der Fluidströmung kombiniert werden, um die Genauigkeit des Modells zu erhöhen und gleichzeitig den Berechnungsaufwand zu reduzieren. Zum Beispiel, indem das Modell auf ein repräsentatives Elementarvolumen angewandt wird.

Contents

Chapter 1. Introduction	1
Chapter 2. Literature Review	3
2.1. Polymer Flood	3
2.2. Xanthan	4
2.3. Wettability Alteration During Flooding.....	6
2.4. Microfluidics.....	7
2.5. Statistical, Topological and Geometrical Analysis and their Applications in Reservoir Engineering	9
Chapter 3. Experimental Apparatus	22
3.1 EOR Platform.....	22
3.2 Microscope.....	23
3.3 Injection Equipment.....	24
Chapter 4. Experimental Methodology	25
4.1 Preconditioning	25
4.2 Conducting Experiments.....	27
4.3 Data Acquisition	28
4.4 Calculations.....	33
4.5 Interpretations of instabilities.....	42
Chapter 5. Results and Discussion	44
5.1 General Description of the Experiments	44
5.2 Statistical Analysis	46
5.3 Geometrical Analysis and Fractal Dimensionality	50
5.4 Topological Analysis	58
Chapter 6. Conclusion	66
6.1 Summary	66
6.2 Further Work.....	66
Chapter 7. References	71
Chapter 8. Appendix	79
8.1 Visualization of All Scenarios	79
8.2 Polymer Retention Experiments	84

Nomenclature & Abbreviation

A	Cross-sectional area of the uniform porous network		
C_p^*	Critical polymer concentration		
C_p	Polymer concentration		
D_B	Box counting dimension		
D_f	Fractal Dimension /Dimensionality/ Number		
D_{front}	Fractal number of the outer perimeter of the areal sweep zone		
D_N	Normal fractal number	AS	Areal sweep
D_{NW}	Fractal number of non-wetting phase	BT	Breakthrough
D_o	Fractal number of oleic phase	DEV	Deviation from the dimension of the space
D_w	Fractal number of the water phase	EOR	Enhanced Oil Recovery
M	Mobility ratio	CDC	Capillary Desaturation Curve
M_u	Viscosity ratio	DLA	Diffusion Limited Aggregation
N_c	Capillary Number	HR	High rate. [0.01 ml/hr]
$P(s)$	Cumulative cluster size distribution	IP	Invasion Percolation
$W(s)$	Volume weighted cluster size distribution	IR	Injection Rate
S_{ors}	Remained oil saturation inside the swept zone	LR	Low rate [0.0019 ml/hr]
v_{Darcy}	Darcy velocity	$MMDa$	Million Dalton
z	Coordination number	MPM	Modified Percolation Model
Γ	Shear rate	MUL	Montan University of Leoben
λ_D	Mobility of Displacing Phase	POF	Polymer Flooding
λ_d	Mobility of Displaced Phase	RCZ	Radical Changes Zone
σ	Standard Deviation	REA	Representative Elementary Area
χ_{cl}	Euler Characteristic for a cluster	REV	Representative Elementary Volume
χ_N	Volume scaled Euler Characteristic	RF	Recovery Factor
χ_{PS}	Euler Characteristic for the pore space	WF	Waterflooding

Chapter 1

1. Introduction

Decades have passed since the peak of giant field discoveries, during which the industry has been gradually yet continuously shifting toward focusing on the increase in ultimate recovery (UR) for which various enhanced oil recovery techniques have been implemented. Polymer flooding has been conducted since 1970 with proven results (1). The idea behind using a polymer as an EOR agent is to decrease the mobility ratio, which in turn leads to higher volumetric sweep efficiency. This is achieved mainly by increasing the injection fluid viscosity (2). Just like other EOR processes, polymer flooding has some limitations in application. Thus, it is important to conduct screening to candidate proper reservoirs in order to achieve the best of polymer flooding and avoid loss of time and capital. The screening criteria has been achieved mainly by experience and hence, accompanied by potential uncertainties and room to manoeuvre with respect to polymer concentration and injection rate.

In order to find the optimum features of polymer flooding this research delves into the statistical, topological and geometrical status of different polymer flooding scenarios by means of cluster analysis, Euler characteristic (χ) and fractal dimension (D_f) respectively. So that different scenarios could be compared, and an optimum one would be chosen through investigation of EOR potential of the system, the breakthrough time remaining as well as residual oil saturations and front stability. To accomplish this task, the potential of microfluidics will be employed and the gathered data will be analysed further using image processing and analysis.

1.1. Background and Context

Polymer flooding is considered to be a chemical mechanism during the tertiary phase of EOR process. Almost half a century has passed since the early innovative work on polymer flooding was done by Pye (3), Sandiford (4), Mungan (5) and Gogarty (6). Meanwhile, to increase the recovery factor and as an attempt to better understand the transport phenomena in porous media, reservoir engineers started to combine various mathematical tools with traditional experimental investigations in the late eighties and early nineties. They began with geometry (7) (8) and statistics (9) and later with topology (10). However, only recently we have seen the studies that use mainly two aspects, including statistical and geometrical analyses (11) or statistical and topological analyses (12) (13) (14) (15). Nonetheless, a combined study, gathering all four aforementioned aspects (polymer flooding, geometrical, topological and statistical analyses) was missing and this thesis is the pioneering effort.

The statistical tool includes cluster size distribution and a Lorenz plot as well as REV analyses. The former two investigate the inequality of the cluster sizes and their distribution to explore the EOR potential. There will be an investigation of fluid topology consisting of its complexity and connectivity both of which will be looked into, using the geometrical tool of fractal dimension and topological tools of Euler characteristic and saturation. This information will be then used to find out the correlation among χ , D_f , RF and polymer concentration.

1.2. Scope and Objectives

The general scope of this thesis is to characterize polymer flooding with mathematical tools including integral geometry, and statistics. The physical motivation behind the characterization is provided by four Minkowski functionals. These are respectively M_0 , M_1 , M_2 and M_3 . M_0 is the volume, M_1 is the

interfacial area, M_2 is the average curvature of the surface and M_3 is the total curvature. Micromodels are considered as 2D spaces, hence M_0 and M_1 are respectively translated into saturation of the oil and the perimeter of the interface between displacing phase and the oil. To describe the topology of the fluid phase in 2D space, three functionals are enough. We use M_3 as the third one which is related to the connectedness of the structure and is quantified by Euler Characteristic (χ). To gather this data image processing and analysis should be employed.

Another main objective is to have a better insight into the displacement patterns for different displacement characteristics. Furthermore, these findings should and could be used to combine with traditional modelling techniques of fluid flow to increase the accuracy of the model simultaneously with the reduction of the computational expense. For example, by running the model over a representative elementary volume.

Chapter 2

2. Literature Review

This chapter aims to present the reader with a background on the concepts being used by the author.

2.1. Polymer Flood

In general, polymer flooding is considered to be a chemical mechanism during the tertiary phase of EOR process. Polymers have more applications than merely an EOR agent in oil industry, however the idea behind using them as an EOR agent is to decrease the mobility ratio, which in turn leads to higher volumetric sweep efficiency. This is achieved mainly by increasing the injected-fluid viscosity. In addition, some polymers can reduce water relative permeability (2), that mathematically could be described as the following, where the mobility ratio (M) is calculated before the breakthrough:

$$\lambda_D = \left(\frac{k_w}{\mu_w} \right) \Rightarrow M = \left(\frac{\lambda_D}{\lambda_d} \right)$$

Although in the above relationship, the role of oil viscosity is not stressed out, it does play an important part in the benefit of polymer flood depending on the flooding conditions. Low oil viscosity and hence low mobility ratios often allow small improvements by polymer flooding as compared to waterflooding, while at high oil viscosities the reduction in the mobility is considerable (16).

Just like other EOR processes, polymer flooding has some limitations in application. Hence, it is important to conduct a screening to nominate proper reservoirs to achieve the best of polymer flooding and avoid loss of time and money. A screening criterion then is reviewed in [Table 1](#) and

[Table 2](#), where oil properties, as well as reservoir characteristics, play an important role in choosing the proper EOR technique.

Table 1: Screening criteria for some EOR methods based on oil properties (17).

Process	Gravity [°API]	Viscosity [cp]	Composition	Oil Saturation
Water flooding	> 25	< 30	N.C.	> 10% mobile oil
Carbon dioxide	> 26	< 15	High % of C ₅ -C ₁₂	> 20% PV
Surfactant/polymer	> 25	< 30	Light to intermediate desired	> 30% PV
Polymer	> 25	< 150	N.C.	> 10% PV mobile oil
Alkaline	13-35	< 200	Some organic acids	Above waterflood residual
Combustion	< 40	< 1000	Some asphaltic components	> 40% - 50% PV
Steam flooding	< 25	> 20	N.C.	>40% - 50% PV

Note: PV=pore volume; N.C.= not critical

Table 2: Screening criteria for EOR methods based on reservoir characteristics (17).

Process	Formation type	Net Thickness [ft]	Average Permeability[mD]	Depth[ft]/Temp[°F]
Water flooding	Sa or Ca	N.C	N.C.	N.C./N.C
Carbon dioxide	Sa or Ca	Thin unless dipping	N.C.	> 2000 / N.C.
Surfactant/polymer	Sa preferred	> 10	> 20	< 8000 / < 175
Polymer	Sa preferred; Ca possible	N.C.	> 10 (normally)	< 8999 / < 200
Alkaline	Sa preferred	N.C.	> 20	< 9000 / < 200
Combustion	Sand or Sa with high porosity	> 10	> 100	> 500 / > 150
Steam flooding	Sand or Sa with high porosity	> 20	> 200	300-5000 / N.C.

Note: N.C.= not critical; Sa= Sandstone; Ca=Carbonate

The criteria to select the polymer type for flooding include good thickening behaviour, high water solubility, low retention, high stability (shear, chemical and biological) and good transport properties in permeable media (2). Many polymers have been used for the flooding process among which Xanthan gum and partially hydrolysed polyacrylamides (HPAM) are most famous. This study used Xanthan gum and thus, it focuses on this polymer. Xanthan belongs to the category of Polysaccharides (Biopolymers) and is preferable in polymer flooding because the viscosity of its polymer solution is not influenced by temperature and pH changes neither presence of salt (18). On the other hand, it is susceptible to Bacterial attack.

2.2. Xanthan

Xanthan gum is among the polymers with major applications in oil recovery techniques (19). Although it is more expensive than HPAM per unit, it is more effective in mobility reduction. Xanthan is being produced through a bacterial fermentation process by bacterium *Xanthomonas campestris* and will be susceptible to bacterial attack once injected into the reservoir. However, this disadvantage is neutralized by its resistance to degradation from brine PH, salinity and hardness (2). As for its molecular structure, studies estimate the persistent length of Xanthan chain to be 60 [nm] for single-stranded and 150 [nm] for double-stranded xanthan (20). Its molecular weight normally varies between 0.4 to 15 MMDa (million Dalton) (21). In a high salinity environment on the other hand, Xanthan molecules tend to form a linear unbranched structure with uniform thickness (20). This formation may cause lower/higher adsorption depending on the salinity and PH of the brine (22). This effect on Flocon can be seen in [Figure 1](#). The similarity between Flocon and Xanthan causes the same behaviour.

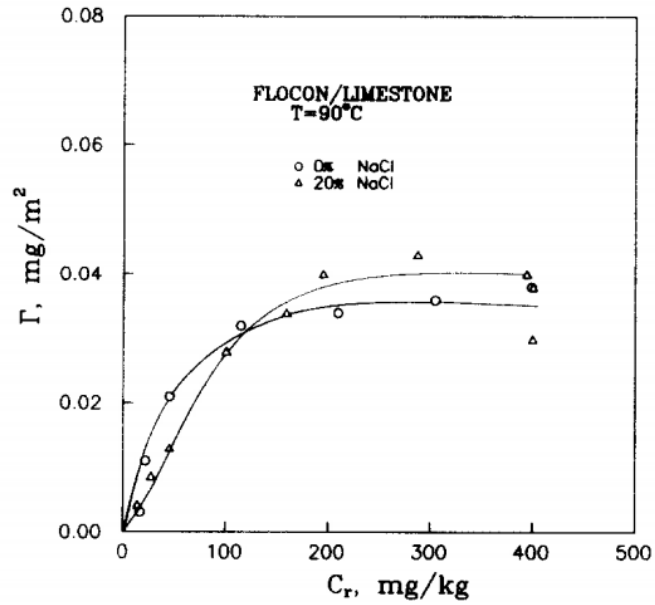


Figure 1: Effect of Salinity on FLOCON adsorption. (PH=7.9 , T=90 °C)

Xanthan's structure can be seen in [Figure 2](#).

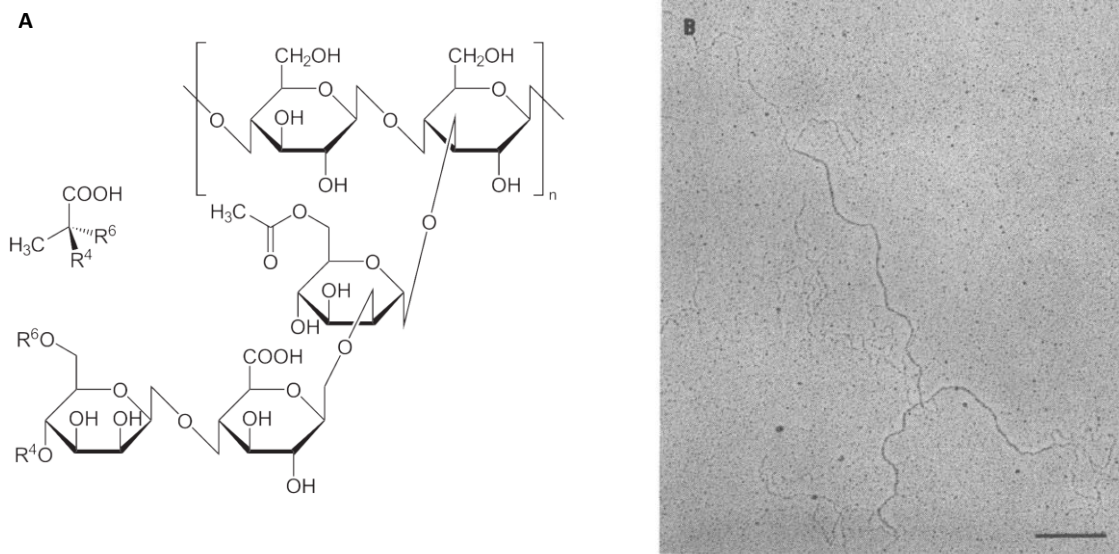


Figure 2: **A)** Structure of Xanthan Gum (23) **B)** Representative electron micrograph of Xanthan (20)

As for its solution rheology, the viscosity is a function of xanthan concentration and as expected temperature. It shows a strong shear thinning behaviour which is the result of uncoiling and aligning of polymer chain when exposed to flow (24). The following figure shows the aforementioned behaviour.

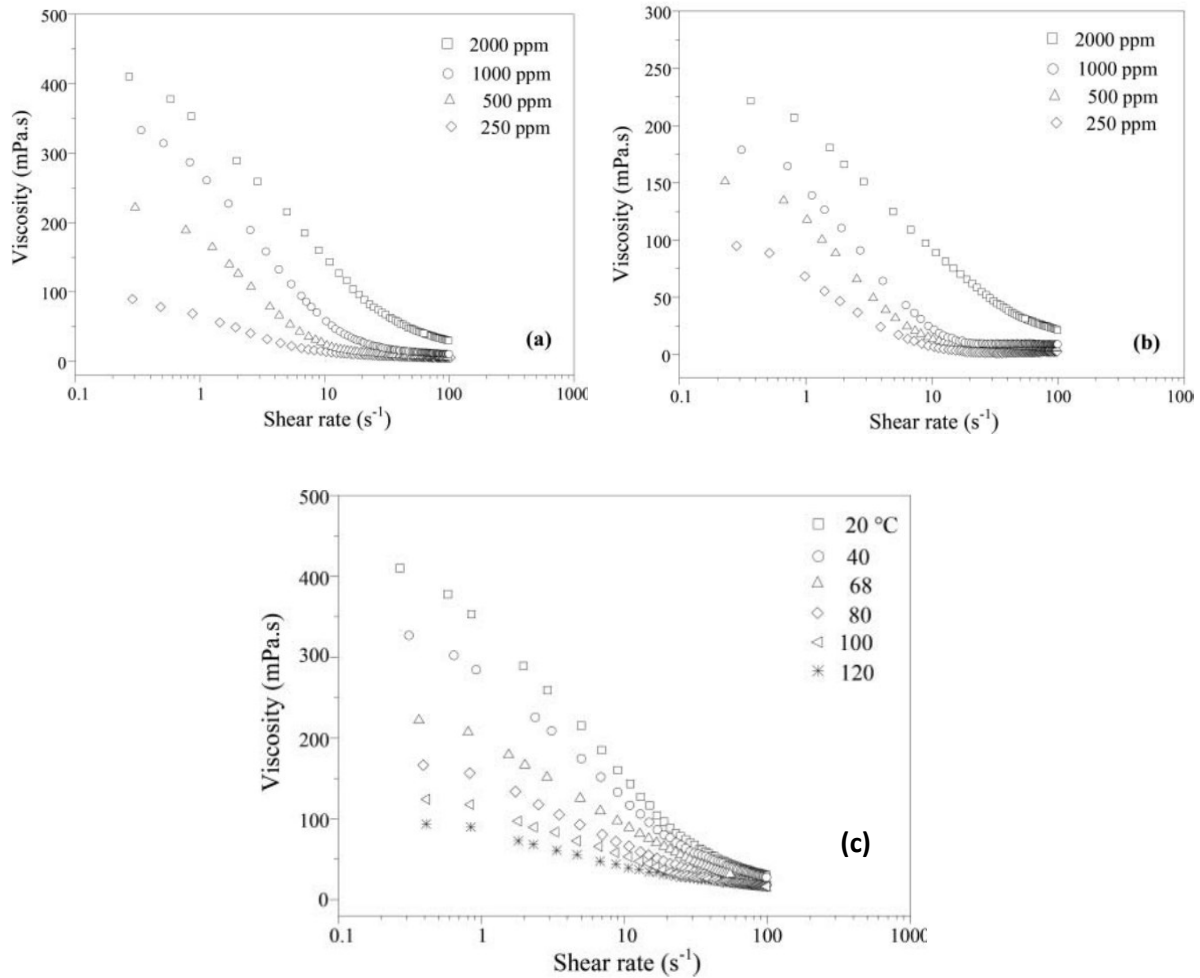


Figure 3: Viscosity as a function of shear rate for Xanthan in water solution @ (a) 20° C , (b) 68° C. (c) Viscosity as a function of temperature for the concentration of 2000 ppm (24).

Methods to measure retention

Conventionally, the general approach to determine polymer retention was first conducting flooding tests, then measuring the effluent polymer concentration and eventually using material balance (25). This technique depends heavily on the accuracy of measuring the polymer concentration in the outlet flow. During recent years simultaneously by the development of the micromodels and computers, new image analysis techniques have been introduced to the laboratories to quantify polymer retention. These image analysis techniques include thresholding, determination of the value of specific colour (normally green), binary image subtraction, sensitivity analysis, and sometimes using tracer particles (26) (27) (28). There are other techniques as well like ultra-visible spectroscopy being able to measure the concentration of polymer and hence used in retention measurements (29).

2.3. Wettability Alteration During Flooding

There have been attempts to relate the wettability alteration to Euler characteristic, hence the topic is subject to a brief review.

Wettability is a concept belonging to the interaction of rocks and fluids in reservoirs. It is a principal factor that controls relative permeability. Wettability alteration could happen during flooding. What governs the change is a combination of environmental factors, fluid properties and rock mineralogy, including the *pH* of the fluids, the retention of the polymers (30) (mainly adsorption (31)), salinity and temperature of the reservoir fluids, and the electrostatic of the reservoir rock. Changing the wettability

is a promising method to produce more oil in some EOR techniques including low salinity flooding and alkali flooding (2).

Considering the fact that phase connectedness, wettability, and fluid distribution are related through capillary pressure curve, it is not a surprise that wettability changes could be characterized using the Euler characteristic (χ) (15), however, to link wettability directly to χ , might be distorting and oversimplifying the physical relationship (13).

2.4. Microfluidics

Microfluidics is the science of studying fluids that are restricted to a specific predefined sub-millimetre dimension and geometry. This science is a wide area covering mathematics, physics, engineering, biotechnology and other sciences (32). The geometry is provided by micromodels which are artificial 2D models of a porous medium and are commonly used to investigate and visualize small-scale physical, chemical, and biological processes. They were initially developed in 1952 to analyse the fluid flow behaviour in a porous medium and later to investigate processes pertinent to the oil and gas industry as well as mathematics and other sciences. Cases in points are different approaches to the effect of grain roundness (fractal dimension in mathematic) and diffusivity (percolation dimension and Labyrinth pattern by mathematicians) (33) (34).

The principal opportunity of using micro models is the fact that it makes it possible for the researcher to watch the medium directly (mainly porous in our case) and investigate one or several features of interest in fluid flow. Moreover, the topology and geometry of the design can be specified. Hence micro models are made of transparent materials such as glass, quartz or polymers and come with different sizes among which those with pore sizes less than one mm is essential to study two-phase flow. The overall size of micro models is normally on centimetre-scale and as can be seen in [Figure 19](#) there should be an inlet and one outlet (35). On the other hand, as a disadvantage, unlike a real porous medium, “bicontinua (existing of two continues phase concurrently) cannot exist in 2D dimensions” (36).

Image Analysis

Image analysis is the science and art of gaining useful and meaningful information from images (37). To achieve this goal, it employs mainly digital software in order to execute a variety of commands regarding processing an image. Depending on the area of investigation, there are many software packages to work with, among which MATLAB and ImageJ are mainly used by researchers in the oil industry. The included algorithms are too many to be mentioned here. However, the used functionalities are listed in [Table 3](#), and include morphological and topological analysis of the images. Afterward, using the results, a statistical analysis can be carried out.

The results of the experiments depend heavily on the accuracy of the executed image processing operations. Hence, it is significant to understand the related mathematical concepts to be able to choose the correct setting for the processing operations. The proper setting will be mentioned in the following chapters; however, the concepts are discussed here.

Erode and dilate are considered as the most basic morphological (shape depending) image processing operations. The first one adds pixels to the boundary of an object while the latter one removes pixels on object boundaries. Researchers in the oil department of MUL use morphological opening (erosion followed by dilation) to remove artefacts (38) (39). This thesis followed a similar procedure.

Table 3: Image processing commands and operations, as well as their mathematical background, having been used in this thesis (40) (41) (42) (37) (43).

Example of commands/Processes	belongs to the following operation	Mathematical concept behind	Details
Image Stitching	Image Registration Operations	Fourier Shift Theorem and translation computation	
Erode/Dilate	Morphological Operations	Pixel Removal/Addition	Artefact removal
Filters>Minimum		Pixel Removal	Artefact removal
Make Binary		Thresholding and Logical Comparison	Simplicity
Subtract Background (SB)		Mainly Rolling Ball Algorithm Using Pixel Subtraction	Background Normalization
Kill borders		-	Residuals detection
Fill holes		-	Areal sweep detection
Area filter		Filtering Operations	Gaussian filter
Area Fraction (AF)	Area Statistics	The Percentage of Non-Zero Pixels	Used To Calculate Recovery Factor
Fractal Dimension	Topological Analysis	$\frac{\log(\text{number of self-similar pieces})}{\log(\text{magnification factor})}$	Used to investigate front complexity and propagation

As for the ‘Subtract Background’ (SB) process, the quality of images is a function of environmental conditions (like the intensity and type of light in the environment) as well as the digital setting of the capturing device. The SB process helps to remove or diminish the effect of artefacts caused by environmental sources to remove the smooth continuous background. This is done by considering a third dimension (height) for a 2D grayscale image by image value at every point. These dimensions then create a surface where the height equals to the gray level of the pixel at position x, y in the image. The average value of this background then can be estimated and be subtracted from the original image. The rolling ball algorithm considers a solid sphere (rolling ball) that can move freely beneath the surface of the picture constrained by the upper surface. The ball rolling underneath the surface will smooth the background by removing/adding pixels to the contact point. This depends on the diameter of the ball of course. Since it should be chosen in a way to affect the background but not the peaks since peaks represent non-background elements in the picture. A schematic representation of the rolling ball algorithm, as well as a sample of its gained result, are demonstrated in the following picture.

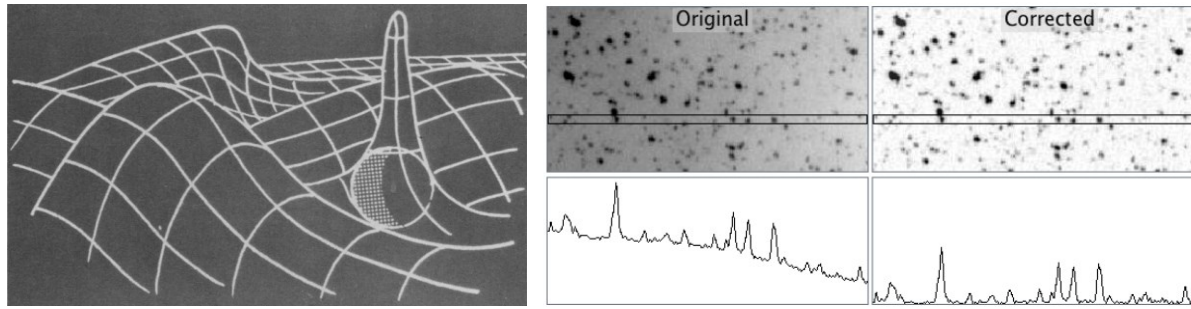


Figure 4: **Left)** Schematic representation of the rolling ball algorithm. The ball smooths the background counter but will not penetrate the peaks, hence not affecting the separated items in the original image. The radius of the ball should be set bigger/equal than/to the size of the largest object that is not part of the background (44). **Right)** An example of the result of implementing the rolling ball algorithm on an image.

Regarding image stitching, it is one of the most important steps affecting the quality of the results. It is a necessary step since normally the image capturing device cannot scan the entire micromodel view at the respectively high image resolution in one image, hence different images will be taken and then merged into one another in the process of stitching to include the entire medium. To reach the optimum setting to stitch the images can be very time consuming as well as complex. All the factors that affect the stitching process should be taken into consideration in order to ensure the accuracy of the results. Reliable work has been done to optimize the stitching process by Preibisch, et al, where the authors use the Fourier transform-based phase correlation method to compute all possible translation between pairs of images to minimize the overlap error yielding into the best automatically achievable results. This method has been used by ImageJ software under “Image Stitching” plug-in (40) (43). The other inherent issue of stitching in displacement experiments is that it places limitations on the injection rate. Because the injection rate must be low enough for the image capturing device to be able to capture the front propagation, otherwise, it causes a fatal error. To shed more light on the matter, it should be mentioned that there are two types of error causing by the stitching process. One is inherent and the other is non-inherent. The latter is the error caused by overlapping sequential images in the merging process. The former on the other hand is the blur displacing front caused by a fast injection rate. Indeed, the rate of capturing images was too fast for the camera to be recorded in one image. The first error can be solved using the correct stitching technique and optimum configuration, but nothing can be done as for the latter case. The issues of this process, as well as their sample images, are covered in **Chapter 4**.

As regards area statistics, area fraction is the main image analysis tool to calculate the saturations in displacement experiments. For the binary image, provided that the grains and the pore volume have different colours (grains as white and the pore volume as black in 100% oil saturated chip), area fraction is the percentage of non-zero pixels referring to the pore volume (40). However, once water is introduced into the domain, depending on the experiment workflow and thresholding pixel value, the non-zero pixel could be associated with the oleic phase or the aquatic phase.

As to mathematical analyses, which are the main tools being used in this thesis, they are discussed in detail in what follows next.

2.5. Statistical, Topological and Geometrical Analysis and their Applications in Reservoir Engineering

Topology, as a mathematical discipline, is the science of studying the properties of topological spaces and its fundamental features. Indeed, topology is a branch of mathematics that treats place directly the way algebra treats magnitude (45). Two main concepts being used in reservoir engineering and in microfluidics are the Euler number and fractal dimension. These concepts can be used to describe pore-

scale displacement (46) and trapping by analysis of cluster topology and pore fluid geometry respectively. The dependency of residual non-wetting phase with pore topology has been investigated by Pathak et al. (2009). They used the concept of genus (a topological invariant describing number of distinct holes in a porous medium) and concluded that pore topology is as important as pore geometry to determine residual non-wetting saturations (47). Afterward, the concept has been used many times by different researchers. This includes studies in pore connectivity and topology on gas productivity (48), pore topology alteration due to removal of the dead oleic phase (49) and scale dependency of pore topology (50). One of the studies having been used by this thesis is done by Ott (2015). Concerning this thesis's area of interest, his work concluded that fluid topology has a connection with the de-saturation curve of the system. Moreover, he presented a methodology describing the connection between desaturation and pore-scale fluid topology and giving an insight how capillary number changes with system size. ***In general, statistical cluster analysis as well as topological and geometrical analysis help reservoir engineers to determine the EOR potential of the reservoir while better understanding the displacement processes.*** This can be seen in [Figure 5](#), wherein a region of interest, a 3D representation of fluid saturation using μ CT imaging as well as its cluster size analysis curves have been shown. The 2D volume can be seen as a fractal system which is characterized by its dimension. A true fractal system, however, has no scale. It is a fractal distribution where there is no preferred cluster size. It means there is an equal amount of oil sited in small clusters as is in large clusters. In the cluster analysis curve, this behaviour will perfectly fit into a straight line (depending on the system characteristics it has different fitting exponent; τ), but as can be seen by [Figure 5](#))right in real systems at a certain point, the distribution is deviating. In this specific case, it is deviating toward right, meaning that larger oil clusters contain more oil in comparison to the small clusters that are very difficult to mobilize. Hence, this system has EOR potential. On the other hand, if it deviated toward left then it would have suggested that the majority of oil is sited in small clusters. Difficult to produce, the system then possessed no or very few EOR potential.

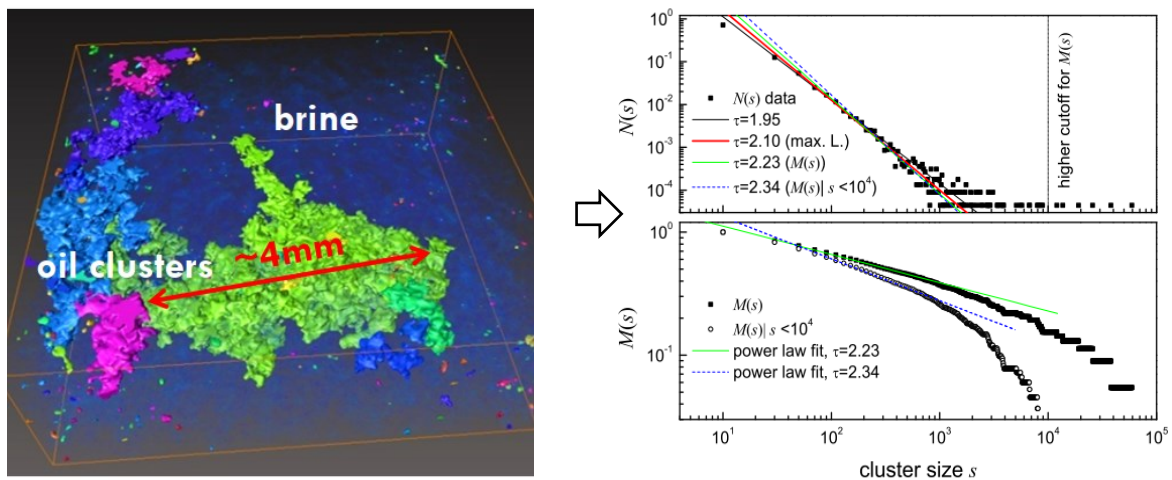


Figure 5: **Left)** 3D representation of fluid saturations using μ CT imaging. **Right)** Normalized cluster volume (top), and cumulative distribution (bottom) for different regions of interest (51).

In a nutshell, neither statistics nor topology alone is enough to describe the porous medium, since it is not the geometry of the medium for which we are looking, but the geometry of the fluid within it (52). However, the combination of statistical, topological and fractal analysis, using their tools including cluster analysis, Minkowski functionals (MF) (Euler characteristic in particular) and fractal dimension not only will eventually replace the role wettability is playing nowadays for reservoir engineers but in

essence, they provide powerful means to study the EOR potential of the porous medium and fluid mobility as well as predict and interpret displacement processes (15).

Giving this introduction, the previously mentioned tools will be discussed now.

2.5.1. Euler Characteristic (χ)

Topology is quantified using Minkowski functionals (MFs). Topological tools have been used to study a wide range of majors from the distribution of galaxies to phase transition and percolation phenomena. The concept was developed by Hadwiger's theorem, based on the fact that topology alone was not enough to unequivocally describe a system or an object. Hadwiger showed that "in an n-dimensional space there exists a basis of n+1 intrinsic values quantifying geometry" (14). In a 2D dimension, these functionals are the area, the perimeter and the Euler characteristic (53).

Figure 7 shows their mathematical expressions. In a 3D dimension, the average curvature will be required as well, but as mentioned, microfluidics experiments are considered 2D.

Euler characteristic can be defined as $\chi = Objects - loops + cavities$ (54). Important to notice is that it is related to the connectivity of a system. The concept can be used to describe the topology of the pore space (like in the work of Blunt (15)) or the fluid phases (like in the work of Pathak et al. (47) and others (13) (14) (55)). **We should be careful not to confuse these two separate concepts. In this thesis, we are interested in fluid phases in porous media.**

Apart from the calculation of χ for the fluid phase, due to the homogeneous structure of uniform micromodel, calculating theoretical values for χ_{ps} (Euler characteristic for pore space) should not be problematic. Blunt used the graph theory to find χ_{ps} and define an intensive χ value. While the definition of an intensive value is meaningful for the pore space due to its continuity, it makes no sense to use it for characterization of residual phase. However, we can always calculate and plot these values to extract useful information.

$$\chi_{ps} = n_p - n_t; \quad \chi_V = \frac{\chi_{ps}}{V};$$

$$\chi_V \approx \frac{1}{l^3};$$

n_p , n_t and l are respectively, number of pores, throats and pore diameter. The estimation is valid only for a structure where each pore has at least two bounding throats (15).

In order to determine the value of χ for an arbitrary shape another equation is being used, in which Betti numbers are employed. β_1 is the key to the connectedness parameter. In plain explanation, it tells us how many connections can be broken without the connectivity to be abandoned. Examples of the values of Betti numbers for a solid and a hollow object are given in Figure 6.

$$\chi = V - E + F - O$$

$$\chi = \beta_0 - \beta_1 + \beta_2$$

Equation 1: The mathematical expression of Euler characteristic. Up is the specific expression and down is the generalized definition (Euler-Poincare equation). β is the Betti number where β_0 is the number of discrete objects in a porous medium (in this thesis number of isolated oil clusters). If the pores are interconnected, then $\beta_0=1$. β_1 is the number of loops that can be omitted without changing the connectivity. β_2 is the number of internal cavities. (55)

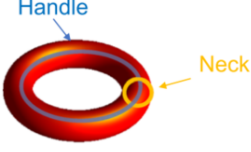

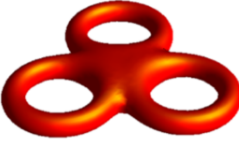
	(Objects, Loops, Cavities)		
			
Solid Object	(1,1,0) $\chi = 0$	(1,2,0) $\chi = -1$	(1,3,0) $\chi = -2$
Hollow Object	(1,2,1) $\chi = 0$	(1,4,1) $\chi = -2$	(1,6,1) $\chi = -4$

Figure 6: Basic topological properties and the resulting Euler characteristic for the following solid and hollow objects: torus, double torus and triple torus ($\beta_0, \beta_1, \beta_2$) (14).

χ is dimensionless and independent of geometry. Its calculation is not cumbersome nor computationally expensive for 2D spaces and is available as the ‘connectivity plug-in’ by ImageJ. In microfluidic experiments, we need to know the phase for which the Euler characteristic is being calculated. The general methodology is to calculate it for the non-wetting phase (56).

There is a relationship between cluster mobilization and fragmentation and χ . Presence of the isolated clusters can lead to greater values of χ . Then comparing experiments in regard to the value of their χ will help us to distinguish systems from one another better. A case in point could be quantifying the differences between two polymer flood experiments trying to find the best criteria of polymer concentration in regard to pore and residual oil cluster size distributions. As for the EOR potential, however, χ is not a good measurement, because it does not differentiate among different sizes of the oil clusters. We need to make χ sensitive to the size, simply because a major oil cluster has more potential to be produced, unlike the small ones that are very difficult to mobilize. Then in this thesis, we will follow the methodology that was proposed recently by Ott et al. to calculate the χ for clusters, so-called χ_{cl} (13). This is further discussed in [5.4.1 Euler Characteristic](#).

The absolute value of χ can also provide useful information. It can be interpreted in different ways, yet all meaning the same thing. One interpretation could be that large negative values of χ correspond to non-wetting phase occupying most of the voids (15). Another explanation tells us that during the waterflooding in both an oil-wet and a water-wet system the values of χ increases (shifting from large negative values to a smaller negative value). This is due to the large oil clusters being broken down into smaller isolated clusters. The process itself consists of two phases. The first phase happens during the initial stages of the imbibition process, where the oil saturation decreases only little and oil production is due to swelling of the wetting phase. The second stage occurs once the large oil clusters are being disconnected and broken down. In the latter phase, there is a large decrease in oil connectivity which in turn results in dramatic oil saturation decrease and Euler characteristic increase (56).

Full Topological Description

Description by the Minkowski Functionals:

$$M_0 = \phi V \rightarrow \text{volume} \rightarrow \text{saturation}$$

$$M_1 = \int dS \rightarrow \text{interfacial area}$$

$$M_2 = \frac{1}{2} \int \left(\frac{1}{r_1} + \frac{1}{r_2} \right) dS = \frac{1}{2} \int \kappa dS$$

\rightarrow average curvature of the surface $\rightarrow P_C$

$$M_3 = \int \frac{1}{r_1 r_2} dS = 4\pi\chi$$

\rightarrow total curvature \rightarrow related to connectedness of the structure

$\chi = \text{Objects} - \text{Loops} (+ \text{Inclusions})$

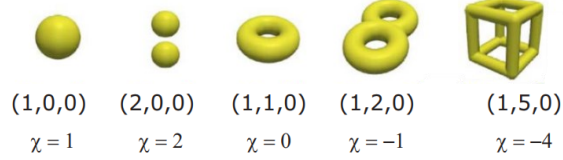
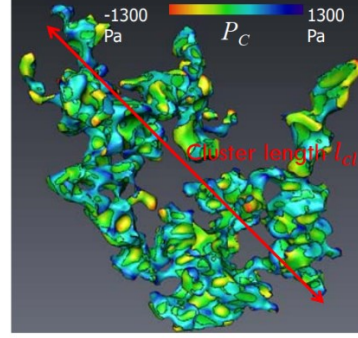


Figure 7: Topological description and Euler Characteristic. The first three are related to porosity since they quantify the intuitive features of the pore space, whilst the fourth one, dimensionless not like others, is related to the connectedness of the pore space. The values in parenthesis are the Betti numbers respectively for the solid objects (57) (15)

2.5.2. Fractal Dimension

Fractals and the fractal dimension are subsets of fractal geometry that according to Benoit Mandelbrot is a way of describing natural phenomena that although are not uniform, obey simple power laws of form $variable_1 \propto variable_2^D$ with D being the non-integer dimension. (58). To explain the concept of fractal dimension we must first explain what a dimension is. The dimension of a space in which an object is defined is the minimum number of coordinates specifying a point on the object (59). In layman's term, it is the number of linearly independent directions of the object. Hence, a line has only one dimension, while plain and cube have two and three respectively. It is significant to understand the difference between a dimension and dimensional in rigorous mathematical language, a case in point could be the description of a circle on a plane which indeed is a one-dimensional object which exists in two dimensions. (60)

A fractal dimension is a dimensionless number (like Euler characteristic) describing the level of self-similarity or complexity of an object or a shape. For a self-similar object, it uses the following equation.

$$\text{fractal Dimension} = \frac{\log(\text{number of selfsimilar objects})}{\log(\text{magnification factor})}$$

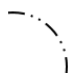
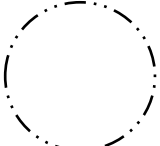
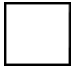
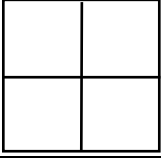

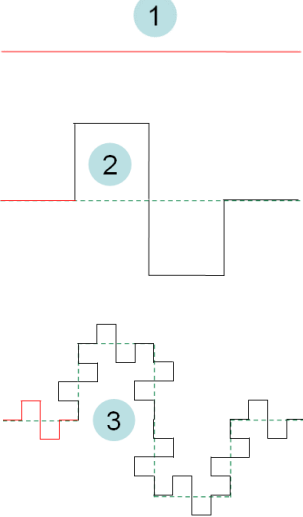
Equation 2: Definition of fractal dimension for a self-similar object

Similar to the Euler characteristic, the application of fractal dimension (D_f)(Equation 2) requires the concept and its equation to be extended and generalized so that it is usable for engineers. An example of its use could be the quantification of ramified patterns of diffusion-limited aggregation processes (DLA) including dielectric breakdown, diffusion-limited polymerization, dissolution phenomenon and viscous fingering (8).

For a representative arbitrary volume in reservoirs, the theoretical values of D_f is between 2 and 3 considering the fact that fractal dimension for a 2D and a 3D object is 2 and 3 respectively (49). However, for the 2D micromodel, this value should be between 1 and 2 owing to the fact that the fractal value is being calculated using 2D images. Apart from the main factors affecting the D_f , its value is

also a function of image quality and image dimension (scale dependency). Hence, it is prudent to come up with an accurate and meticulous approach to calculate the fractal dimension for different experiments to make the results comparable.

Table 4: Examples of Fractal dimension for self-similar objects (59) (61).

Base unit	Name	Iteration Process and the final shape	Order of magnification	Fractal dimension (D_f)
	Circle		4	$\frac{\log N}{\log 4} = 1$
	Square		2	$\frac{\log N^2}{\log N} = 2$
	Minkowski sausage		n	<p>For the first and second iteration:</p> $\frac{\log 8^n}{\log 4^n} = 1.5$ <p>Eventually:</p> $\frac{\log 8}{\log 5} = 1.3652$

As for its application in the petroleum industry, it was first used to determine of the true pore surface area, as a solution to the practical difficulties in its quantification (62). Around the same time, the concept also arose from the usage of percolation theory to describe displacement process in porous medium for $N_c \ll 1$ (34) (63) and later the theory was supported by experimental data (9) where fractal dimension was used to characterize the shape of fingering in immiscible flooding (64) (65). Initial experiments were conducted applying the constant pressure gradient; however, this approach later was reformed, and a constant rate was applied (34). In general, the removal of the initial fluid in place increases its fractal dimensionality. The increase comes from the fluid distribution becoming more complex, especially through the increase in the roughness of the interface. (51) (49).

To understand the reliability of using fractals as a tool to describe displacement process take a look at [Figure 8](#) where the concentration profile (physical approach, using the concept of Peclet number and mathematical description of advection/diffusion process) has been plotted beside the acceptance profile (mathematical approach using the percolation theory).

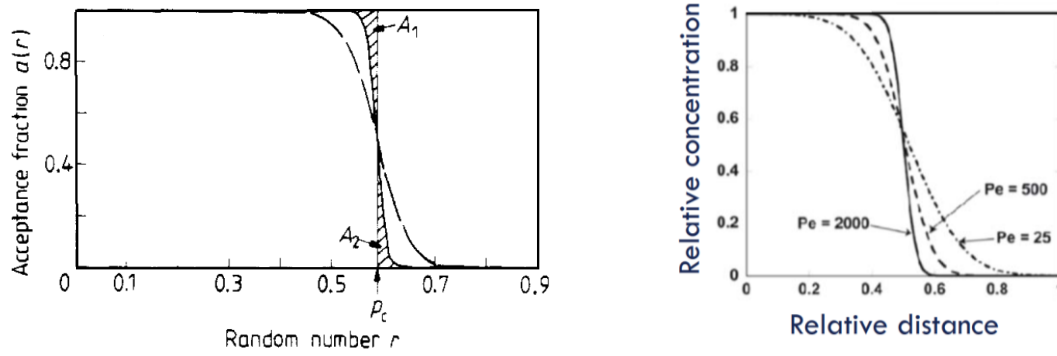


Figure 8: Advection/Diffusion phenomenon has been represented using **left)** Percolation theory and on **right)** concept of Peclet number (34) (57)

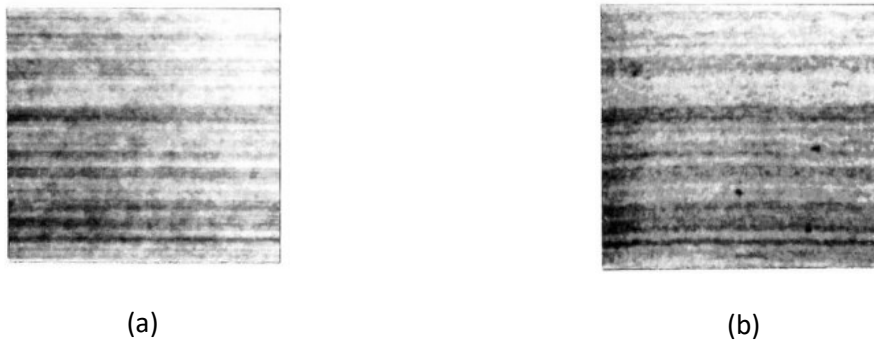


Figure 9: Comparison of a stabbed sandstone core photo **(b)** with a photo-generated using a 2D fractional model **(a)**. Note the striking similarity (7).

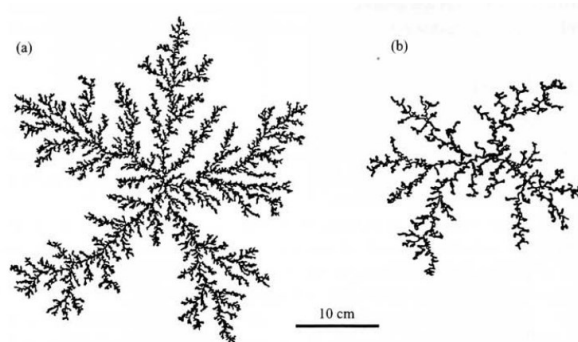


Figure 10: **a)** A pattern produced by computer using Diffusion Limited Aggregation (DLA) and **(b)** injection pattern of air into liquid epoxy in a micromodel test (7).

Concerning reservoir engineering, fractals provide an alternative mathematical model toward the distribution of the rock and hydrocarbon properties based upon scaling law (that means certain geometrical features appear at any scale (66)). Historically this was done by models hinged on effective rock properties for fluid flow calculation (7) (67). Fractal theory, in particular, has been used in different facets of reservoir engineering including logging, core analysis, pressure test data and seismic data where it offers reliable helps in the estimation of the water saturation from resistivity log or scaling up the properties measured in cores to reservoir scale (7). Furthermore, three main properties of fluid flow modelling in porous media can be analysed by fractals. These properties include length scale,

heterogeneity and front instability (66). Correlations have been established between capillary and fractal dimensions which in turn led to correlations between permeability and fractal dimension as well.

In a nutshell, this subchapter with respect to the aids fractals can provide petroleum engineers can be read in [Table 5](#) and seen in [Figure 8-Figure 10](#).

Table 5: Representation of how fractals can be used to interpret and upscale the physical mechanisms observed at different scales (66) (11).

Fractal/Statistical tools	Physical mechanisms and concepts to be interpreted and upscaled
Fractal geometry	Pore Roughness
Effective medium theory	Permeability
Percolation theory	Capillary Invasion, Saturation of non-wetting phase at BT
Diffusion limited aggregation	Viscous fingering and rock dissolution
Multifractals	Represent large variations in filed properties

Pingping et al. showed that the larger the fractal dimension the smaller the oil recovery at water breakthrough. They also found a linear relationship (with a correlation coefficient of 0.67) between oil recovery factor and the fractal dimension (68). A similar result is expected for the end states of water flood and polymer flood for the similarity of the governing phenomenon. Since the larger fractal dimension indicates the stronger heterogeneity of the porous structure.

As regards the particular use of fractals in this thesis, the author focused on the characterization of front stability by fractals as well as their usage in percolation theory. The percolation theory offers many opportunities including estimation of capillary pressure and relative permeability curves (10) which in turn could be used to investigate further concepts in reservoir engineering. A promising filed could be for example investigation of polymer retention.

Eventually plotting the evolution of D_f during the flooding experiments may assist us to visualize the entrapment, breaking part, collision, and mobilization of ganglia of droplets of various sizes by a new approach. Many of the mentioned phenomena are described by the process, called ganglion dynamics (69). Hence, using fractals could provide further insight into ganglion dynamics and help us better understand micro flow regimes and the balance among acting forces in the porous medium. We will take this matter further in [5.3. Geometrical Analysis and Fractal Dimensionality](#) where we answer the fundamental question of which fractal number should be used.

2.5.3. Statistical Analysis in Microfluidics

Statistical analysis provides tools to investigate EOR potential and to configure reservoir models. While the use of percolation theory is already explained for the latter task, here we focus on the application of representative elementary volume (REV) analysis, Lorenz Plot, and cluster size distribution all of which are used for investigation of EOR potential and characterization of the efficiency of different flooding scenarios.

Lorenz Plot

Originally derived from the Lorenz curve, the plot is an indication in the form of graphical representation of inequality of a specific property developed by American economist Max Lorenz in 1905 (70). The property was originally capital and wealth in the economy but in reservoir engineering, we work with the distribution of the volume of remained oil or characterizing the heterogeneity of the porous medium with respect to permeability. Nowadays Lorenz plot is becoming an interesting tool to assess the EOR processes (13).

Eventually it should be mentioned that to plot the Lorenz curve for this thesis, a prepared MATLAB code (71) was used.

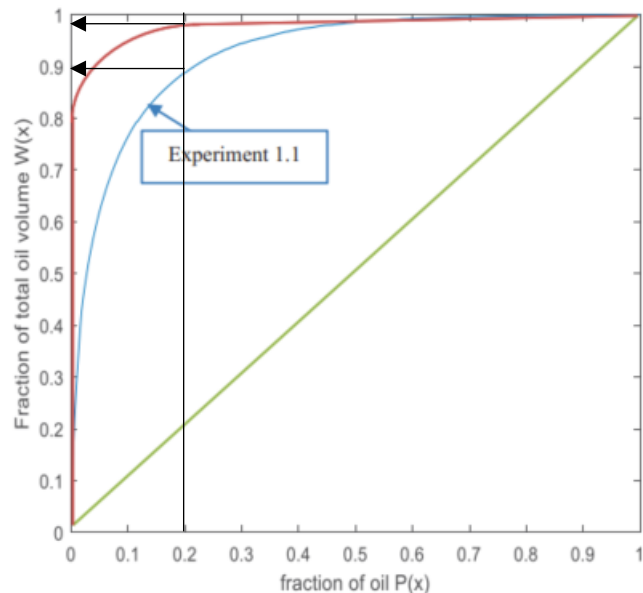


Figure 11: Example of the Lorenz plot (39). The 45° line is the equality or homogeneity line (Depending on the property of interest). The further a curve deviates from the equality line; the more is the level of inequality. In this case, for instance, 20% of the population has 89% and 98% of the total wealth in the blue and red experiments, respectively (39).

Cluster Size Distribution

To investigate the EOR potential, we are interested to analyse two fundamental properties. Namely, phase mobility and recovery. The first one could be studied using cluster size distribution whereas the latter one is explored using cluster volume distribution. The idea behind the application of cluster analysis is to find out the deviation from fractal behaviour to characterize the aforementioned properties of interest. Since idealistically, the normalized cluster volume distribution in a porous medium follows a power-law (fractal) behaviour in accordance with the percolation theory (34) (15) (72). A case could be seen by a)Top [Figure 12](#), where the characteristic of a true fractal system(no scale) is depicted by the $N(s)$ line. It indicates that the same amount of oil is sitting in large clusters as well as the small clusters. However, the data deviates from the line toward right(bigger clusters) suggesting that much of the oil is sitting into larger clusters which in turn proposes that this scenario could be a good choice for further EOR study since unlike the small clusters which are very difficult to mobilize, the large clusters demand smaller force for mobilization. Hence, this scenario has a potential due to the oil sitting in larger clusters. However, the major clusters could be broken apart due to viscous forces acting along the length of the large clusters (73). This process is observed by the author and is characterized by Euler characteristic. Please look at the **Results and Discussion**.

Although using $N(s)$ (number frequency of cluster size s) provides useful information, it could be misleading too, in the sense that in a power-law fit, much higher weight is associated with the larger $N(s)$ for the smaller s . Then $M(s)$ (cumulative distribution) is calculated and used because it varies by less than one order of magnitude normally (13) (73).

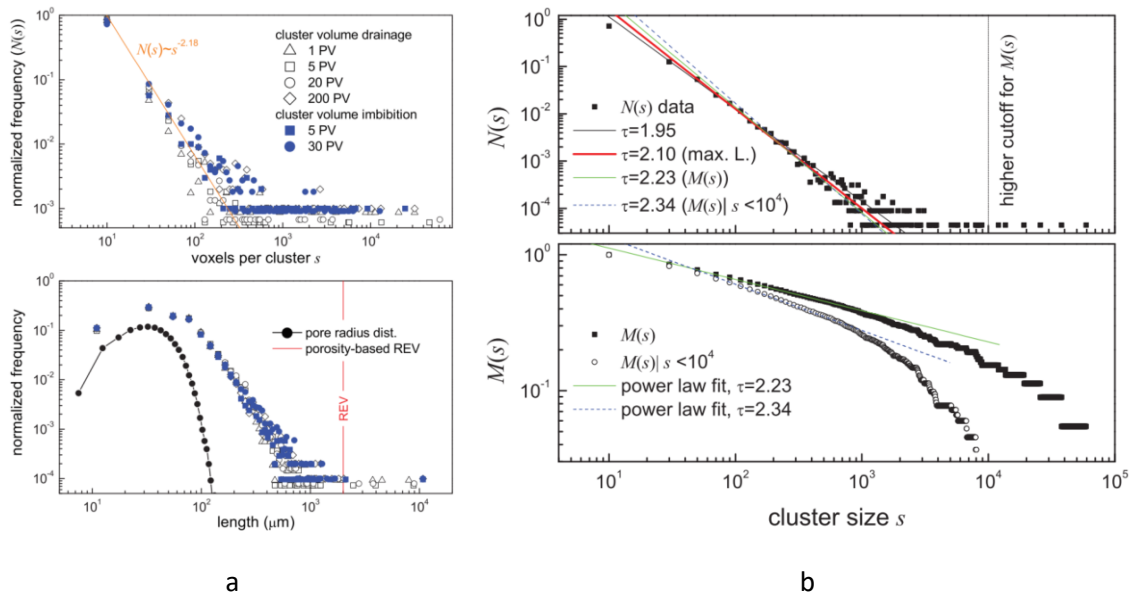


Figure 12: **a)** Top: normalized volume distribution. Bottom: Pore -radius distribution compared to the cluster length distribution **b)** Top: Normalized cluster volume. Bottom: Cumulative distribution for different regions of interest (73).

REV Analysis

REV analysis is the answer to this question that how representative the microfluidics results (this particular field of view of porous medium) is for the representation of two-phase system. The concept has been used for a relatively long time in reservoir modelling for upscaling and averaging processes for macroscopic scale. It is always associated with a property of interest that could be porosity, permeability and/or saturation. As Bear explained, it refers to the scale at which fluctuations in properties approach a constant value (1972). It is prudent to keep in mind that within the same medium different REV may apply to various flow processes. For example, while a uniform micromodel with specific dimensions may not be a REV for water flooding, it may be for Alkaline flooding or polymer flooding. In a nutshell, REV provides an insight to understand measurement scales and variability. The concept is fundamental to the analysis of flow in permeable media without which we cannot upscale the measured property and come up with a reasonable forecast in another medium (74). That is why conducting REV analyses in microfluidics (39) or 3D core imaging (through tomography) (73) (75) is becoming more and more common in the academic work in the field of reservoir engineering.

Although the importance of REV analysis is not a trivial task, its importance should not be exaggerated. In microfluidics, the random outcome could also be a direct result of the variation of the boundary conditions (39).

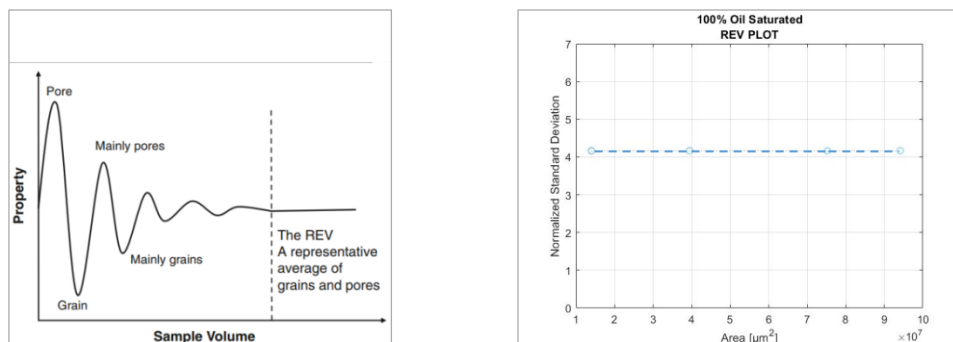


Figure 13: **Left)** The representative elementary volume concept based on work of Bear (76). **Right)** A representative elementary area (REA) plot of a clean uniform network micromodel associated with the porosity and/or saturation.

2.5.4 Estimation of Saturation at Breakthrough using Percolation Theory

Percolation theory offers three different models simulating three main flow patterns in a porous medium. These models include Anti-Diffusion Limited Aggregation (Anti-DLA), DLA and invasion percolation that simulate the stable displacement, viscous fingering, and capillary fingering, respectively. [Equation 3](#) is the outcome of invasion percolation and *scaling theory* both of which come with limitations. The former describes drainage with the assumption that the wetting phase is not trapped and in case it should be used for imbibition, significant errors could be expected; while the latter explains *critical phenomena* which is an attempt to deal with particular phenomena of percolation near a critical concentration above which there is a cluster percolated through the system. In the oil industry, this could be translated as a mathematical effort to estimate the saturation of the non-wetting phase (S_{nw}) at breakthrough. And this is exactly what Blunt recently proposed [2017].

$$S_{nw} \sim \left(\frac{L}{l}\right)^{D-d} \int_{r_c}^{r_{max}} \frac{G(r)}{r} dr \sim \left(\frac{L}{l}\right)^{D-d}$$

Equation 3: Estimation of the non-wetting phase saturation at breakthrough using the probability and statistics of percolation theory (15)

Where $G(r)$ is the normalized distribution of volume on a logarithmic scale of the radius. d is the dimension of the space while D is the fractal dimension. L is porous medium length and should be sufficiently large for the estimation to work (since $D < d$ the ratio tends to zero). The suggestion that micromodel is a 2D environment has the consequence of $S_w = 1 - S_{nw}$; hence, [Equation 3](#) could be validated by microfluidics experiments with regards to the estimation of both wetting and non-wetting saturation at breakthrough.

[Equation 3](#) is obtained from a lattice model, which is a large array of squares, where depending on its structure, the theoretical value of D should be ~ 1.89 and ~ 2.53 for 2D and 3D lattices (15) (58) (63). Moreover, while considering or ignoring trapping has no effect on the results estimated from the model in 3D space, it causes a major difference in 2D space (~ 1.82). Since in 3D space, the structure is more open than 2D space, hence the process of filling the sites (the pores) that causes higher fractal numbers, is not suppressed (15) (58).

In [Further work chapter](#), we will discuss this model and its results more fully.

2.5.5 Instabilities in the Interface

The conducted floodings in this work belong to the category of immiscible displacement. The viscosity ratio is not equal to one and hence for the scenarios of $M\mu > 1$ they are subject to the Saffman-Taylor instability known as viscous fingering (77). We do not consider the Rayleigh-Taylor instability type because of the assumption of 1D horizontal flow in microfluidics and ignorable role of gravity.

Owing to the wetness of the medium, the interface is also susceptible to capillary fingering, which is deterministic (78). Categorizing the flow regimes and to distinguish the disturbances in porous media is a topic of interest and is well covered in the literature (15) (66) (78) (79) (80). Lenormand et al. (78) use the plot of capillary number versus viscosity ratio to differentiate the different flow regimes.

$$N_c = \frac{Q \cdot \mu_{displacing}}{A \cdot \gamma \cdot \cos(\theta)};$$

Equation 4: Capillary number based on the work of Lenormand et al. [1988]. For our experiments, A is the cross-sectional area of the uniform network: $2 \times 10^{-7} [m^2]$.

Where Q is the flow rate, and A is the cross-sectional area to the flow and γ the interfacial tension. This definition of capillary number has the downfall that it assumes, capillary and viscous forces are acting over the same length scale in a porous medium, this is not true. That is why there have been efforts to solve this issue by introducing a geometrical parameter into the capillary number definition (14) (15) (81).

From another perspective, there have been studies on the stability and geometry of viscous perturbations. Notorious work included that of Saffman and Taylor (77), Homsy (80) (82), Koval (83) and Riaz et al. (84) (85). The common mean to solve the perturbation equations is to use the linear stability analysis which in turn results into dispersion curves indicating that in case of dissipation, the maximum reverse wavelength runs down (Figure 14, in the direction of red arrow) making the length scale of fingering very large particularly for the viscous dissipation, hence our micromodel with the length of 1 [cm] might not be a proper representative to observe and investigate viscous fingering.

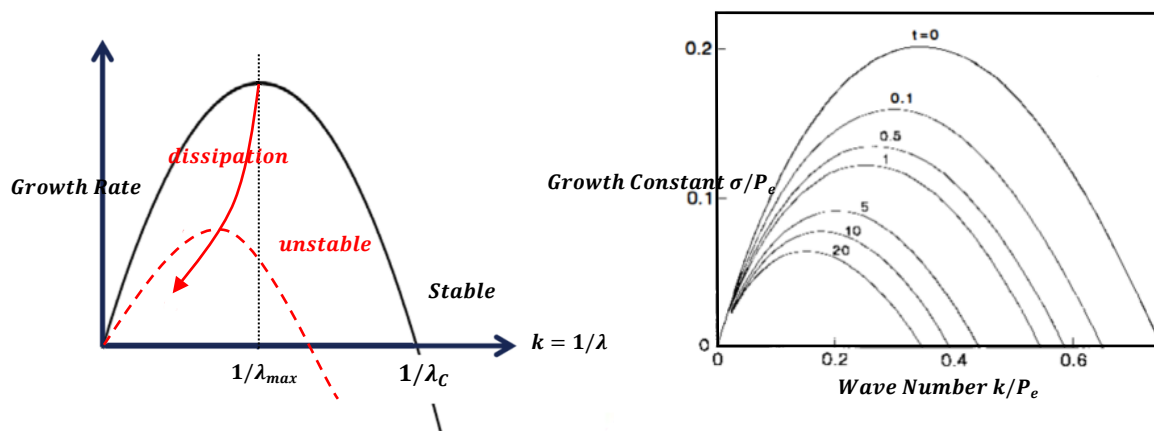


Figure 14: **Left)** Conceptual model of dissipation curve derived from linear stability analysis for viscous fingering. **Right)** Simulation results from the work of Tan and Homsy (82). P_e is the Peclet number, k the wavenumber, t is the time.

By contrast, the viscous fingering zone is ubiquitous for categorizing the flow regime in a microporous domain in the abovementioned literature. Two examples are given in Figure 15.

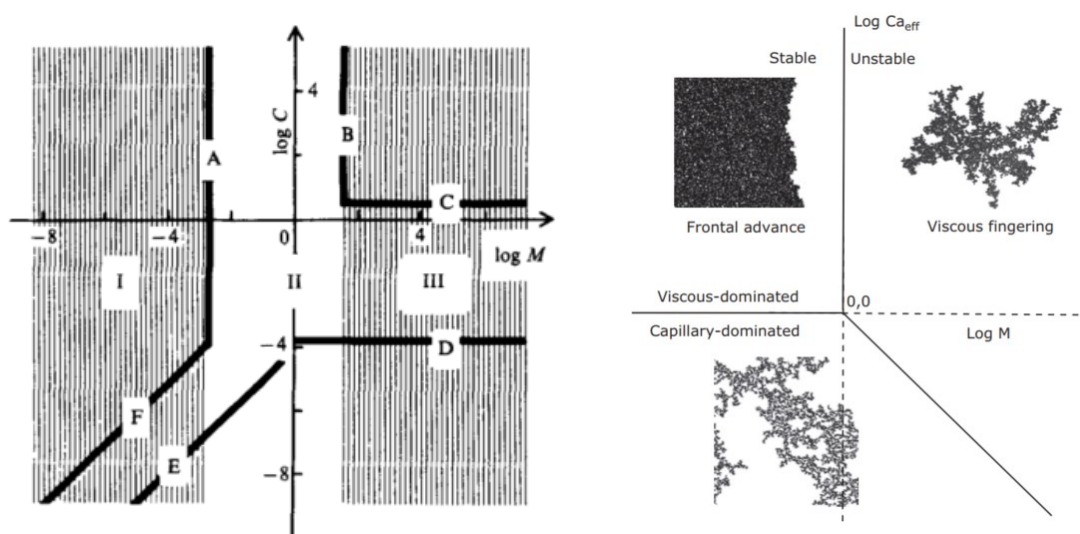


Figure 15: **Left)** Schematic representation of three zones with the boundaries of the domains based on the work of the Lenormand group (78). Stable displacement is limited to BC, viscous fingering zone to AF, and Capillary zone to ED. **Right)** A full regime diagram based on the work of Blunt (15)

As to the work of Lenormand et al. (78), they calculated the value for the borders of different zones using relative permeability and pressure drop. We did not measure nor calculate these values for our experiments, and because we use the Lenormand technique in this thesis, our judgment is based on visual observations. To do so, we have the following criteria (78) (64) (15):

For the viscous fingering:

- There is no loop
- Fingers in viscous cases are very thin.
- No fingers against the direction of the flow will be developed.
- Most importantly viscous fingering is independent of pore structure¹

For the capillary fingering

- Loops are possible and frequent
- Capillary fingering is deterministic.
- The roughness of the interface is noticeable.
- The capillary ramification can occur in all directions.
- Capillary dominated scenarios have a higher RF in comparison to viscous scenarios.

Examples of different regimes are provided in [Figure 16](#) for visual observation.

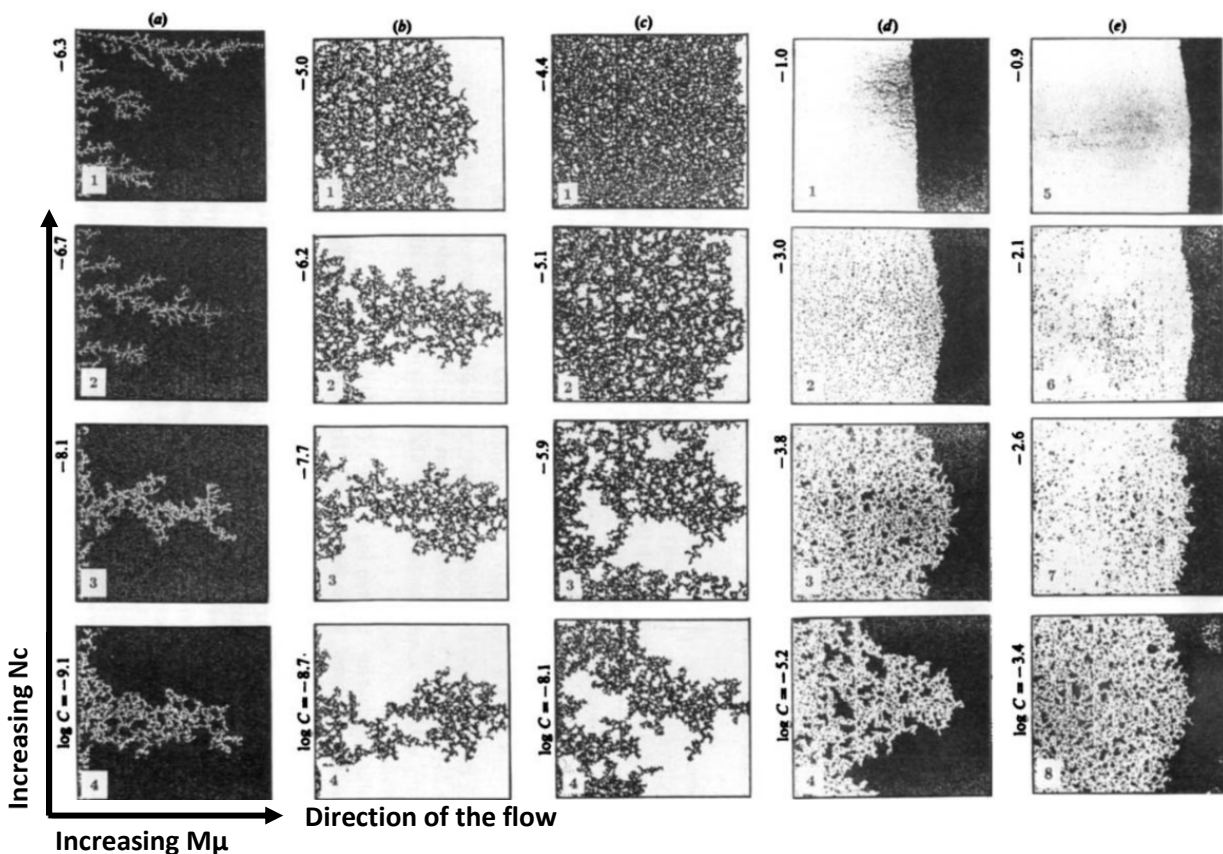


Figure 16: Viscous (1) to capillary (4) fingering according to the work of Lenormand et al. [1988]. (a) Air is displacing a very viscous oil. (b) Mercury is displacing hexane at $\log M\mu=0.7$. (c) Mercury displacing oil at $\log M\mu=0.7$. (d) Glucose solution is displacing oil at $\log M\mu=2$ and various Capillary number: from stable displacement analysed as capillary fingering.

¹ The viscous patterns, however, are still dependent on the pore structure (111).

Chapter 3

3. Experimental Apparatus

In this chapter, we introduce and shortly discuss the equipment that was used by the author. The thesis was carried out in the flooding and imaging laboratory of DPE laboratory building using Xanthan powder from Jungbunzlauer company as the polymer agent, DMi8 microscope from Lecia company and Motic AE200 inverted microscope as visualization apparatus, uniform network micromodels from Micronit company, NE300 syringe pump from New Era Pump System and Fusion 200 Touch syringe pump from Chemyx.

As for software, those required to conduct microfluidics experiments and process the respective images were employed. Apart from the software coming with the used hardware, the main programs include MATLAB, ImageJ and OriginLab.

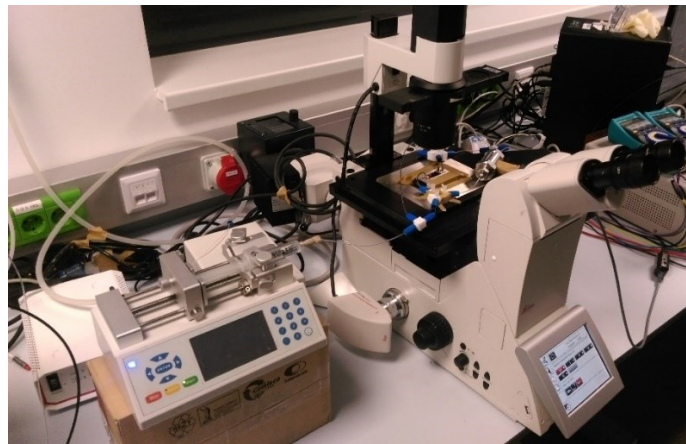


Figure 17: Experimental setup

3.1 EOR Platform

The representative porous medium and its accessories were obtained from the Micronit company. This equipment includes a fluidic connect frame (chip holder), uniform EOR chip and connection kits.

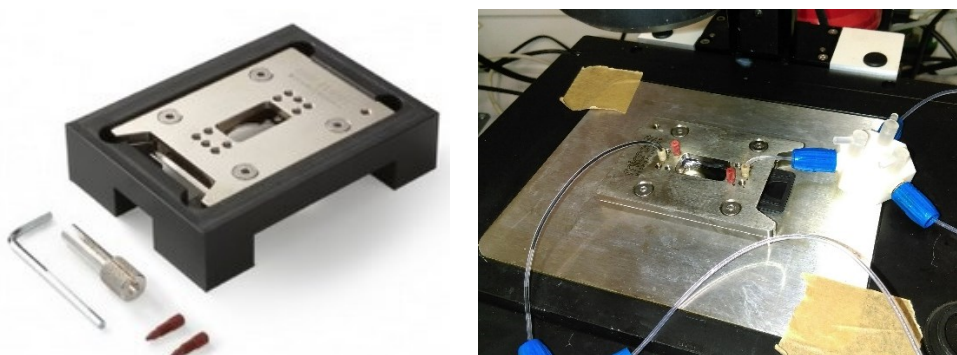


Figure 18: **left**) High-pressure chip holder, **right**) chip holder already assembled.

As for the uniform micromodel, the next image and [Table 6](#) provides the reader with its fundamental properties.

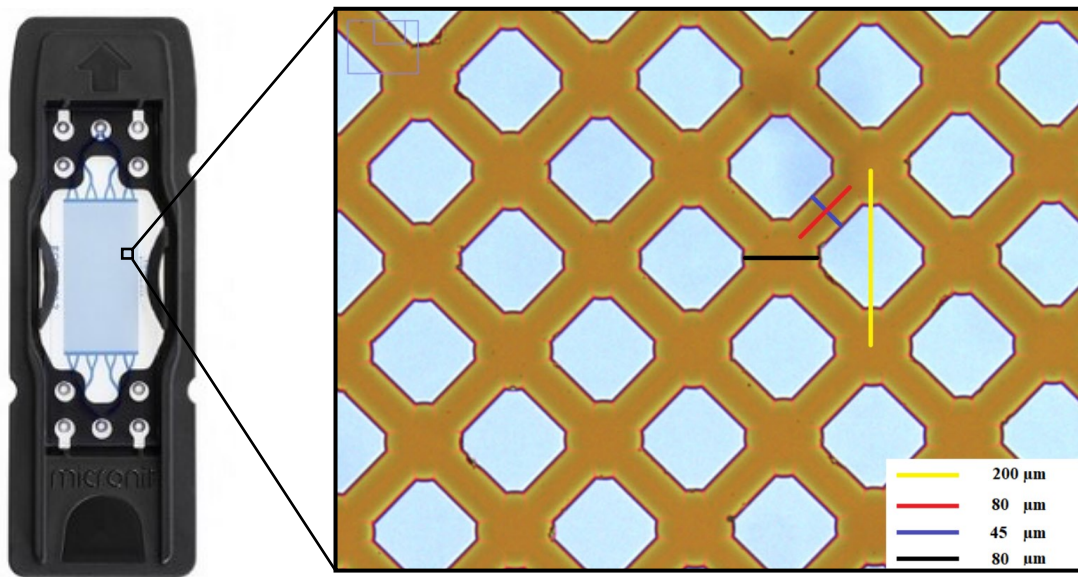


Figure 19: *left*) the uniform micromodel chip inside the black cartridge, and *right*) a zoomed-in area over the porous medium and its geometry.

Table 6: Micromodels specification (86)

Specification	value
size	45mm × 15mm
Channel height	20 μm
Rock pore volume	2.1 μl
Porosity	0.52
Permeability	2.5 Darcy

3.2 Microscope

The images have been taken with a Leica DMI 8 high-end microscope as shown in the following figure. This model is an inverted light microscope with space for five different objectives. In these experiments, objectives with 2.5X, 5X and 10X magnification are applied, depending on the stitching quality of the images. The field of view is based on the magnification and is shown in [Table 7](#). The images are taken with a Leica DMC2900 camera, which is connected to the computer, and an objective with 0.7X c-mount to improve the stitching quality. In addition, it is possible, to acquire an image of the entire flooding domain with an automatic stitching option. In case of 10x magnification, the spatial resolution was 2.2 μm and the time resolution was ~40s.

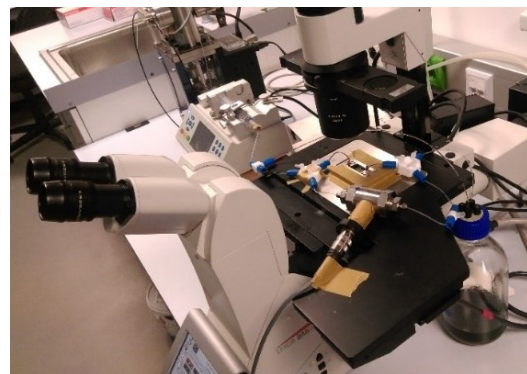


Figure 20: Leica DMI 8 microscope (87)

Table 7: Field of view for microscope objectives.

Magnification	Field of View [μm]
2.5X	3742 \times 2806
5X	1871.09 \times 1403.09
10X	935 \times 701.54

3.3 Injection Equipment

Syringe Pumps

The practical purposes of syringes are for cleaning and fluid injection. The fluid could be oil, water, air or any other type that might be required for the experiment. The only criterion is that the compatibility of the syringe production material and the fluid should be checked before application. A very good example is the injection of Toluene into the micromodel. Toluene will react with the plunger tip (Polyisoprene) of the plastic (Polypropylene) syringe. Hence a glass syringe should be used for this purpose.

For the pumping, initially, NE-300 syringe pump was used. However, it could not provide the necessary accuracy for the low rates injection. That is why standard experiments were conducted using a pulse-free continues syringe injection pump (model Fusion 200 from Chemyx Inc)



Figure 21: **Left)** NE-300 and **Right)** Fusion 200 syringe pumps.

Chapter 4

4. Experimental Methodology

This chapter explains the overall workflow of the conducted experiments. We go through preparation that is required to perform microfluidic experiments until the acquisition of the data.

As for the general methodology, sequences of polymer flooding and water flooding were conducted mainly in two rates of 0.01 and 0.0019 [ml/hr] as well as two phases of secondary and tertiary. To be able to control the effect of pore network geometry, these experiments were performed only in uniform micromodel. Crude oil of the target field from the Vienna Basin, which has a high viscosity and TAN number was used in all the experiments.

Table 8: Sample oil properties (38).

TAN [mg KOH/g oil]	Density @ 20°C [g/cm ³]	Density @ 15°C [g/cm ³]	Viscosity @ 20°C [cP]	API °
1.96	0.9306	0.9339	331	19.88

The injection rate and the polymer concentration were changed systematically, causing a change in viscosity ratio ($M\mu$) of about three orders of magnitude [0.003-1.64] cP. While other parameters including oil, water and polymer type were kept constant. The flow mechanism and displacement patterns on a microscopic scale were observed, photographed and investigated.

4.1 Preconditioning

Preparation of the solution

The solution process of Xanthan in water takes place in two stages. Initially, a gel is formed when water molecules start to associate with polymer chains. The second stage where the solved polymer molecules disperse is affected by mixing technique (88). The methodology of preparation of the solution is as follows:

Initially, the desired amount of the polymer and water were calculated and measured using “Precision balance EG-N”. What we should consider is that one litre of water has a slightly different mass depending on the ambient temperature. That is why the measuring part is important and should be accurate. The polymer concentration in the solution is calculated using the following equation.

$$1 \frac{g_{polymer}}{l_{water}} = \frac{1}{m_w} \frac{g_{polymer}}{g_{water}} = \frac{1000}{1000\ 000} \frac{mg_{polymer}}{mg_{water}} = 1000 [ppm]$$

$$m_w [g] = \rho_w^{@ Lab Temp} [g/ml] \times 1000 [ml]$$

Equation 5. Polymer concentration and related mass of water calculation



Figure 22. **Left)** Precision Balance and **right)** Magnetic stirring instrument with a beaker, containing the prepared solution.

Xanthan shows high resistance to mechanical degradation, however, to avoid it as much as possible, we add water first to the beaker and then place the beaker over the stirring device, with the stir bar inside it. Once the stirring process started and water formed the vortex, Xanthan powder was added to the edge of the vortex slowly. The stirring should continue until the aquatic medium is entirely transparent with no lumps visible. This will take around 6 hours. As a general rule of thumb, the author ran the stirring for 12 hours. The top of the beaker was covered by a plastic cap so that water vapour cannot leave the container.

Should the polymer solution storage time exceed 24 hours, adequate preservation is necessary to prevent microbial degradation (89). That is why the beaker should be cleaned before and after usage and new syringes were used every time.

For our experiments, the injection phase took 36 hours the most, during which the polymer solution did not show any visual sign of degradation owing to light exposure.

Cleaning Process

Xanthan is not directly soluble in solvents like Acetone and Toluene. Therefore, the normal cleaning procedure that was followed by Borji (38) is not enough to dispose of the adsorbed polymers after polymer flooding. [Figure 23](#) compares two cases of water flooding at the same rate where the polymer remained in the micromodel having been cleaned by the normal procedure caused the dramatic increase of the recovery factor.

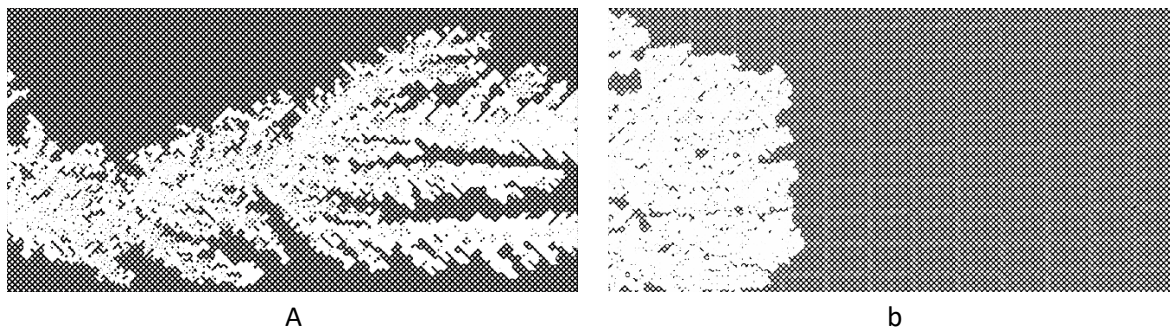


Figure 23: Examples of two waterfloods after ~ 0.24 injected pore volume in **a)** clean micromodel, **b)** porous network contained adsorbed polymer before the flooding.

The cleaning procedure is a modification of what was followed by Borji (38) and Kharrat (39) and it was proved to be efficient by giving reproducible recoveries for waterflooding. For the aforementioned case the recovery reduced from 90% to 50%. The procedure goes as following:

- a) Inject 50 pore volume of acetone.

- b) Inject 50 pore volume of toluene until no trace of oil is visible in the connection pipes and chip.
- c) Inject 50 pore volume of acetone to clean toluene.
- d) Use the ultrasonic vibrator. Inject distilled water with the rate [0.001] ml/hr while the chip is placed inside the ultrasonic. Set the temperature on 50 degrees and let the injection continues for four to five hours.
- e) Take the chip outside the ultrasonic and inject acetone to displace water.
- f) Use the vacuum to remove the acetone and air. (normally no more than 1.5 hours)

Note that it might be necessary to change the injection direction from that of the flooding direction, owing to the debris that might have got stuck inside the chip. The clean chip should be free from any debris.

Saturation the Chip with Oil

Pump the oil inside the chip under vacuum until the medium is 100% oil saturated. After this step, the chip is ready for flooding scenarios. Depending on the specific case, we injected distilled water or polymer solution.

4.2 Conducting Experiments

In total, fourteen experiments were conducted eight of which were standardized. It means their methodology and their conducting procedure, as well as used equipment and materials, were the same. There were other tests which were used mainly to provide supporting data. The standard experiments were performed in two rates and two phases of secondary and tertiary. The secondary ones were conducted with four different polymer concentrations. Starting from zero (waterflooding) and ended with 2000 [ppm]. A general description of these experiments is provided in [Table 9](#). Please notice the terminology there because henceforth, the author only refers to the experiments using this terminology.

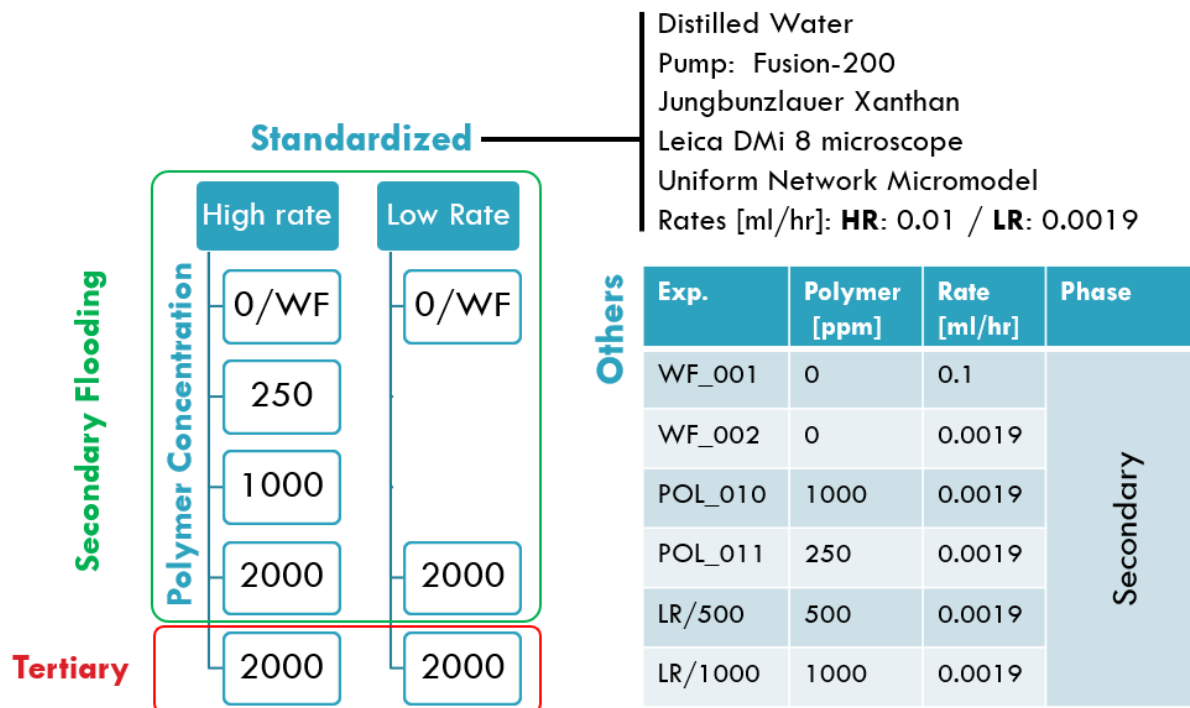


Figure 24: General Overview of the conducted experiments. The results are derived from standardized tests. However, some other experiments were used mainly as complementary data providers.

Table 9: General description of the experiments.

Experiments *(Main Terminology)	Original Name	EOR Phase	Rate [ml/hr]	[ppm] polymer	Used water	Details
0.1/WF	WF_001	Secondary	0.1	0	Tap water	NE-300 pump Moic AE200
HR/0	WF_003	Secondary	0.01	0	Distilled	Standard
HR/250	POL_006	Secondary	0.01	250	Distilled	Standard
HR/1000	POL_007	Secondary	0.01	1000	Distilled	Standard
HR/2000	POL_008	Secondary	0.01	2000	Distilled	Standard
HR/T	POL_T_001	Tertiary	0.01	2000	Distilled	Standard
LR/0	WF_004	Secondary	0.0019	0	Distilled	Standard
LR/500	POL_004	Secondary	0.0019	500	Distilled	NE-300 pump
LR/1000	POL_003	Secondary	0.0019	1000	Tap water	NE-300 pump
LR/2000	POL_009	Secondary	0.0019	2000	Distilled	Standard
LR/T	POL_T_002	Tertiary	0.0019	2000	Distilled	Standard
Data could be used for further work	WF_002	Secondary	0.0019	0	Distilled	Could be further used for evaluation of polymer retention
	POL_010	Secondary	0.0019	1000	Distilled	
	POL_011	Secondary	0.0019	250	Distilled	

*LR and HR are abbreviations of the low rate and high rate while the number after the slash sign is the polymer concentration. T states for tertiary flooding.

Duration of the Experiments

In all standard experiments, the flooding continues until no further changes could be detected with time. This was achieved after injection of at least 23 times pore volume.

4.3 Data Acquisition

Flooding records (duration, injection rate and polymer concentration) and images of the micromodel are the main experimental data. Any other data is extracted primarily from these two. The extraction process was mainly done by image processing and image analysis. The difference is that in image processing, using some transformations, we create a modified version of the original image, while in image analysis, a different image or information will be extracted from the original image.

4.3.1 Image Processing

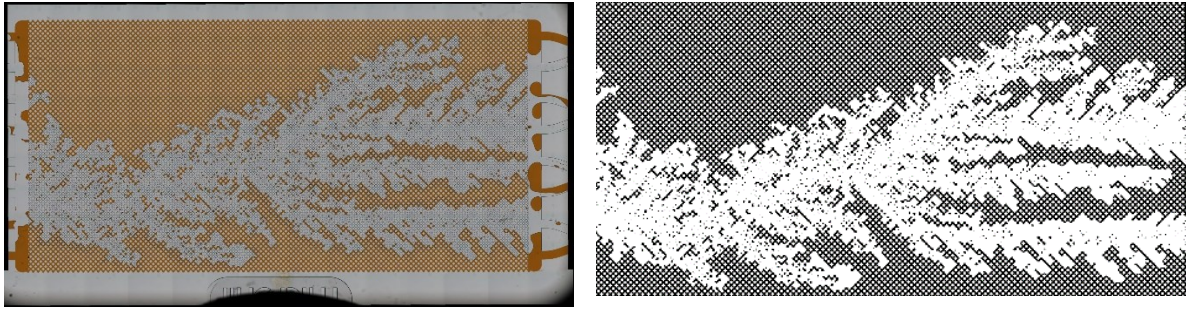


Figure 25: *left) original RGB image and right) the processed image.*

Original RGB images will go through transformations so that artefacts and grains could be removed. All images should meet the same quality and have the same format. For this thesis, this was Tiff format with the dimensions of the images to be around 21000×10000 pixels.

Quality Control the Original RGB Image

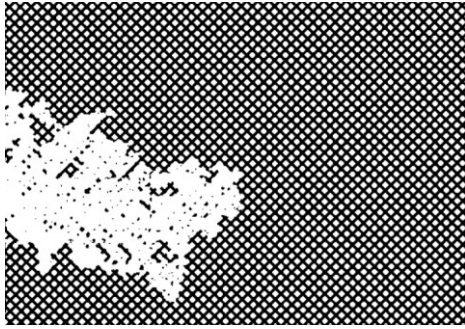
At this step, ‘image stitching’ followed by ‘background removal’ is executed.

Typically, the large high-quality images of the micromodels do not fit in the field view of the microscope, hence an image stitching process is necessary. This process can be implemented using a plugin in ImageJ or by the microscope software. In both cases, there is always an error causing artefacts in the final results. Thus, an error analysis is necessary to assure the accuracy of the results. In the series of the experiment done by the author. Using various techniques including setting up the proper configuration for the stitching process, using opening and closing processes and manually stitching or even manually removing artefacts, errors regarding the calculation of RF , χ and D_f were always kept below 0.01% (Figure 27). Then the ‘subtract background’ command (normally with the ball radius of 50) was executed to ensure a uniform light distribution over the field of view. The image is ready for binarization now.

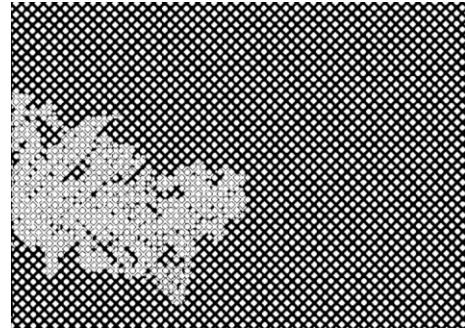
Binarization and Opening Process

Researchers in the DPE at MUL implement morphological opening (erosion followed by dilation (37)) to remove artefacts and to measure the area fraction which in turn is used to measure the recovery factor. The tricky point is that once the image is made binary, the pixel value of 0 (level of intensity) should be assigned to the white colour (water phase), this often happens automatically, if not, then an inversion is needed which in turn makes the usage of morphological closing instead of opening necessary.

After binarization, seven times opening was executed so that the grains are omitted. However, in order to get consistent results, the images should be binarized from a TIFF format and not a JPG nor PNG, since the quality of the images changes during the compression process. Moreover, the associated pixel value to water should be 0 while oil is 255. Sometimes the software associated reverse values to oil and water. In these cases, the values were corrected using the following command in ImageJ: ‘Image>Lookup Tables>Invert LUT’ after which seven times closing (dilation followed by erosion) should be implemented and then the extraction of information could proceed. Worthy to notice is that the potential error caused by image format and wrong values is negligible for D_f and $\%RF$ calculation, whereas it could be very serious regarding χ_N as could be seen in Figure 26:



RF: 6%; D_o :1.872; χ_N =-7427



RF:4%; D_o :1.872; χ_N =-5.7

Figure 26: Opening process implemented on an image (zoomed-in area) **left**) with correct pixel values (oil:225; water:0) **right**): reverse pixel values. Notice the major difference in the values of Euler characteristic.

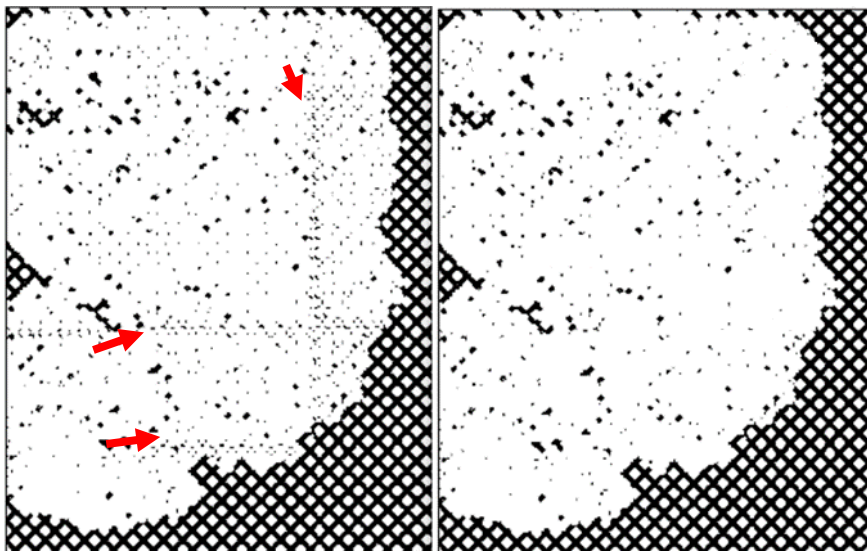
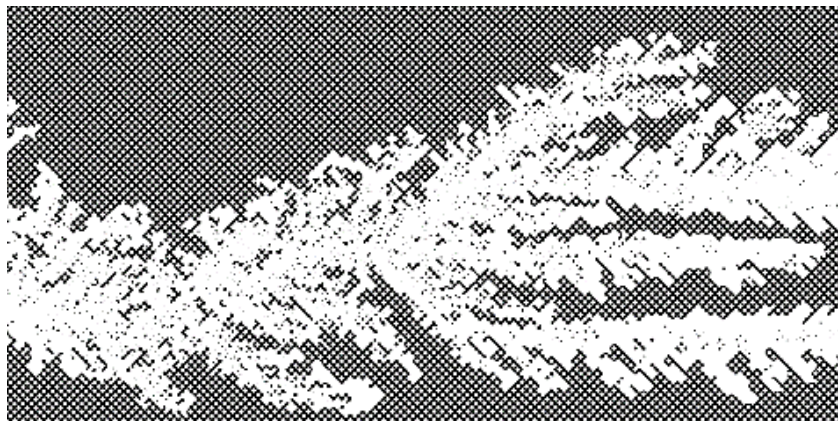


Figure 27: For this specific case(LR/2000, $PV_{inj}=0.1$) the error regarding the Recovery factor, Euler Characteristic and Fractal Dimension are less than 0.005%, 0.007%, and 0.01% respectively.

4.3.2 Image Analysis

Image analysis was proved to be extremely useful in the extraction of information. Because it separates a specific feature inside the image and the corresponding value could be independently calculated. The analysis was always performed on the images that were already binarized and opened. The version of ImageJ that was used is Fiji.



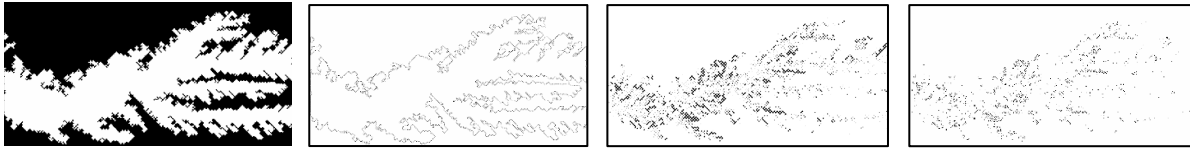


Figure 28: **top)** original image ready for analysis. **bottom row from left to right)** extraction of corresponding features including areal sweep, an outer perimeter, residual oil and the area of the clusters of the residual oil.

Extraction of Areal Sweep

Use the following morphological commands in sequence.

‘Fill holes’, ‘invert’, ‘fill holes’, ‘invert’

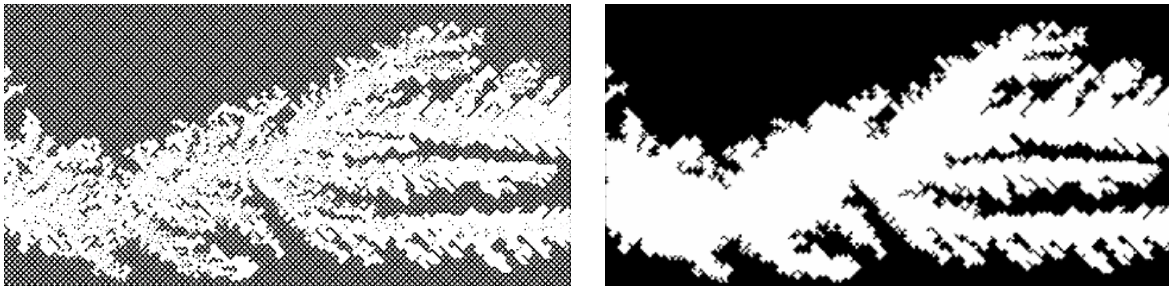


Figure 29: Result of the extraction of the areal sweep. The grains are entirely removed as well as the residual oil.

Once the commands are executed. The area (ratio of the black to white pixels) is obtained by ctrl+M.

$$\text{Areal Sweep}[\%] = 100 - \text{Area}$$

Extraction of Residual Oil Saturation Inside the Swept Zone

Use the morphological command ‘Kill borders’.

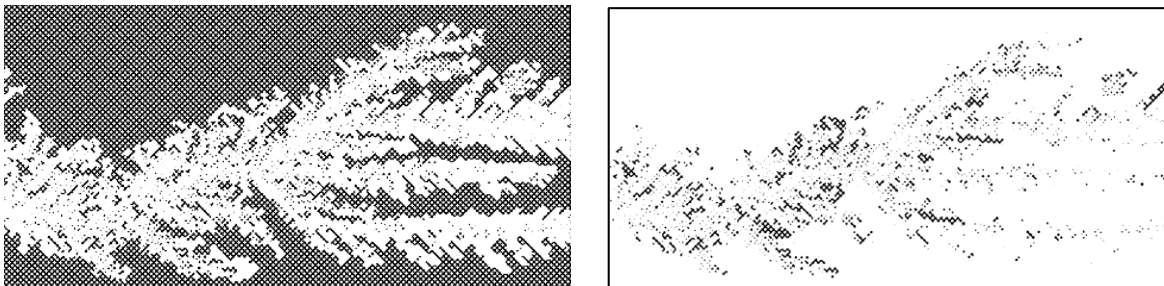


Figure 30: Results of the extraction of residual oil inside the swept zone.

Once the command is executed, use the area to calculate the saturation of the residual oil. The initial area is normally 60%. But it was calculated for every scenario individually.

$$S_{or} = \frac{\text{Area}}{\text{Area}_{initial}}$$

Extraction of the Fluid Interface

Use the morphological command ‘Fill holes’, followed by ‘Area filter’ and ‘invert’.

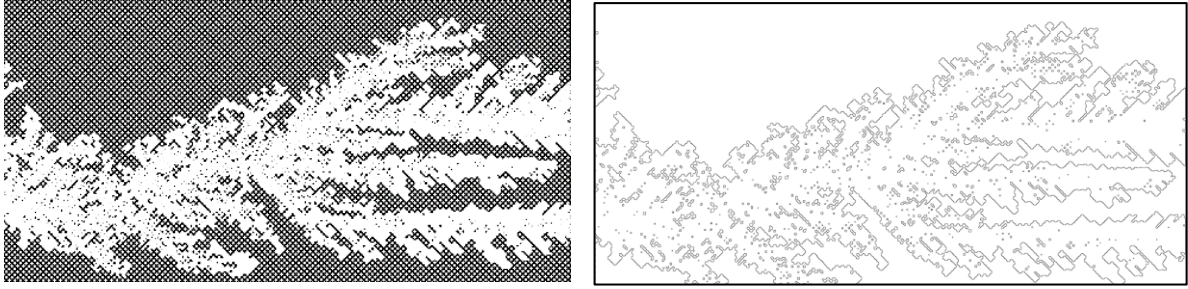


Figure 31: Result of the extraction of the fluid interface including the outer perimeter and the residual perimeter.

Extraction of the Outer Perimeter (the fluid interface on the outer front)

This feature entirely governs the complexity of the front and its corresponding fractal number quantifies it. Hence its extraction was very important.

Use the morphological command ‘Fill holes’, ‘invert’, ‘Fill holes’, ‘Area filter, and ‘invert’

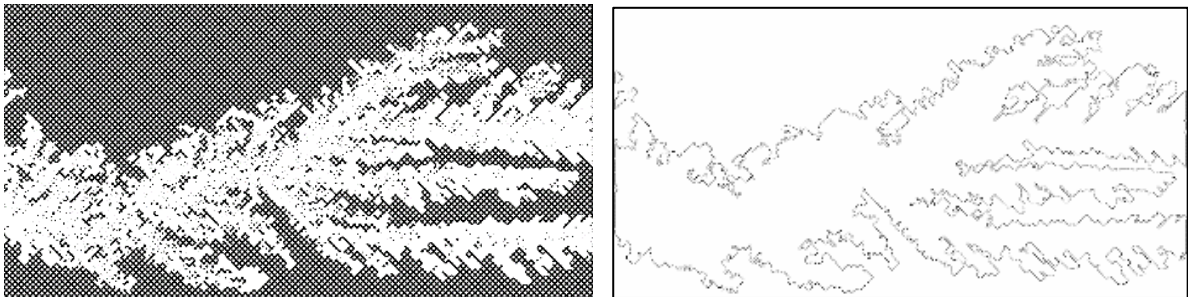


Figure 32: The extraction of the outer perimeter.

Eventually, the use of Macros in ImageJ could help in automation these processes. This saves a considerable time especially once there are many images to process and analyse.

4.4 Calculations

4.4.1 Injected Pore volume (PV_{inj})

$$PV_{inj} = \frac{t \times Q}{3.6 \times V_{pore}}$$

Equation 6: Calculation of injected pore volume. The time starts once the fluid reaches the porous domain. Time (t) is in second, injection rate (Q) is in ml/hr and pore volume is 2.1 μ l.

4.4.2 Recovery Factor (RF)

$$RF_{secondary} = 1 - \frac{Area}{Area_{pore}}; \quad RF_{Tertiary} = 1 - \frac{Area}{Area_{oil, end\ state\ of\ secondary\ flooding}}$$

Equation 7: Calculations of secondary and tertiary flooding recovery factors.

4.4.3 Fractal dimension (D_B)

Oil and water fractal numbers (D_o , D_w)

The used fractal number is based on the box-counting method (scaling rule) by ImageJ (42). It is the slope of the regression line for the log-log of scale and count. Before the calculation, there are some options to config. Most important of them all are the scaling method and setting the background colour.

Once the **background** colour is defined, number of the counts only corresponds to the boxes within which we have the **foreground** colour. For example, if we set the background colour to black, only the boxes with white colour (water phase; D_w) inside will be counted and vice versa. That is why calculating the fractal number for two phases gives different results. **This is caused by the point that; the trapped clusters only influence the fractal number of trapped phase** (non-invading phase) owing to the scaling rule. The presence of the residual black clusters has a minor effect over the number of white counts. The influence only will be felt once the grid size (calibre) is smaller than the length of the residual cluster. An example of calculated D_w and D_o with and without residual clusters could be seen in [Figure 34](#).

We have used the fractal number, having been calculated only for the boundary. That is why it is most sensitive to the instabilities of the front.

Another necessary configuration is the type of scaling method. ImageJ offers seven different modes including, *power law*, *default sampling size*, and *block series*. **The scaling method is the way that calibre changes**. The size of the calibre is between a minimum and a maximum pixel (as default 0 to 45% of the image dimension_ that is how the dimension of the domain influences the results). *In power law method*, the box sizes are following a power series like *base^{exponent}*. The base is raised to the exponent added to itself to make successive sizes. As a default, the base and exponent are 2. So, The first three sizes are 4, 16, and 64. Selecting the *bock series method* makes Fracklac calculate a series of box sizes that divide evenly into the largest size and are no smaller than the smallest \pm 5 pixels. **This will cause the removal of the partial boxes in counting**. In the *default sampling method*, the series increases in size linearly by a fixed increment over a range from minimum to maximum. The increment is set by dividing this range by the number of sizes requested. If the minimum is 0 pixel, the maximum is 5000 pixels, and the number of sizes is 100, then the series of the boxes sizes will be 50, 100, 150, ... 5000. Concerning this thesis setting, we used the *default sampling method* with the number of sizes left to 0 (which Fraclac uses 100 instead) and the range [0-45% of image] pixel.

Eventually, it should be mentioned that the values that ImageJ delivers are an average value that already takes into consideration the error that is caused by image orientation examples of calculating the fractal number is shown in [Figure 33](#).

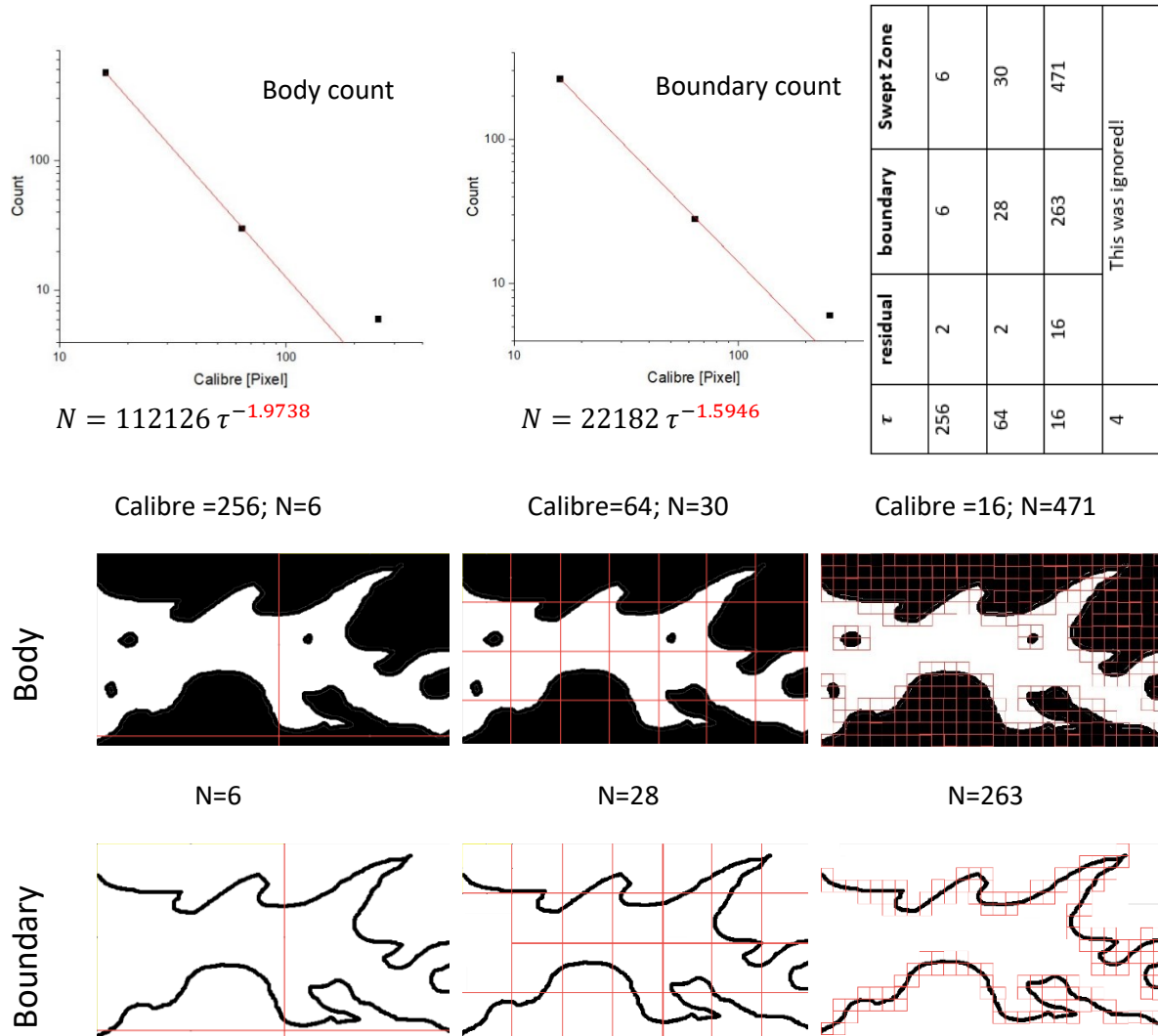


Figure 33: Examples of calculating the fractal number for two cases. τ is the calibre length [pixel] and N is the counts. The background colour is white, then in both cases, N counts the boxes within which there are black pixels (foreground colour). Scaling method is power law. The dimensions of the domain is 538×271 pixel. Hence the maximum box size is 65609 pixel (\sim a square with length of 256 pixel). Notice that the calculated fractal value for the front is much smaller than that of the body. I avoided the 4 calibre grid size and its calculation because it was too cumbersome to show; therefore, the calculations are not accurate but the purpose of this figure is only to demonstrate the method.

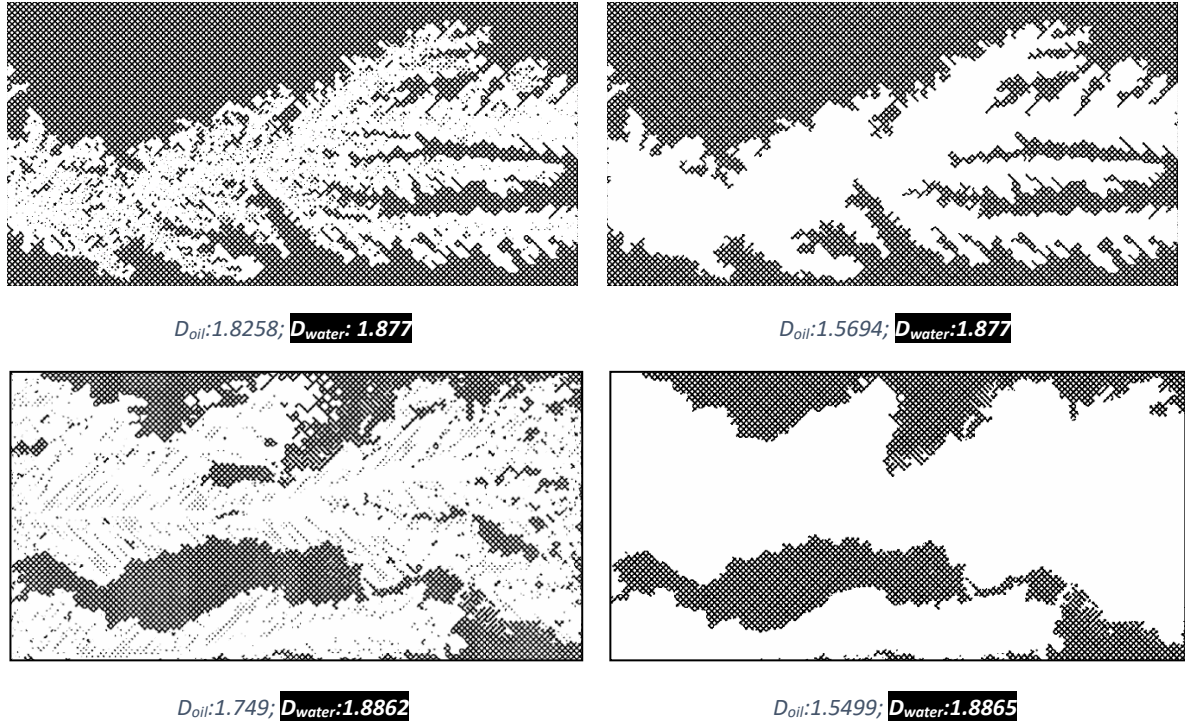


Figure 34: **Left)** the normal binary image. **Right)** holes are filled morphologically. The order of magnitude that water fractal number is affected by the removal of trapped oil clusters is negligible or minuscule.

Normal fractal number (D_N)

Introducing and employing D_N was helpful to remove the sources of errors in D_o calculation. By removing the effects of artefacts and images dimension variability, different scenarios could be compared regarding their oleic fractal numbers, so that the scale of changes is better understood. For example, rather than values of 1.8746 and 1.6654 we will have 32 and 261. Moreover, D_N follows the trend for D_w , which its calculation was not always possible by ImageJ.

$$D_N = \frac{D_{oil}}{Area}$$

Equation 8: Calculation of normal fractal number

Fractal number of the outer perimeter of areal sweep (D_{front}) and the total interface perimeter (D_{int})

These fractal numbers are extracted from the corresponding images. The first one quantifies the propagation of the front while the second one corresponds to the first Minkowski functionality. We have used D_{front} in [5.3 Geometrical Analysis and Fractal Dimensionality](#) and it provided satisfactory results.

4.4.4 Euler characteristic (χ)

We have already explained the concepts regarding Euler characteristic in [2.5.1 Euler Characteristic \(\$\chi\$ \)](#). Here we just introduce how it was calculated by *ImageJ>BoneJ* plugin and moreover, we explain the effect of cluster fragmentation on the value of χ so that the results in the discussion chapter are better understood.

The BoneJ plugin is an adaption of *ImageJ>3D Object Counter plugin* for identifying particles as a part of connectivity analysis (90). BoneJ defines the Euler number using the same [Equation 1](#). However it defines β_1 as number of holes in all of one components (1 dimensional Betti number) ([Figure 36](#)) and β_2 as number of cavities in all of one components (2 dimensional Betti number). By this approach $1 - \beta_1 + \beta_2$ is always equal to 1-loops ([Figure 35](#)).

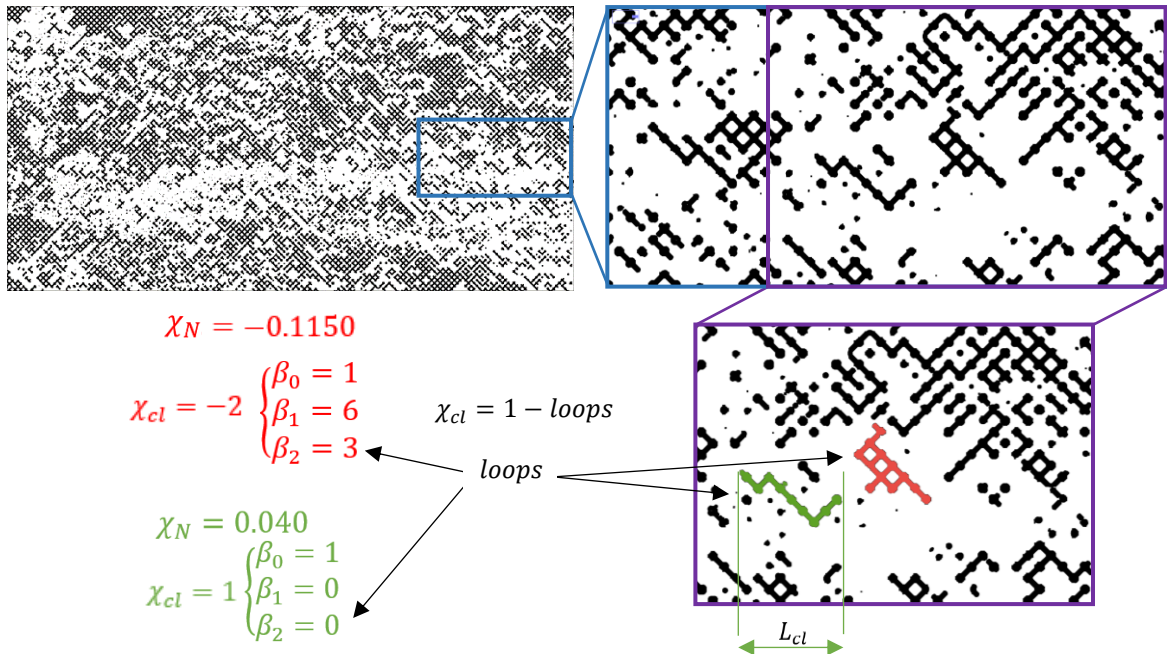


Figure 35: Determination of Euler characteristics based on BoneJ procedure. **Left)** Oil distribution at some point in LR/T. **Right)** magnified frame and the calculated χ and χ_N for the two specified clusters. The negative value indicates higher connectivity while its larger absolute value shows a larger volume. Note that BoneJ plugin takes a different approach to calculate the χ_{cl} , however the final result is correct.

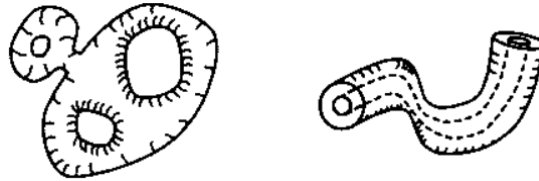


Figure 36: Holes (handles and tunnels) according to (91)

So in our 2D microfluidics the value of β_2 is the number of grains and β_1 is $2 \times$ complete grains – number of incomplete grains at borders of the image. Important to consider is that although ImageJ uses this misinterpretation, the final calculated value for χ is correct. Now with this introduction, we check how we calculated the χ_N .

for cluster i ;

$$V_{ni} = \frac{V_i}{\sum V_i} \quad \text{Normalized area } V_{ni}, \text{ the ratio of cluster volume } i \text{ over the total area of clusters}$$

$$X_{ni} = X_i \times V_{ni} \quad \text{Normalized Euler characteristic for cluster } i$$

for the system;

$$X_N = \sum X_{ni} ; \quad \text{Normalized Euler characteristic for the system}$$

Equation 9: Calculation of normalized Euler characteristic.

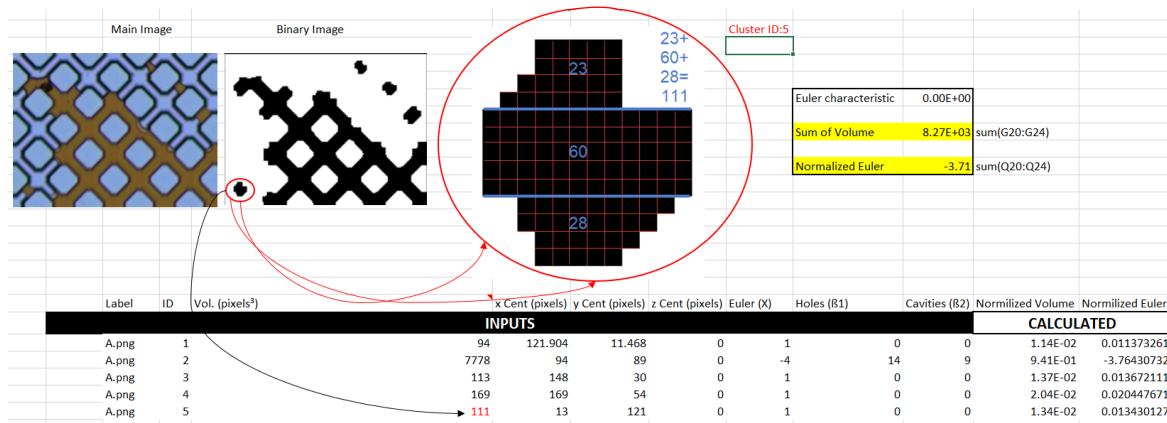
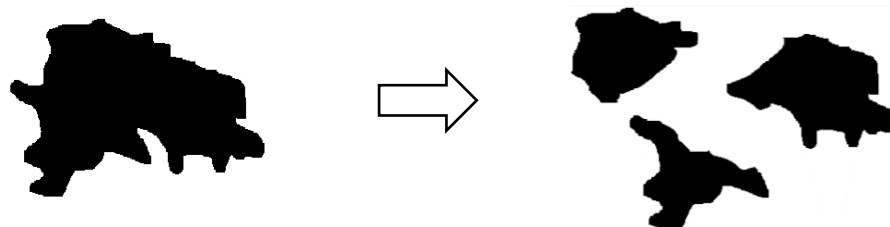


Figure 37: The procedure to calculate χ and χ_N for the binary image. Five calculations correspond to the five connected oil clusters. Voxels are only counters of the pixels. Note that we are in a 2D dimension. β_1 is the connections that is calculated as the sum of necks and handles for a complete grain and just the neck for grains at border. For the second cluster with area of 7778, there is nine grains (β_2), four of which are on the border. Hence, $\beta_1 = (5 \times 2) + 4 = (2 \times 9) - 4 = 14$. For cluster #2, $\chi_{cl} = 1 - 14 + 9 = -4$ and $\chi_N = \frac{-4 \times 7778}{8265} = -3.76$.

As can be seen in Figure 37, there are five connected oil clusters and that is why there are five calculations. The voxels are indeed a counter, counting the number of the pixels that could be associated with the area as well. Cluster with ID#5 is magnified and the numbers of its pixels were calculated manually. It is 111 pixels, which equals the provided number by the software.

Now we investigate the effect of cluster fragmentation on normalized χ_n . If we check Equation 1, it is better understood how they occur.

When an oil cluster breaks apart, what is remained is many smaller isolated clusters with the sum of their volume being equal to the initial cluster volume. This is depicted by the following image:



$$X_i = 1 - \beta_1 + \beta_2; X_n = X_i \times V_n$$

$$\chi_{n_1} = \chi \times V_n \qquad \chi_{n_2} = X_1 \times V_1 + X_2 \times V_2 + X_3 \times V_3$$

Figure 38: An example of one initial cluster (without segmentation) breaking apart. Once it fragments, the sum of V_i equals to V so V_i is always smaller than V . However, $\chi_i = \chi_{n_1}$ hence sum of $\chi_i = \chi_{n_2} = \chi_{n_1}$. For the right side we have $V_i = 0.29V, 0.43V$ and $0.28V$. For these specific clusters, $\chi_i = \chi_{n_1} = \chi_{n_2} = 1$.

Figure 39 shows an oil cluster inside the porous medium. Notice that the initial χ has the maximum negative value. Then its value starts to increase owing to fragmentation and oil production.

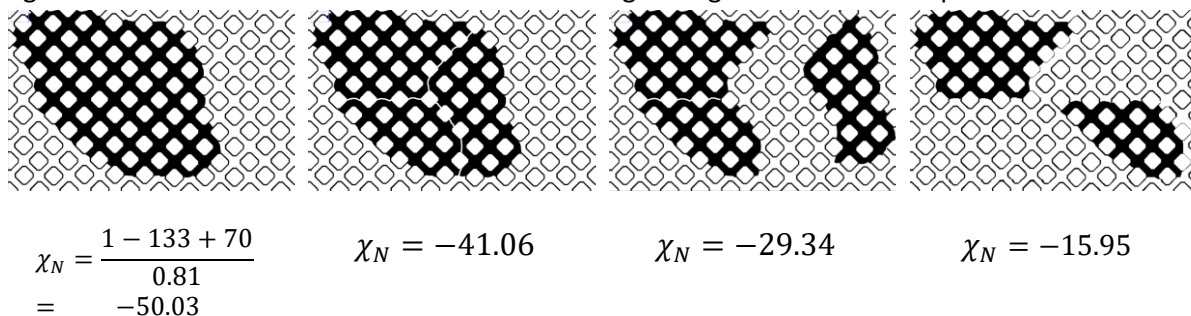


Figure 39: Cluster fragmentation and oleic phase leaving the system. The effect can be seen on Normalized χ .

4.4.5 Statistical calculations

Cluster size distribution

We plot the discrete frequency versus sizes of the clusters using OriginPro. The input data was provided by ImageJ, Fiji version. Once the data is plotted on a logarithmic scale, its deviation from the power law is an indication of deviation from the fractal behaviour. The characteristic of a fractal behaviour is that it has no scale. Hence a deviation tells us that the volume is not distributed equally. We can use either cluster area (using Particle Analyser plug-in) or cluster length (using '3D object counter' plug-in) as the x-axis. Using the cluster area may end up in small inconsistencies owing to rounding error.

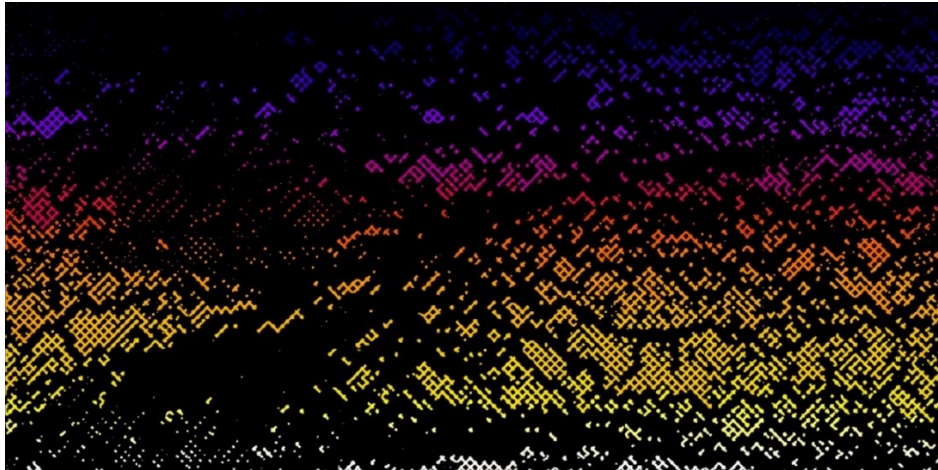


Figure 40: A sample object map, taken from of HR/T that is produced using the 3D object counter plug-in in ImageJ.

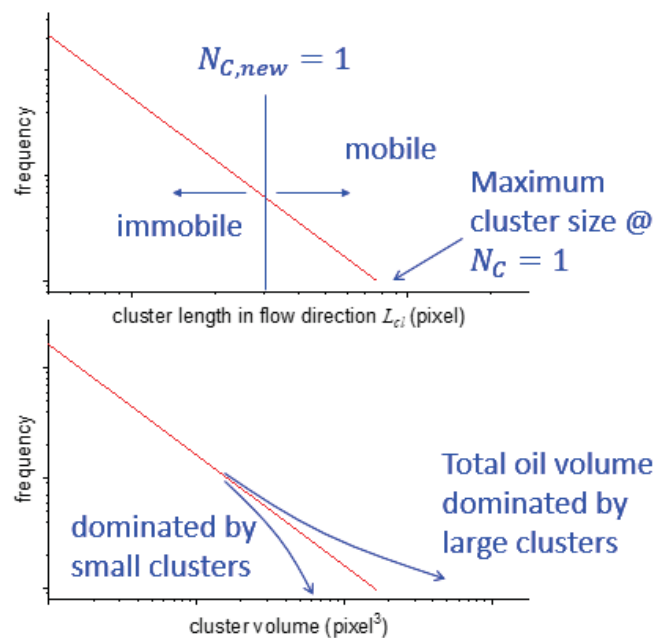


Figure 41: Cluster analysis overview (39)

Lorenz Plot

Originally derived from the Lorenz curve, the plot is an indication in the form of graphical representation of inequality of a specific property, which is the volume of the oil clusters in our case. The Y-axis of the plot is volume-weighted cumulative cluster size distribution $W(s)$ and X-axis is the cumulative cluster size distribution $P(s)$.

$$P(s) = \int_s^{\infty} P(y)dy \quad ; \quad W(s) = \frac{\int_s^{\infty} yP(y)dy}{\int_{s_{min}}^{\infty} yP(y)dy}$$

Equation 10: integrations to calculate $P(s)$ and $W(s)$, cumulative and volume-weighted cumulative cluster size distribution. P will be interpreted as the richest fraction of the population while W as the total volume of oil associated with this fraction.

The related computations were done by MATLAB script from References (92) (71).

The last point is that, as already mentioned using the area might cause some inconsistencies due to rounding error. This happened in the plotting of Lorenz curves for tertiary scenarios. In those cases, the curves were plotted using the length, which led to solving the issue.

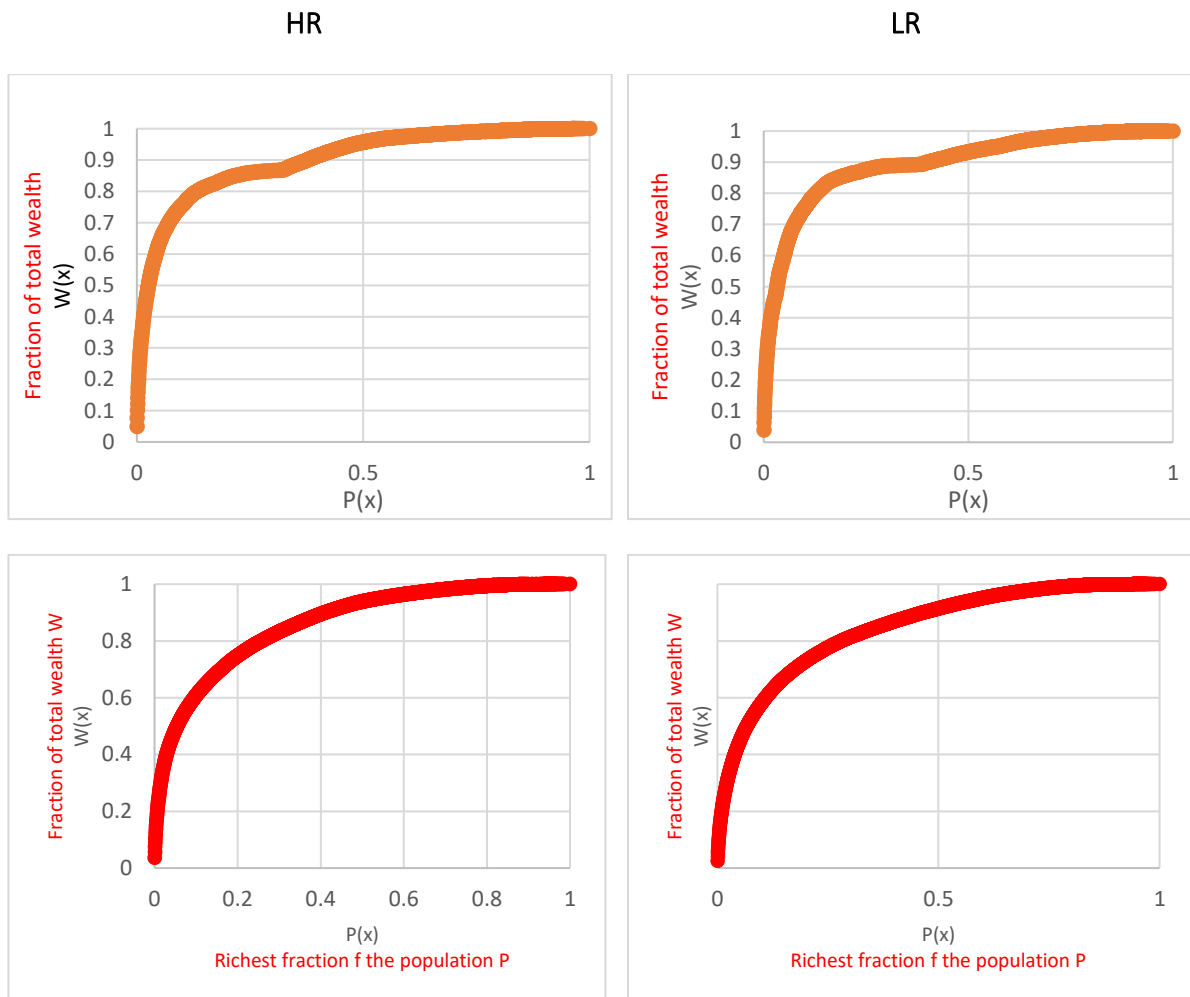


Figure 42: Lorenz Plot for tertiary scenarios using **up**) area and **down**) the length as input for the MATLAB script. Note that the inconsistency in the top curves is solved.

4.4.6 Phase Diagram

We followed the procedure defined by Lenormand to plot the phase diagram (78) and compare it with our topological phase diagram. Hence the capillary number that has been used is defined as (Equation 4)

$$N_c = \frac{Q \cdot \mu_{displacing}}{A \cdot \gamma \cdot \cos(\theta)}$$

Where Q is the flow rate, and A is the cross-sectional area of the uniform network that equals to the width multiplied by the thickness of the network (2×10^{-7} [m²]). Lenormand considers a steady-state condition with no meniscus oscillation; hence one contact angle is measured for the entire network (78). This is not the case in our experiments. Although end-state images were taken under steady-state conditions, we can find different values for the contact angle. However, there are mostly within a small range of changes. What we have done is that we calculated the contact angle inside the throats in different arbitrary ten positions in the network using ImageJ. The reported contact angle for any experiment is the arithmetic average of these measured values. An example of measuring the contact angle is depicted in Figure 43. Notice that it is only an example and not the exact representative.

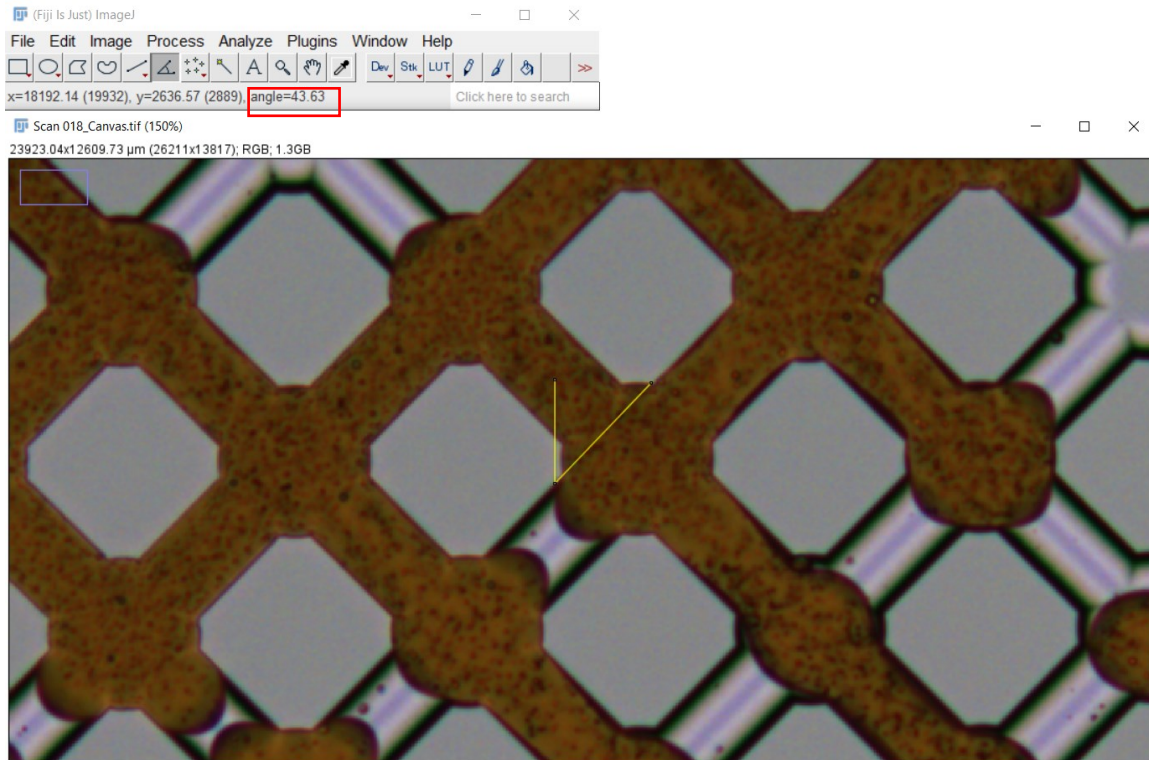


Figure 43: Measuring the contact angle with ImageJ for Low rate [0.0019] waterflooding.

Viscosities of Xanthan at different concentrations were gathered from (89). The issue was to convert the flow rates to shear rates. Although the conversion for Newtonian fluids is well defined in the literature (93) there is no straight forward conversion for non-Newtonian fluids. The approach for this thesis is to calculate the interstitial velocity of the fluid for the porous medium parameters, which refers to the main restriction in the domain, and then divides it to the pore radius. As follows:

$$\Gamma_{\text{Non-Newtonian fluid}} = \frac{Q}{\phi \cdot \pi \cdot r_{\text{aperture}}^3}$$

Equation 11: Conversion of the injection rate to the shear rate.

For the polymer floods, using the SI units, values of 26.6 and 5.13 [s⁻¹] are calculated for the two flow rates of 0.01 and 0.0019[ml/hr], respectively. Then the corresponding viscosities are read from Figure 44. The read values are represented in Table 10.

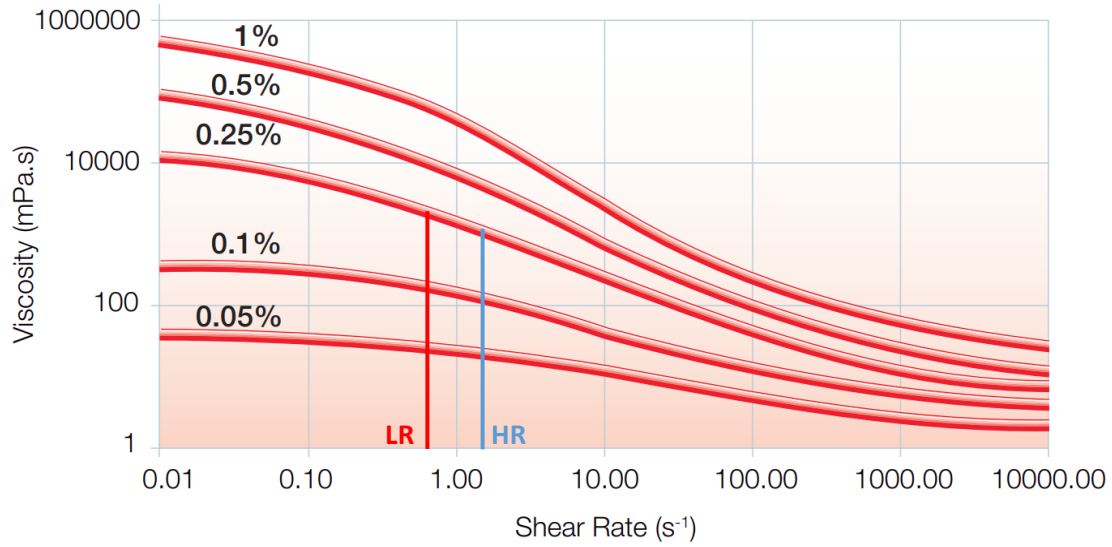


Figure 44: Viscosity as a function of shear rate for Xanthan (89) and the corresponding shear rates for high rate [0.01 ml/hr] and low rate [0.0019 ml/hr].

Table 10: Parameters of Equation 4 to calculate the capillary Number. (94)

Experiment Rate [ml/hr] / Concentration [ppm]	Fluid viscosity [mPa.s]	γ [mN/m]	θ	N_c^2
0.01/250	2.7	0.36	43.6	1.39×10^{-4}
0.01/1000	126	0.4	43.6	6.04×10^{-3}
0.01/2000	706.6	0.5	43.6	2.71×10^{-2}
0.0019/500	24.3	0.38	33.3	1.06×10^{-4}
0.0019/1000 ³	176	0.4	143.7	7.58×10^{-4}
0.0019/2000	962.1	0.5	43.18	7.13×10^{-3}

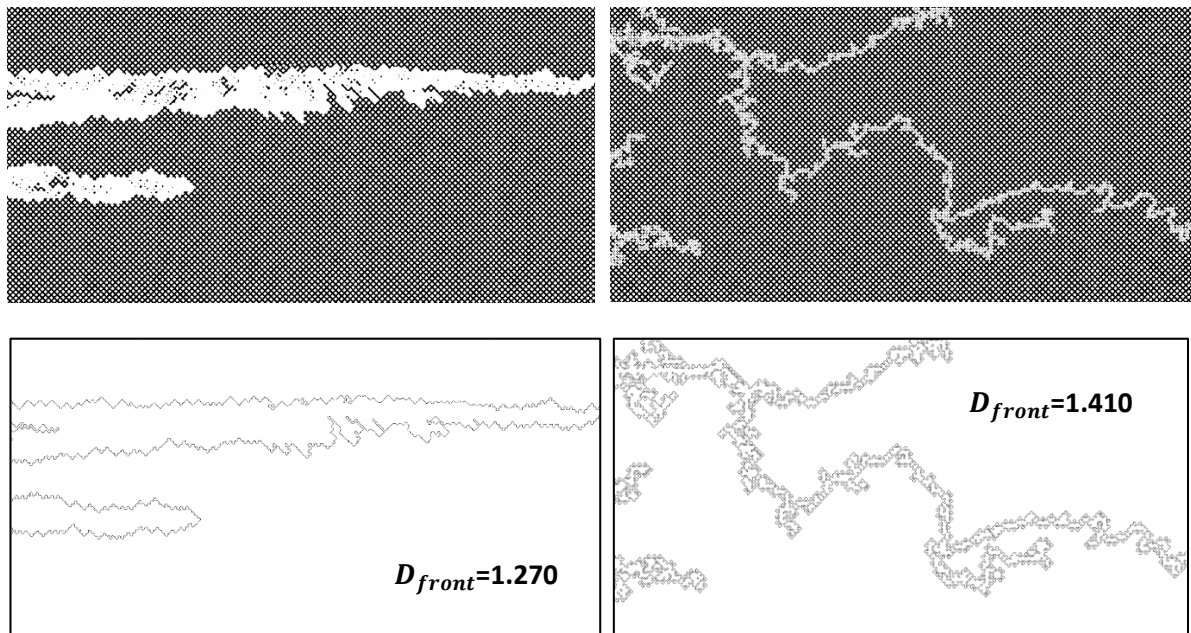
² IFT values for distilled water and 2000 [ppm] Xanthan solution was measured, and the rest are interpolated.

³ The micromodel for this experiment remained strongly oil wet during the flooding as can be seen by its different contact angle.

4.5 Interpretations of instabilities

Before going to the result chapter, it is essential to point out that in the planning the experiments was based on their injection rate and polymer concentration. We are obviously changing the capillary number and viscosity ratio, but we did not plan for a specific value of N_C nor M_μ . That is why we might not observe severe capillary or viscous fingering scenario. To have a more robust understanding, the author manually made-up two flooding scenarios corresponding to two cases of a) severe viscous fingering and b) crosslinking between viscous and stable displacement. This is shown in [Figure 45](#).

The value for D_{front} is also extracted to see the scale of its changes between viscous fingering regime and crosslinking to stable displacement regime. We will see how to use these values in [Chapter 5](#).



*Figure 45: Two made-up scenarios with their extracted fronts. **Left)** A case between viscous and stable displacement and **Right)** An exemplary form of viscous fingering. Notice that for capillary scenarios the ramification will be more and hence the RF increases.*

With the provided information, we will try to find an analogy between Lenormand results and that of ours, as is shown partly by [Figure 46](#).

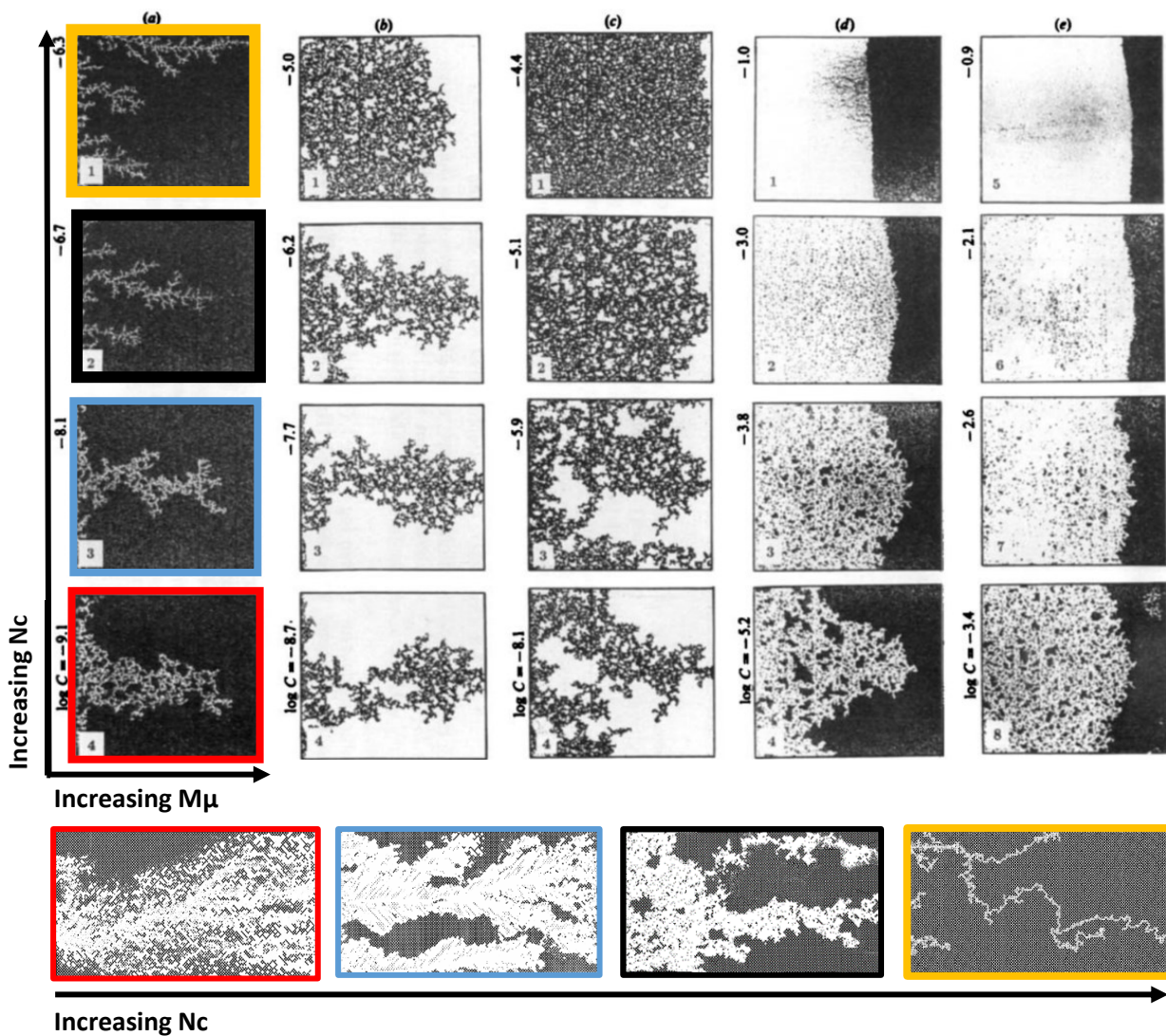


Figure 46: **Up)** Viscous (1) to capillary (4) fingering according to the work of Lenormand et al. [1988]. (a) Air is displacing a very viscous oil at $\log M\mu = -4.7$. (b) Mercury is displacing hexane at $\log M\mu = 0.7$. (c) Mercury displacing oil at $\log M\mu = 1.9$. (d) Glucose solution is displacing oil at $\log M\mu = 2$ and various Capillary number: from stable displacement analysed to capillary fingering.

Down) The experimental waterflooding at different rates of red: 0.0019, Blue: 0.01 and Black: 0.1 [ml/hr] plus the made-up scenario. Their approximate positions on the Lenormand range is also shown by their respective colours indicating cases of "Red: capillary fingering" and "Amber: viscous fingering".

Chapter 5

5. Results and Discussion

This chapter provides the reader with the results of the conducted experiments where their analyses will be discussed. The findings are divided into three main categories of statistical, geometrical and topological. However, in order to uniquely describe the fluid system, many conclusions are a combination of these three.

We go through observation of ganglion dynamics in tertiary floods, a new approach to describe flow regimes, EOR potential of water flood scenarios, homogeneity of the remained oil after flooding and the use of graph theory. Let us start this journey.

5.1 General Description of the Experiments

In total, fourteen experiments were conducted, eight of which were standardized. It means their methodology and their conducting procedure, as well as used equipment and materials, were the same. A general description of all experiments can be found in [Figure 24](#) and [Table 9](#) (Page 28). The body of evidence and findings are mainly derived from these eight, while other experiments provided supporting data and opportunity for further work. [Table 11](#) provides the general outcome of the conducted experiments.

Table 11: Results of the conducted experiments at two stages of breakthrough and end state

	Experiments	At the state of breakthrough					At the end state			
		Rate/ Concentration	Areal Sweep	RF	S _{ors}	χ_N	D_{front}	Areal Sweep	RF	S _{ors}
HR Scenarios	0.01/WF	0.75	0.57	0.055	-2000	1.2450	0.76	0.69	0.073	-578
	0.01/250	0.70	0.60	0.107	-	-	0.99	0.75	0.224	-340
	0.01/1000	0.77	0.67	0.077	-1000	1.2413	0.98	0.82	0.179	-21
	0.01/2000	0.82	0.77	0.063	-1188	1.1387	0.99	0.89	0.089	-5.5
LR Scenarios	0.0019/WF	0.45	0.38	0.058	-4974	1.4084	0.72	0.50	0.209	-705
	0.0019/500	-	0.41	-	-5262	1.2986	-	-	-	-
	0.0019/1000	-	0.48	-	-	1.733	-	0.56	-	-
	0.0019/2000	0.80	0.76	0.032	-1150	1.4938	0.97	0.92	0.052	-30
HR	0.01/Tert						RF _{tert} = 0.245	0.233	-2.95	
LR	0.0019/Tert						RF _{tert} = 0.109	0.439	-4.43	

Figure 47 shows the recovery factors at end state and the occurrence of the breakthrough. The general trend logically should be that at some point, the increase in viscosity ratio does not affect oil production. This is happening for the end state plot but not yet at the breakthrough plot.

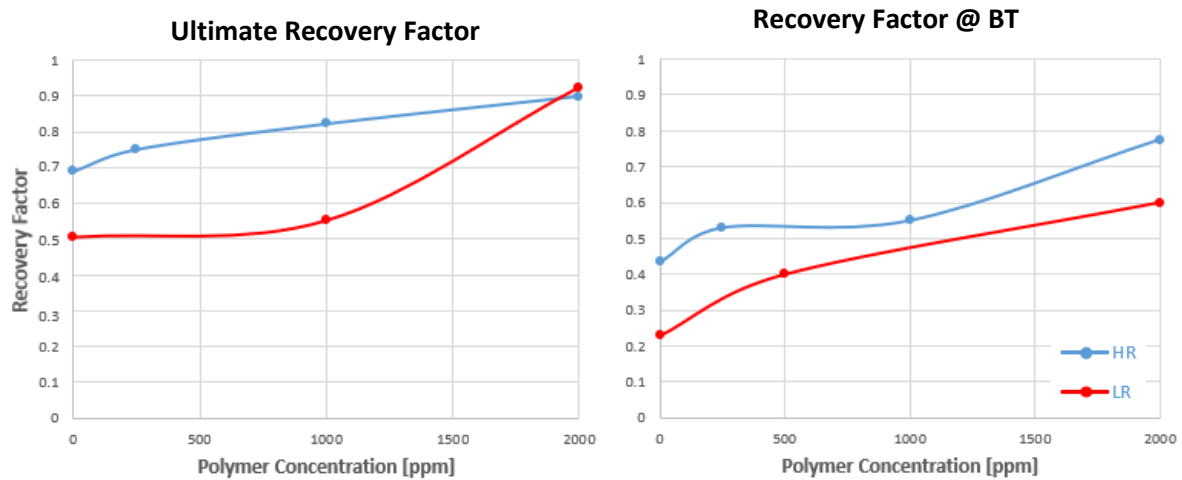


Figure 47: **Left)** Ultimate recovery factor vs. polymer concentration. As expected, the higher the concentration, the higher the ultimate recovery. For 2000 [ppm] the effect of concentration contributes more to production than the effect of the rate. We can safely assume that the behaviour of the plot is not linear, and we require more data to show it. **Right)** Estimated injected pore volume at breakthrough.

Observing Figure 47, we see that the ultimate recoveries converge into a similar value by increasing the polymer concentration, but this is not the case with the recoveries at breakthrough. That possibly could be linked to the role of time (injected pore volume) and capillary forces. The breakthrough occurs relatively very quickly before injecting even one pore volume but the ultimate RF s are gained after at least 23 injected pore volume. After the breakthrough, the displacing phase has a preferred path, hence the shape of the interface does not have many degrees of freedom to change because its structure has already been formed. Capillary fingering is deterministic and then acts toward increasing the ultimate RF until end of the production, that is why if the polymer concentration is high enough, different scenarios reach similar ultimate RF s. For the RF s at the breakthrough, the interface for different scenarios has much more degrees of freedom to propagate. It behaves chaotically and hence RF s do not converge.

With the second sight, we might be tempted to state that “expectedly, a higher polymer concentration leads to a higher ultimate recovery and slower breakthrough”. On this one we should be more cautious, because this statement is entirely based on the recovery factor. Although the values are valid, the issue is that our domain, which is the uniform micromodel with the size of 2×1 [cm²] is not a representative elementary area to have consistent results with regards to RF . Hence recovery factor alone cannot be used to evaluate the flooding. Upon this observation, we may conclude that **an evaluation based on only one variable may deliver inconsistent results, but observing different variables together, a better understanding is then could be developed.**

Take a look to Figure 48 where the different representative elementary area analyses were done for waterflooding and 2000 [ppm] polymer flooding on two rates. The x-axis is the area fraction (as a proxy for RF) and the y-axis is the normalized standard deviation ($\frac{100 \times \sigma}{sum(\sigma)}$), that refers to the scale at which fluctuation in the value of RF occurs. The fluctuation does not reach a constant value hence the model

is not a proper representative for the property of interest, in our case the RF . (To get more information on REA analysis refer to 2.5.3. Statistical Analysis in Microfluidics > REV analysis).

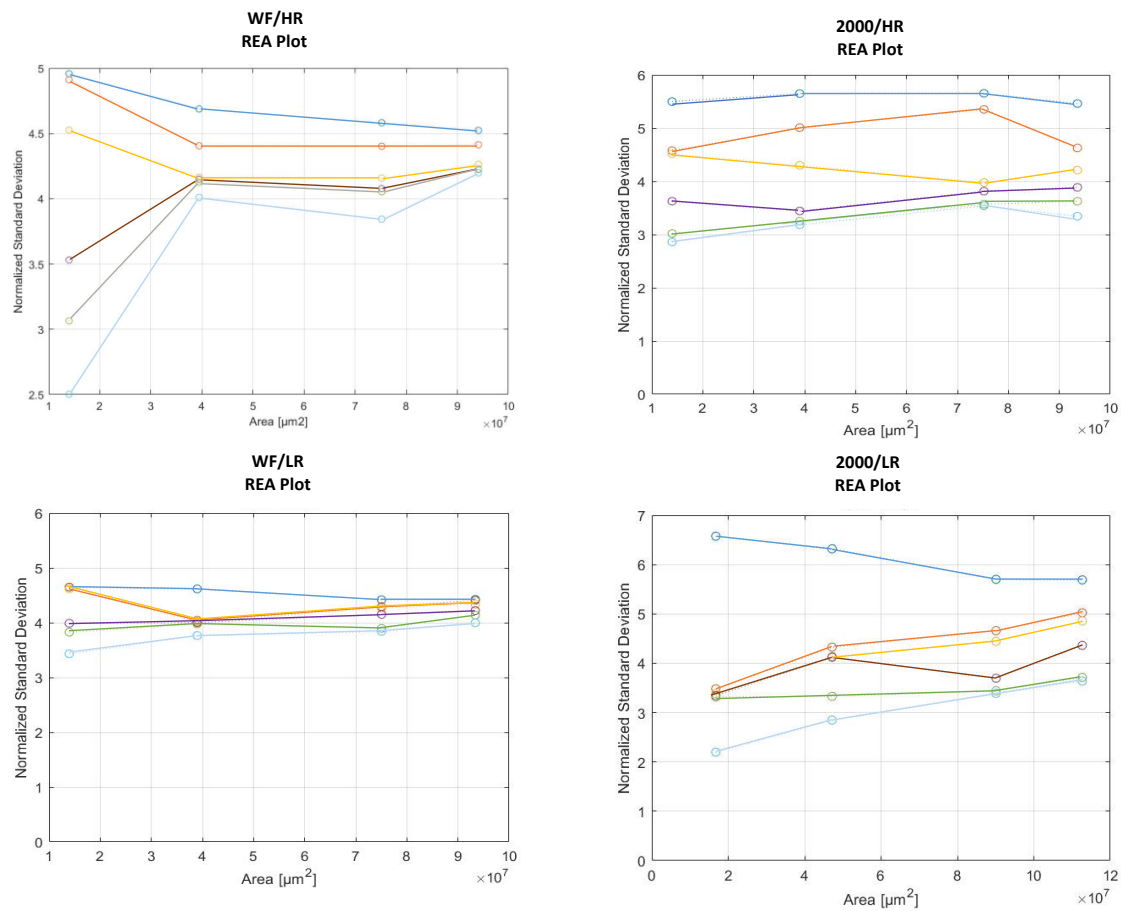


Figure 48: REA analysis for the different scenarios. An explanation to the inconsistencies with the recovery factor. Note that waterfloods show better convergence than polymer floods. However, none converges entirely.

Therefore, as a result of the observed inconsistency in the values of the recovery factor, we tried to open new fronts of investigating the flooding. Hence, we look respectively into statistical, geometrical, and topological analyses of flooding in microfluidics. We will show that a combination of these analyses has the potential of providing a comprehensive picture of the system that thoroughly describes the flooding and its related phenomena.

These analyses and the results will come in detail, respectively in the following.

5.2 Statistical Analysis

Cluster Size Distribution

Visually we could observe from Figure 49 that the lowest rate scenario leaves behind more remaining oil that is also relatively more homogeneously distributed with respect to cluster sizes in comparison to the other two scenarios. So, we should expect a Lorenz plot, more biased toward the homogeneity line. As to the 0.01 case, it looks like a crosslinking regime to a stable displacement. This looks similar to Figure 46 > blue square picture. For the 0.1 rate, instabilities are fully developed. To understand the difference, we may think of the progress of these WF scenarios.

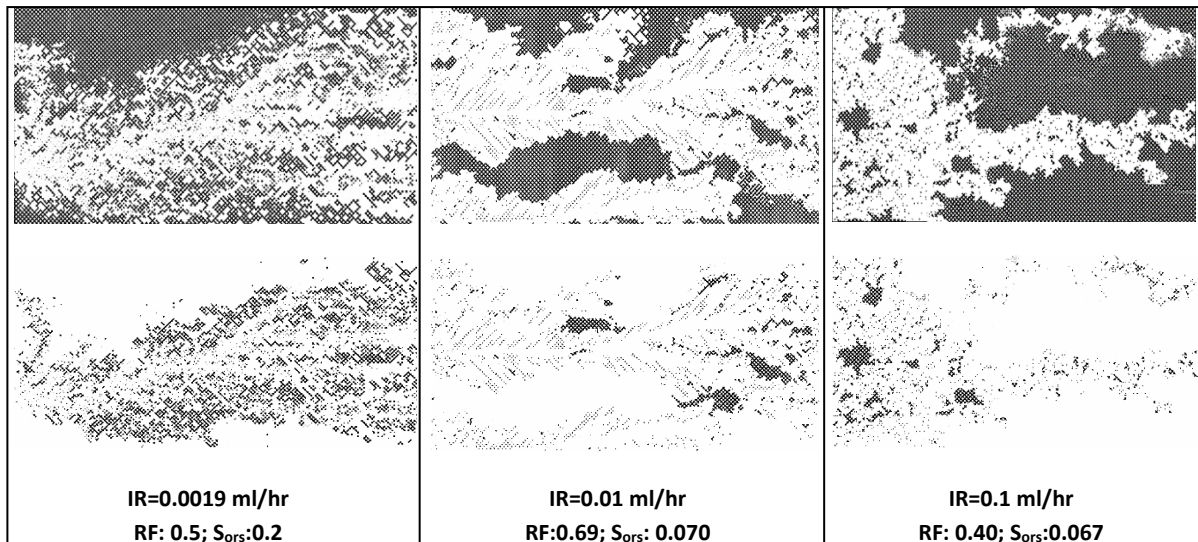


Figure 49: Up) End state of different WF scenarios and down) remained oil in the swept area (S_{ors}) at the end state. Notice the remaining oil saturation inside the swept zone at the end state. A higher rate leaves more oil behind.

In the low rate, a percolation type advancing front is happening. The capillary ramification is noticeable at each stage. That is why inside the swept zone we do not see major clusters but many small ones. In the other rates (0.01 and 0.1) we see major clusters left behind, however, from different paths. In the 0.01 scenario, various disturbances are advancing, the swept area is a result of the interaction among these fingers shape disturbances. They combine and create bigger and wider fingers while trapping oil clusters behind, or a finger creates new branches bypassing the oil while trying to find the preferred path that has the least resistance.

Note that we are deliberately refusing to use specific terminology of “viscous fingering” because within this small domain, that scenario might not be observable (Figure 14). Moreover, the viscous fingering regime is independent of pore structure but in our experiments, the visual criteria of judging the regimes depends on the pore throat structure.

As for the 0.1 scenario, by increasing the injection rate the viscous forces are stronger than the previous scenarios. That is why we have the least remaining oil in the swept zone. At the same time, fully developed fingers are shaped very soon, not giving the water phase enough time to increase the ultimate recovery factor (we cannot name them viscous fingers because they seem much wider than the thin diffusion limited aggregation (DLA) type instabilities we see in viscous fingering regime. Also the length scale of the domain is probably smaller to be able to develop viscous fingers). Hence, based on these observations and their physical reasons behind, we expect that the EOR potential of WF increases with the increase in rate. As can be seen from the remaining oil saturation inside the swept zone where higher rates leaves more oil behind. Similar statement could also be made by looking at Figure 50 where deviation from the fractal line indicates levels of size inequality of the different oil clusters. The fractal line is the mathematical fit of $a \times voxels^{-\tau}$ using OriginLab Pro.

A bias toward right (bigger sizes) then shows a greater EOR potential. In the left side a schematic black arrow shows the potential between two stages. Note that as the flooding proceeds forward, the recovery factor increases, implying that smaller clusters remain behind, which in turn means that the EOR potential decreases. In the right side the arrows show the distance between the tail of the power-law line and the biggest cluster size. Notice that as expected, the highest rate has the greatest EOR potential.

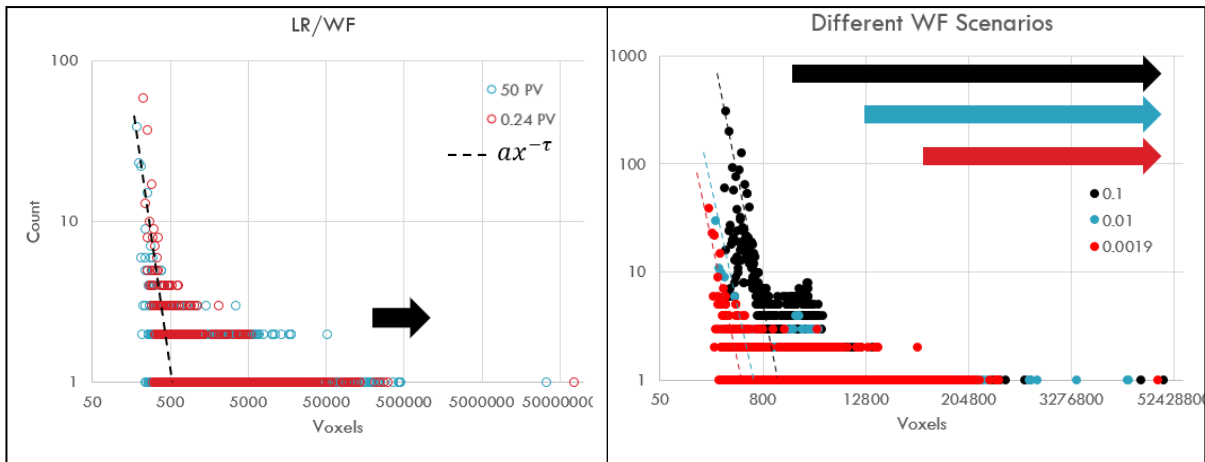


Figure 50: Cluster size distribution for WF scenarios. **Left** LR/WF cluster distribution at 0.24(red) and 50 (blue) pore volume injected. **Right** the comparison between WF scenarios with different rates@50 PV. The waterflood with 0.1 [ml/hr] has the greatest EOR potential, while the low rate [0.0019 ml/hr] has the lowest. **Left** EOR potential decreases with lapse of time and continuation of flooding. That is why the red distribution (@ 0.24 PV left image) is biased toward right more than the blue distribution (@ 50 PV). Note that the term voxel that stands for volume pixels is only based on ImageJ terminology and not a real volume. In our 2D images, this so-called voxels are only the number of pixels counting the area.

Concerning the role of polymers, once it is added to the water phase, we expect that it prevents the rapid creation of finger onsets, giving the front a more stable advance that makes the remained oil more homogeneously distributed. From this viewpoint, a major difference between WF scenarios and polymer flood scenarios should be expected. This, we judge by the Lorenz analysis.

Lorenz Analysis

Figure 51 compares the Lorenz plot for different waterflood scenarios and 2000 polymer floods. As a measure of heterogeneity, the closer the curve is to the diagonal line the more homogeneous are the oil clusters with regard to their volumes. Now, if we draw a horizontal line from $W(s)=0.96$, it intersects the 0.1 scenario at $P(s)$ 1%. It tells us that only one percent of the population owns 96 percent of the wealth (96 percent of the remained oil sat in one percent of the clusters). While this value is 8% and 28% for 0.01 and 0.0019 scenarios respectively. This confirms the results from Figure 50. That the lower the rate, the greater the EOR potential at the end state of water flooding. As for the 2000 scenarios, although the curves are very similar, the oil is distributed more homogeneously in the higher rate. This is due to the smaller areal sweep of the low rate scenario (Table 11) where a major cluster has been left behind, as could be seen by Figure 52. Hence, in the Lorenz analysis, the difference between the 2000 flooding scenarios does not come from their potential of mobilizing oil clusters but the percentage of the areal sweep.

Following the works of Kharrat (39) and Ott et al. (13), the cumulative cluster size distribution for secondary flooding has been plotted in Figure 53. As to the HR (0.01 ml/hr) scenarios, 250 [ppm] does not show much difference with the waterflood.

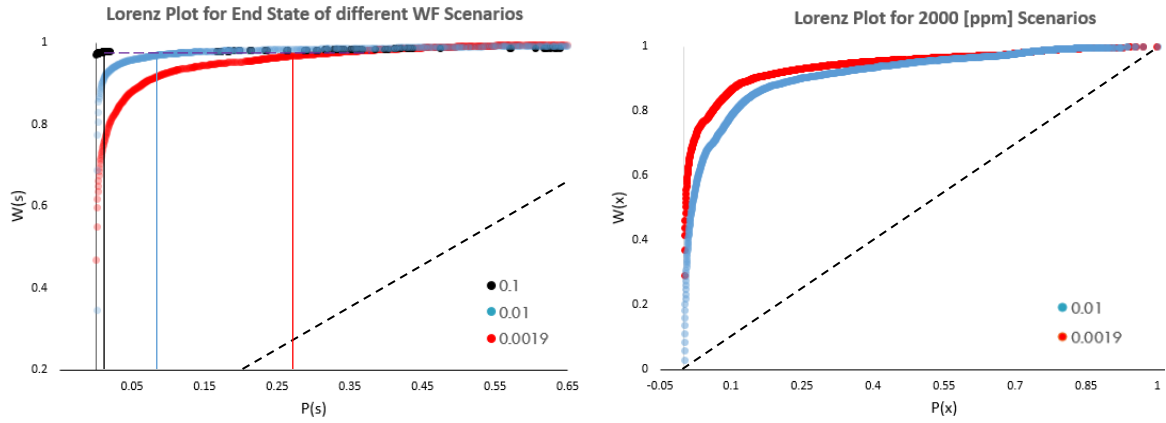


Figure 51: Lorenz plot for end states of **left**) different WF scenario and **right**) 2000 [ppm] polymer floods. Notice that, as expected, in WF the least heterogeneous scenario is 0.0019 while it is 0.01 in polymer flood. The black dash line is the 45° homogeneity line. **Left**) The axes length has been adjusted for better visualization.

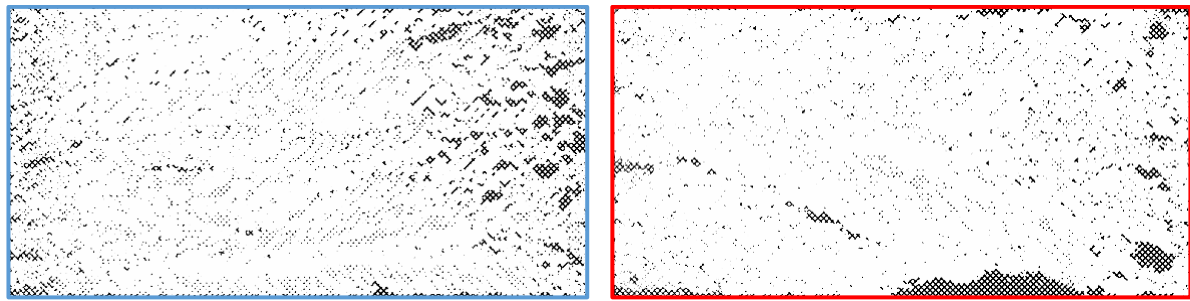


Figure 52: Comparison between the end states of 2000 scenarios. The right is the low rate [0.0019], while the left is the high rate [0.01]. Notice that a major cluster is left behind in the low rate owing to the smaller areal sweep.

As for the Lorenz plot in [Figure 53](#), we see that increasing the concentration shifts the plot closer to the homogeneity line which is understandable. Because the increase in the viscosity of the water phase in polymer scenarios will cause the mobilization of smaller clusters of the oleic phase ([Equation 12](#)). Therefore, clusters that are remained after polymer floods will be smaller than those remained after waterflood. In the Low rate scenario, however, because of the smaller Darcy velocity, the effect of higher viscosity is neutralized, making the two plots getting closer.

$$\text{Maximum cluster length} \leq \frac{P_b K}{\mu_w \cdot v_{Darcy}}$$

Equation 12: Estimation of the maximum cluster length from macroscopic capillary number (81) (73). P_b is the breakthrough pressure from the capillary pressure curve. K is the permeability. μ_w is the water viscosity, and v is the Darcy velocity.

Although the Lorenz plot of LR/0 and LR/2000 are quite similar, we know that there is a major difference between their ultimate RF, the saturation of remained oil in the swept zone, and the areal sweep. That is a major motivation to use other techniques to characterize the fluid-structure as is done in the geometrical analysis.

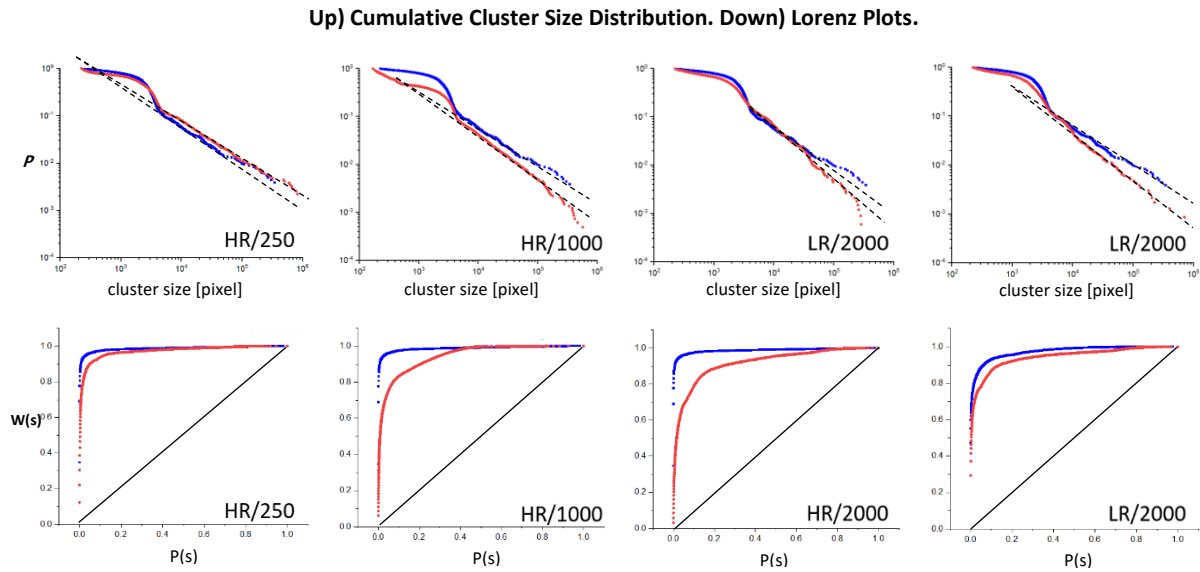


Figure 53: **Top row)** Cumulative cluster size distribution for secondary polymer floods (red) and WF (blue) with the dash lines correspond to power-law fits by a maximum likelihood approach. **Bottom row)** Lorenz plot and the 45° homogeneity line for the same data set.

Core observations of the statistical analysis.

- ✓ In WF scenarios higher injection rate causes a larger amount of oil to remain in a small fraction of clusters.
- ✓ In WF scenarios, for the 0.0019, 0.01 and 0.1 rates [ml/hr], the sweep efficiency is controlled by a percolation type advancing front, where the viscosity ratio is responsible for shaping different patterns.
- ✓ The end state in all scenarios shows relatively high heterogeneity with regard to the area of the remained oil clusters. However, the system becomes relatively more homogeneous the higher the polymer concentration.

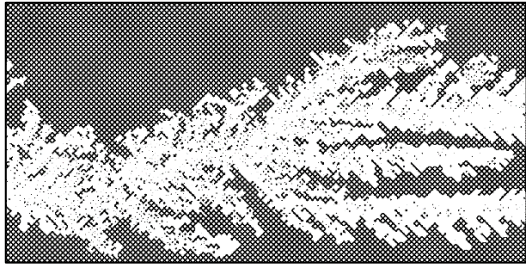
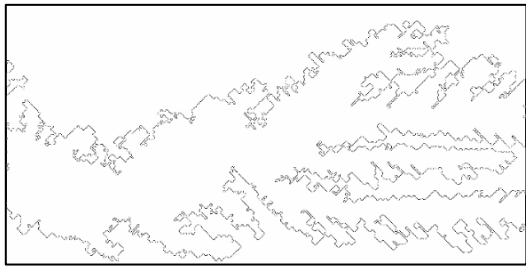
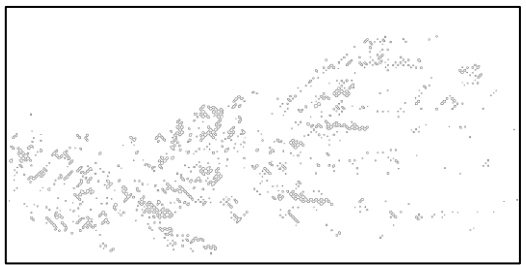
5.3 Geometrical Analysis and Fractal Dimensionality

The main argument of this subchapter is that fractal dimensionality provides a strong tool to characterize the complexity of the advancing front. However, this was not done by the fractal number of water (D_W) nor oil (D_O). But by the fractal number of the front (D_{front}), which corresponds to the outer perimeter of the areal sweep.

Many vain attempts were made to explain the complexity of fluid phases, using the D_W and D_O . But we concluded that at best, they give us a vague idea regarding the complexity of the total fluid phase. And that is understandable because many factors are influencing the value of D_O and D_W at the same time. Namely, the geometry of the pore network, the saturations of two fluid phases, the growth in the areal sweep, and the residual saturation. These factors sometimes exert their influence in opposite directions. For example, a higher recovery factor means higher residual oil saturation as well. While the RF is attempting to decrease D_O , the S_{or} is trying to increase D_O . Hence, a clear trend that explains the complexity of one of the fluid phases could not be achieved based on D_O or D_W .

This was the main motivation to separate these factors by morphological image analysis so that a clear trend could be achieved. Separation of these factors is done by the extraction of different images from the original binary image. For any of these images, we can calculate fractal numbers. Please take a look at [Table 12](#).

Table 12: A sample image (LR/O @ 0.24 injected pore volume) and the corresponding fractal numbers and extracted images

Image	Terminology And value	Explanation
<p>This is the original binary image after the opening process. This image alone gives us 3 different fractal numbers</p> 	D_o 1.8258	<p>Directly related to the oil phase and indirectly to other factors.</p> <p>It is calculated assuming that the background colour is white, and the fractal shape is black</p>
	D_w 1.877	<p>Directly related to the water phase and indirectly to other factors.</p> <p>It is calculated assuming that the background colour is black, and the fractal shape is white</p>
	D_N 51	$D_N = D_{oil}/Area$ *Area= ratio of black to white pixels
	D_{front} 1.4164	<p>Directly related to the complexity of the front</p> <p>Porous medium and residual oil are removed.</p>
	$D_{residual}$ 1.4899	<p>Directly related to the complexity of the residual saturation.</p> <p>Porous medium and the front are removed.</p>

We have no choice but to investigate the behaviour of D_o and D_w , because these two values are the ones traditionally studied in the literature.

Evolution of Body Fractal Numbers Through Flooding: Complexity of Fluid Phase in the Pore Network

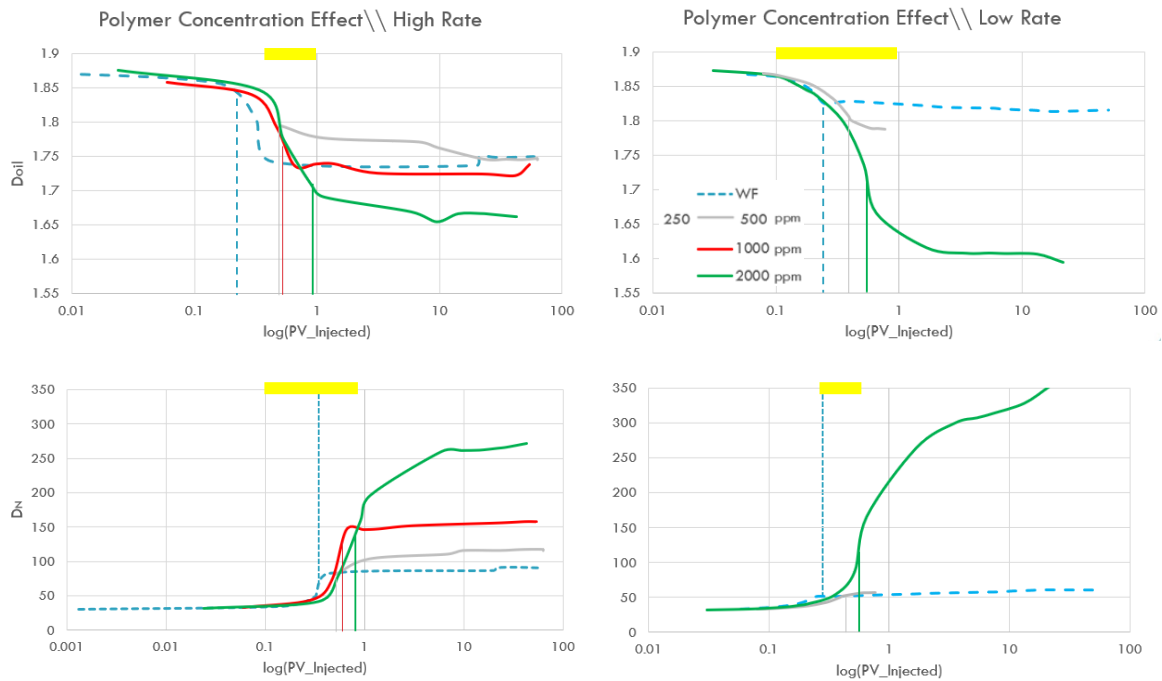


Figure 54: Down) Evolution of Normalized Fractal Dimension (D_N) and Up) for different scenarios. The vertical dash lines are the moments of breakthrough occurrence. The highlighted lines are pointing out the radical shift in the values of fractal number.

Figure 54 represents the evolution of D_O and D_N for different scenarios. The values of D_O for all scenarios start within the range of [1.86-1.9] following the literature (11) (15) (58) (63). The differences are likely because of the variations in the quality and dimensions of the images. Using the value of area% (ratio of black pixels to white pixels in a binary image), a normalized fractal number is defined with more sensible numbers that make it easier to compare different scenarios. Furthermore, the normal fractal number follows the behaviour of D_W which is helpful, considering that due to practical issues, calculation of D_W was not always possible. Eventually, usage of a D_N will omit the error introduced to the calculation by variation in the sizes of images. Hence, as can be seen, all scenarios start from the same initial value (~ 30). Moreover, D_N shows a trend similar to D_W . Keeping in mind that ImageJ could not always calculate the values of D_W that is pertaining to the error associated with fitting the data to the power equation $N \propto \tau^{-D}$. Where N is the number counts for foreground colour in calibre size τ . D_W is calculated using the foreground colour as white, hence in the early stages of flooding where there is a few white pixels, the data cannot be properly fitted to the equation (Figure 33)

Another considerable point is the trend of the curves and the physical meaning behind it. So as depicted, the x-axis represents the injected pore volume that can be seen as the lapse of time too. As already stated in **Literature Review**, the removal of the initial fluid in place (in our experiments, oil) increases the fluid phase complexity. **This increase in complexity has been characterized by a downward trend of D_O and an upward trend of D_N , respectively** as is shown in Figure 55.

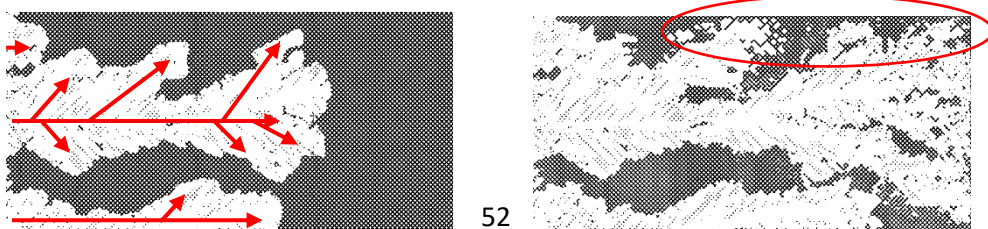


Figure 55: HR/0 scenario. **left**) before the breakthrough, notice that the front is not ramified and yet it is not stable entirely. **Right**) Subsequent end state, notice that previous instabilities are fully developed shortly after breakthrough and then the capillary fingers have the opportunity to grow and cause capillary ramification.

The complexity to link the fractal number of the body of the fluid to understandable concepts was the motivation to separate the external players from the scene and extract a fractal number that solely explains the front stability.

Evolution of Front Fractal Number (D_{front}) During Flooding: Categorization of Displacement Patterns

From the possible flow patterns, the observed ones in our secondary floodings seem to be mainly capillary fingering with the $M\mu$ contributing to the stability of the front., and stable displacement. These patterns are shown in Figure 56, and their features have been discussed further.



Figure 56: Sequence images of the displacement patterns and flow regimes as a function of polymer concentration and injected pore volume. The viscosity ratio ($M\mu$) is 2.9, 2.13 and 0.003 for the LR/2000, HR/2000 and waterflood scenarios, respectively. Red values in bracket are front fractal dimension while the blue percentages are their place in provided instability range, [1.0402-1.4668] so that the numbers are better felt.

LR/0 Capillary fingering: The experiment is characterized by its $\log M\mu < 0$, $[C_p] \ll [C_p^*]$ and $Nc \sim 10^{-6}$.

The instabilities, in general, are sensible to the rate. In the LR scenario, capillary forces cause ramification and a percolation type advancing front that does not necessarily progress toward the direction of the flow. The rate is still not high enough to develop clear viscous fingering. The channels are the result of viscous versus capillary forces.

HR/0 Crosslinking regime: The experiment is characterized by its $\log M\mu < 0$, $[C_p] < [C_p^*]$, and $Nc \sim 10^{-5}$. Viscous forces are strong enough to overcome capillary forces. Hence, they possess a stabilizing effect by suppressing the formation of capillary fingers. Meanwhile, instabilities are developing since a less viscous fluid is displacing a more viscous fluid.

Provided that $M\mu$ is constant (waterflood scenarios) the capillary number explains the flow patterns that can vary within different order of magnitude in capillary dominated flow regime. [Figure 57](#) shows a range of patterns from slightly capillary dominated ($Nc = 8.28 \times 10^{-6}$) to instabilities that look like less capillary and more viscous dominated ($Nc = 5.44 \times 10^{-4}$).

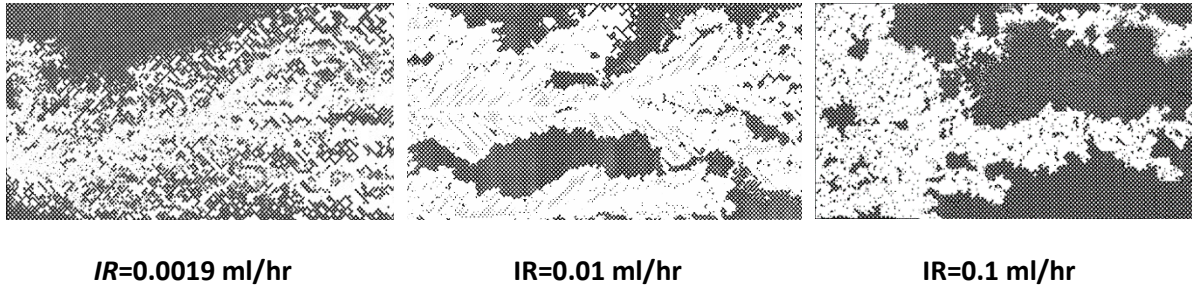


Figure 57: Waterflood scenarios and rate sensitivity. $M\mu = 0.003$ for all scenarios.

(2) Stable front: $\log M\mu > 0$, $[C_p] > [C_p^*]$, there is no noticeable sensitivity in the behaviour to flowrate, which means that the pattern is independent of Nc . The displacement is stable regardless of the viscosity ratio ($M\mu_{LR} = 2.90$ and $M\mu_{HR} = 2.13$) *as if above a critical polymer concentration (C_p^*), the stabilizing effects of polymer overcomes the instability caused by viscous or capillary forces.*

Fractal dimensionality and Lenormand phase diagram

Now, if we use the front fractal number versus recovery factor, the zones in which different patterns occur, are better represented. Note [Figure 58](#), where we have tried to translate the Lenormand phase diagram into our plot to find analogy and clear patterns.

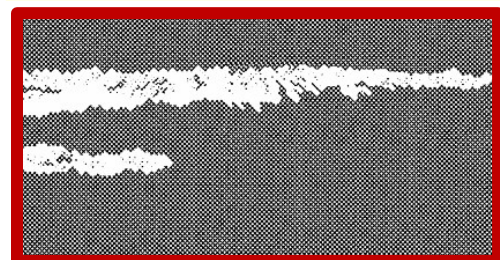
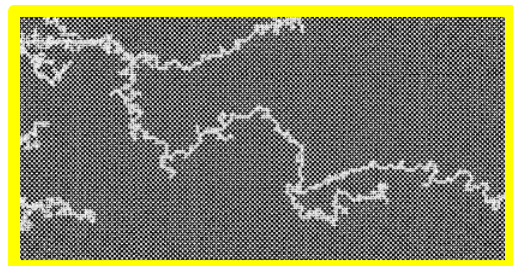
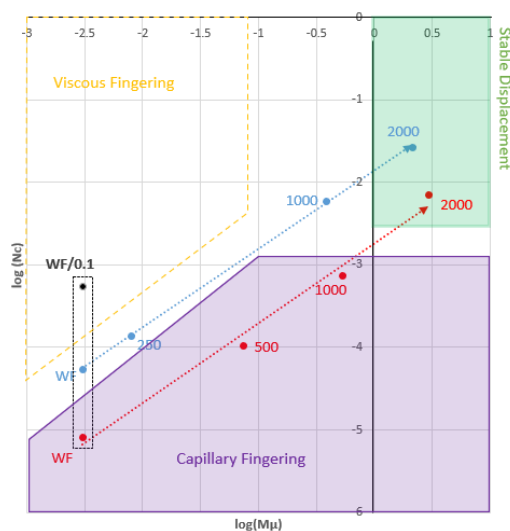
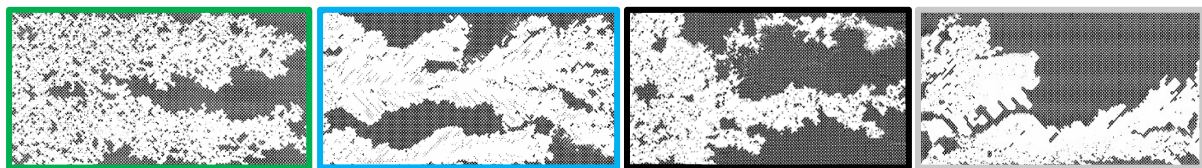
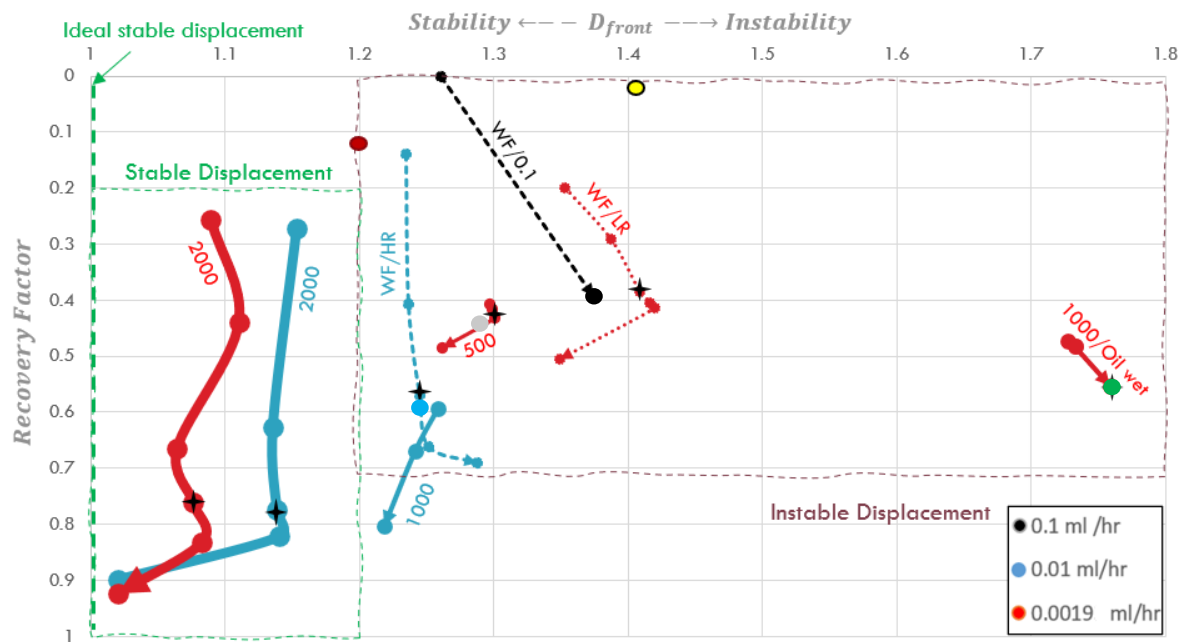


Figure 58: Lenormand phase diagram (left > down) and its translation into D_{front} vs. RF diagram (up)

Numbers are polymer concentration in ppm. $M\mu$ is the viscosity ratio as a proxy for the mobility ratio. Perfect displacement is considered to have the D_{front} equals to 1. We do not reach it, owing to the fact that the experiments were conducted in a porous medium. Note that both capillary and viscous ramification have higher D_{front} than the stable displacement. The difference could be the RF. Severe viscous fingering scenarios have a small RF. Stars are the estimated occurrence of the breakthrough. One status of different scenarios are shown in the translation plot with their respective colour. The first one represents a simple viscous fingering scenario while the latter representing crosslinking between viscous and stable displacement scenario. To see the calculation for the Lenormand phase diagram refer to [Table 10](#).

Here we try to describe these zones further. Let us see the general trends and features in [Figure 58](#) that were not mentioned beforehand.

- **The ideal stable frontal advance, where any growth of protuberance in the front is suppressed, is characterized as a straight line on $x=1$.** Obviously, in a real porous medium we will not reach this line.
- For waterflood scenarios (and probably we can safely assume for low polymer flood scenarios as well) the instability grows before the breakthrough. What happens afterward depends on RF (if the front has left the porous medium or not) and capillary number. So, once the water production starts, the ramified front leaves the model, and this reduces D_{front} . For the HR case, instability continues to increase after the breakthrough because the capillary ramification now has the opportunity to develop. ([Figure 59](#))

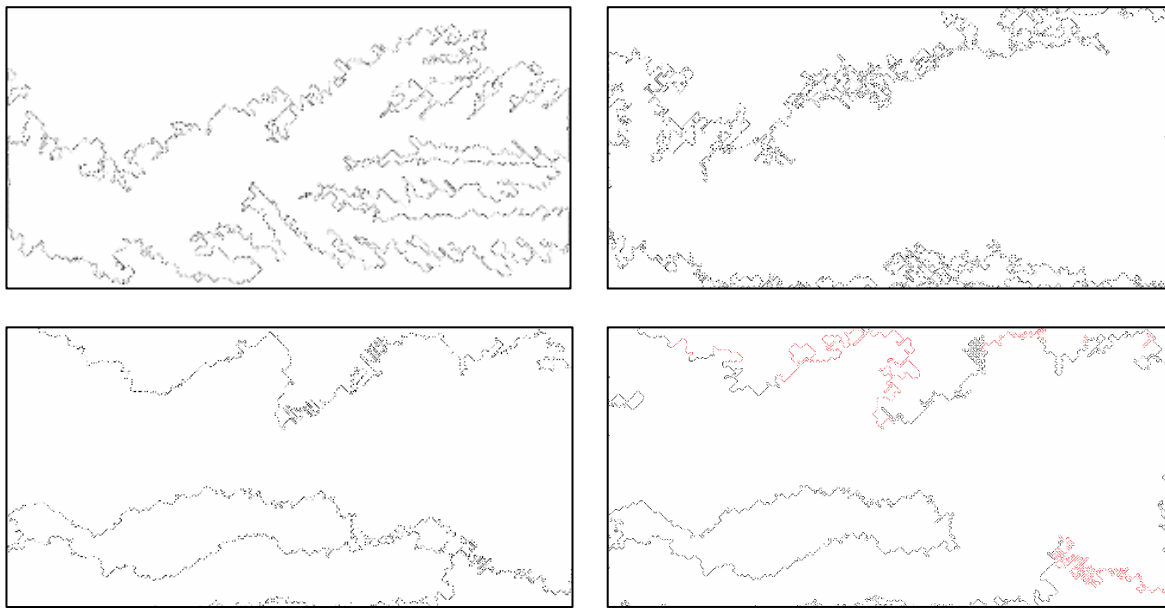


Figure 59: Top) LR/O shortly after breakthrough and subsequent final image. Notice the removal of the branched front in the final image. Down) HR/O after breakthrough and subsequent final image. Notice the small branches over the perimeter in the final image.

- As for the stable front zone, in which there are 2000 [ppm] polymer floods, both HR and LR scenarios follow the same trend. However, as expected, the one with a higher viscosity ratio develops a more stable frontal advance. Unlike the WF scenarios, before the breakthrough, stability increases. This could be linked to having different entry zones to the porous medium, each of which develops a separate front. Soon they connect and create one major stable front that progresses forward ([Figure 60](#)). At the microscopic level, the author assumes that the cooperative pore filling phenomenon plays a significant role in suppressing oil cluster trapping, which leads to a connected front. Both polymer flooding scenarios start to develop fingers around the breakthrough. We do not know when it starts. Because we have only images shortly before and after the breakthrough. If we assume these fingers occurs after the breakthrough, then it could be because now the water phase has a preferred path and follows it. **However, if we assume that the onset of fingering starts before the breakthrough, it could be due to polymer retention.** Because of the retardation of polymer agents, the mobility ratio will change locally, and fingers start developing at the point of highest mobility contrast. But for now, all we can say is that we require more data to be sure what is exactly happening.

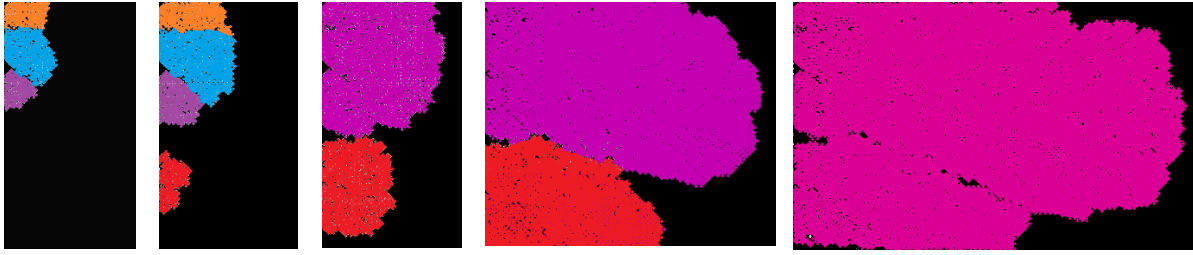


Figure 60: Frontal advance in LR/2000. Oil is shown by black colour, and grains have been removed for better visualization. Notice the separated fronts entering the micromodel and the formation of the subsequent combined stable front. Compare this with the final state of 0.1 waterflooding (Figure 57) where the two fully developed fingers reached the breakthrough before having the chance to merge into each other.

- Eventually, the exact boundaries of these zones depend on the pore distribution of the network. The application of this plot is then limited by the geometry of the domain and pore (and throat) size distribution as well the resolution of the images. The effect of these factors are yet to be investigated.

In a nutshell, the newly introduced technique uses two of the Minkowski functionals to describe the flow pattern. Namely, area (saturation) and indirectly the perimeter. We do not use the perimeter directly, but we use the fractal number that describes the complexity of the external boundary (perimeter) of the interface.

Table 13: A comparison between the translation plot and that of Lenormand

Lenormand	Translation Plot
<ul style="list-style-type: none"> • Calculation of capillary number is necessary 	<ul style="list-style-type: none"> • No calculation of the capillary number • Image analysis techniques are employed
The entire flooding is considered as one point, so regime change and onsets of instabilities during the flooding will not be captured.	Flooding path can be plotted and onsets of fingers could be captured.
Physic is the foundation for the diagram	The foundation is related to the fractal geometry
<ul style="list-style-type: none"> • Depending on the pore size distribution and sizes of the network, the boundaries of the domains change. Still, the general shape of the zones remains constant (78) 	<ul style="list-style-type: none"> • The effect of pore size distribution and sizes of the network are yet to be investigated. • The effect of resolution leads to changing the boundaries (lower resolution causes a smaller range of fractal numbers), but similar to the Lenormand technique, the general shape of the zones remains constant.
Phase diagram only corresponds to the flow regime before the breakthrough	The plot can be employed even after the breakthrough, however with lower accuracy

Core observations of the geometrical analysis.

- ✓ By extracting the fractal number of the perimeter of the areal sweep (called D_{front}) a plot of D_{front} versus RF was used to make a connection between the flow regime and the actual behaviour yielding good results for the given cases.

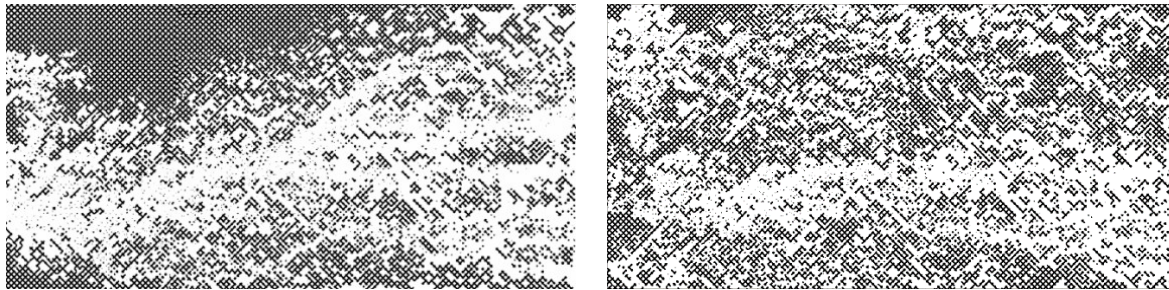
- ✓ The application of the fractal number of the body of the fluids (D_o or D_w) does not provide a reliable, unique description of the complexity of one fluid phase.

5.4 Topological Analysis

As far as this, we have analysed polymer flooding statistically and geometrically. Although valuable information was extracted, we still need the topology to describe our system unequivocally, and, in this section, we provide the reader with the data that was obtained from the topological analysis. This data includes the characterization of the connectedness of the oleic phase and Euler characteristic relationship with cluster mobilization. Moreover, production curves are included here, because saturation in 2D is equal to the volume in 3D, which is the zeroth Minkowski functional.

To start, we explain the necessity to use χ_N and the method to validate its calculation.

5.4.1 Euler Characteristic



$D_N:61.2, D_o:1.8155, D_w:1.8818, RF:50.9\%;$
 $\chi_N=-784$

$D_N:61.5, D_o:1.8207, D_w:1.8822, RF:50.7\%;$
 $\chi_N=-19$

Figure 61: The comparison between LR/O after 51 injected pore volume(left) and the subsequent LR/T after the introduction of polymer agent(right). Notice the similar values of fractal dimensionalities and recovery factors, as well as the major difference in Euler characteristics. In accordance with the literature, the growing number of isolated clusters causes a shift toward greater value for χ_N .

Figure 61 is a good example that drastic changes in the topology of the fluid do not necessarily alter the fractal dimension or recovery factor with the same order of magnitude. Hence, any characterization approach should consider the Euler characteristic.

To validate the computed values for χ from experimental data, we use the graph theory to calculate the pore space χ_{ps} . We know that at the initial stage where the micromodel is 100% oil-saturated, there is only one phase that has already filled all pores and throats. **Hence at the initial status, the topology of the fluid is the same as that of the pore space.** Check the following image which shows the lattice design for a uniform micromodel. Using graph theory, we calculate the value of $9702-19404= -9702$ which is in very good harmony with the values extracted from images of the experiments (~ -9800). So, we expect that all experiments start from a similar initial point. In practice, however, there is always a small error.

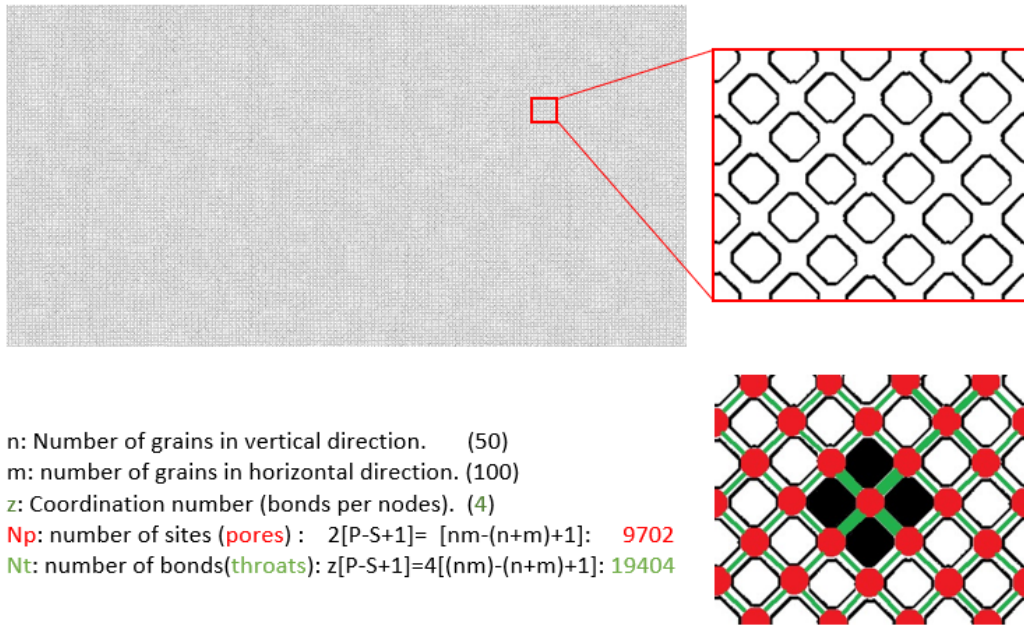


Figure 62: Lattice design for a uniform micromodel and calculation of X_{ps} . **Top>left**) a clean uniform micromodel. **Right>top** a zoomed-in area and **Right>down** the same area characterized by different colours for pores, grains, throats and the coordination number for better visualization. Values belong to the entire domain.

Evolution of the χ During Flooding Scenarios

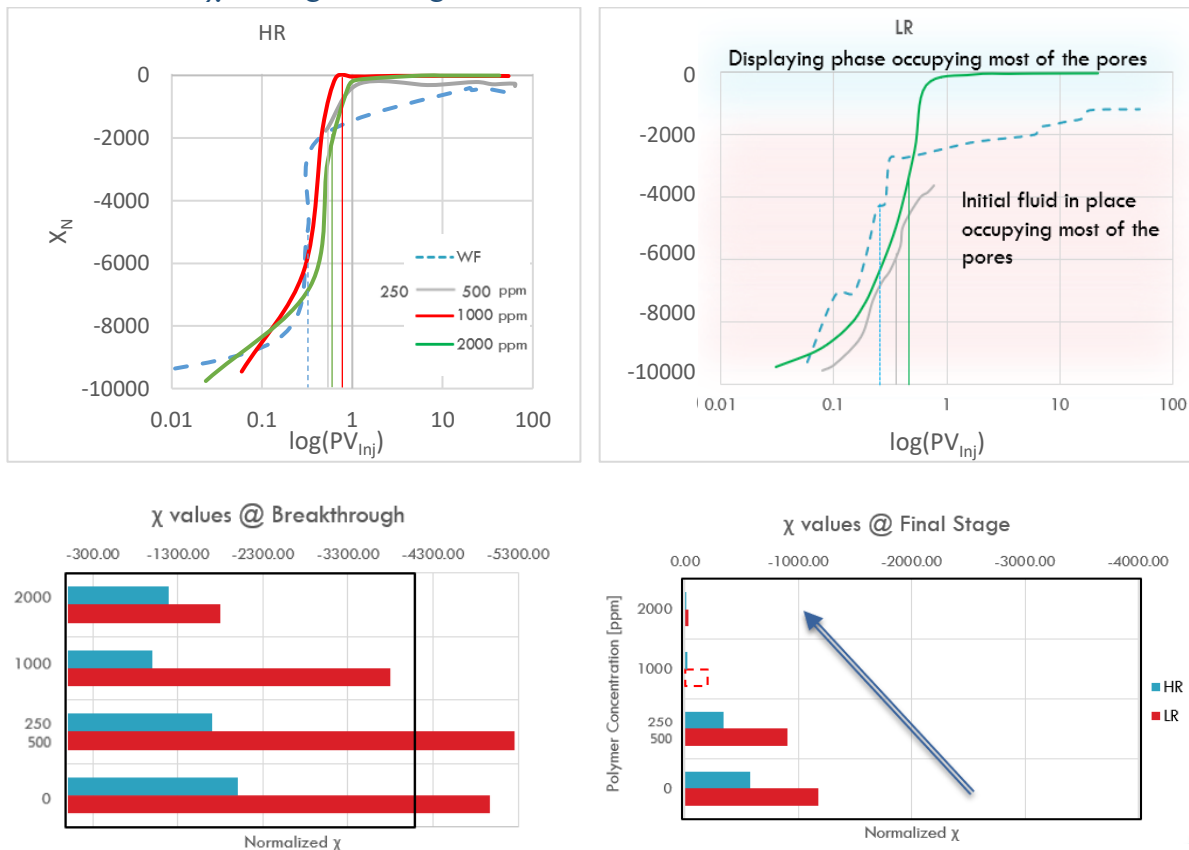
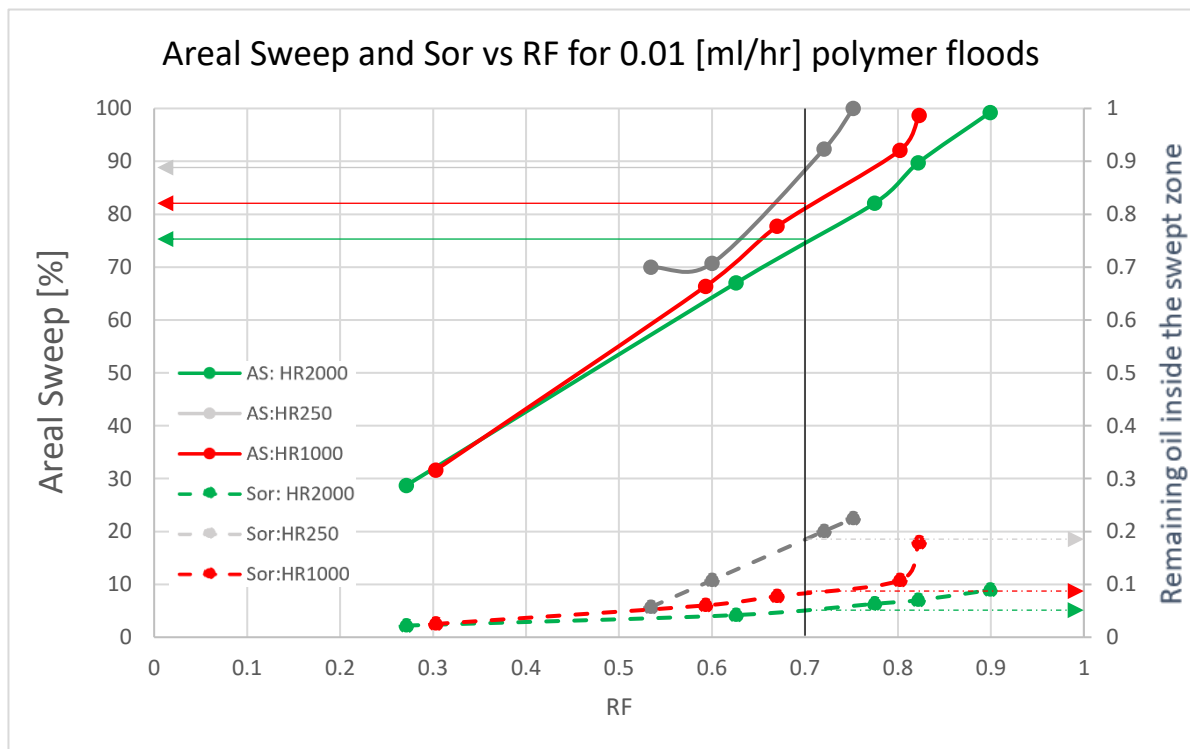


Figure 63: **Top**) Evolution of χ_N for different scenarios. The straight lines are showing the moment of breakthrough. Notice the radical changes of topology around breakthrough: an indication of discontinuity of the oleic phase. Note that plots are semi-log, which means the main topological changes or in plain language fluid rearrangement is taking place mainly before the breakthrough. **Bottom**) Comparison between values of χ_N at breakthrough and at the end state of different secondary flooding scenarios.

General trends are clear in [Figure 63](#). Changes in topology start at the moment of the introduction of the displacing phase into the system. The radical changes happen before the breakthrough and at most, continue shortly afterward, although changes for WF scenarios continue with a gradual rate even after the breakthrough.

While the recovery factor increases, smaller clusters are left into the system that could not be recovered and that is why the Euler characteristic goes up. Notice that the higher the polymer concentration the more disconnected is the oleic phase. This is better depicted by the plot of RF versus χ_N ([Figure 66](#)).

Unsurprisingly, there is a relationship between polymer concentration and breakthrough, as well as the time (PV_{inj}) at which χ_N reaches a maximum. So, the higher the concentration is, the later breakthrough occurs, and the sooner the oleic phase becomes internally disconnected the most. In plain language, we are producing the majority of the oil while reaching the maximum areal sweep. Interestingly there is not much difference between polymer flood scenarios with respect to their χ_{max} , while there is a major difference among their RF results. This could be interpreted as, *although within our range of capillary number, even low concentrations of polymers maximize the areal sweep, oil production is controlled by mobilization of oleic clusters inside this zone*. This is clearer depicted in [Figure 64](#).



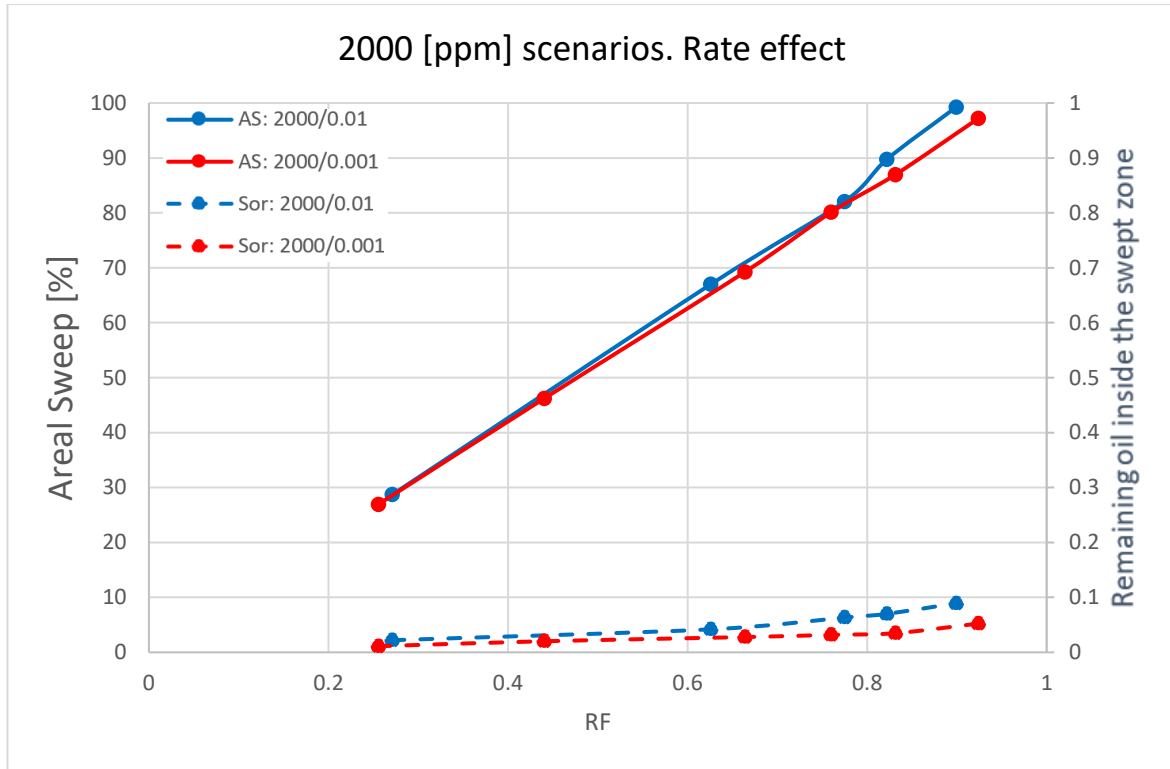


Figure 64: Areal sweep (left axis) and remained oil saturation inside the swept zone (Sors, right axis) vs recovery factor for up) different HR polymer scenarios and down) Rate comparison.

Up) Notice that at the same RF, HR/2000 has the minimum swept zone and Sors. An indication that oil production is mainly governed by the mobilization of clusters inside the swept zone and not necessarily by maximizing the areal sweep. Down) The effect of polymer concentration is strong enough to prevent major differences between two scenarios, however the low rate sweeps the field cleaner, leaving lower S_o behind.

Cluster Mobilization and Fragmentation

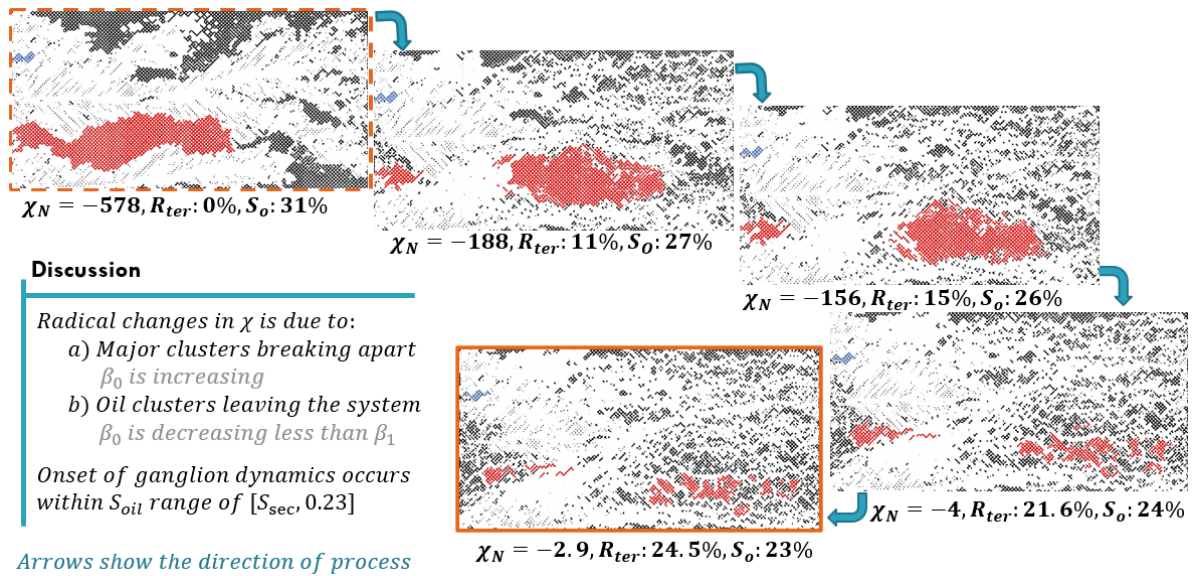


Figure 65: Image sequence during HR[0.01]/T, depicting cluster fragmentation and ganglion dynamic. Oil clusters are mobilized by viscous forces, yet the flow regime is not viscous dominated but ganglion dynamic. The red oil cluster is the biggest cluster in which the majority of the remained oil is sat. It also bears the maximum potential of being mobilized.

As for the fragmentation, there are two mechanisms acting through the tertiary flooding that affect the value of Euler characteristic; cluster fragmentation and production. The introduction of the polymer to the medium mobilizes the clusters that were trapped since the end of waterflooding. At this initial stage, in the pore-scale, we have meniscus oscillation leading to fluid rearrangement. We see that the major cluster is initially being mobilized as a whole before fragmentation occurs. ***This is a key finding of this thesis because it is the observation of ganglion dynamic flow in the tertiary flooding.*** Clusters become immobile around the oil saturation of 23% for HR/T and 43% for LR/T. In accordance with the literature, we also observed that larger oil clusters are mobilized easier than smaller ones (notice the small blue cluster on the left edge of the sequence pictures in [Figure 65](#)). So, a general suggestion would be: ‘in a secondary phase, waterflood the field with low injection rate while in the tertiary phase, use the high rate.’

At some point, the induced pressure gradients that are acting along the length of the large ganglion break it into smaller disconnected ganglia. This is the point where the continuous reduction in the internal connectivity of a mobile cluster finally reaches a local percolation thresholding value. From the mathematical perspective, this causes the Euler characteristic to increase owing to the increase of zeroth Betti number. For the oil production, however, both zeroth and first Betti number reduce, yet because of the existence of the grains (loops in the clusters) the number of loops that are omitted is more than the number of objects and this is the cause of the increase of χ_N through production.

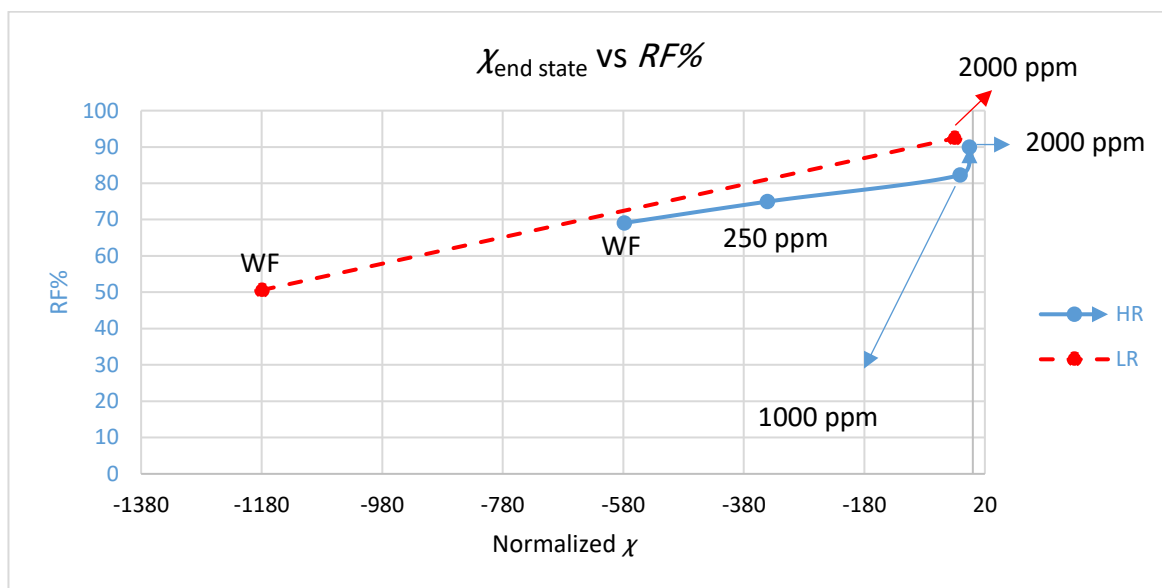


Figure 66: RF vs χ_N . For standard secondary scenarios. As the RF increases, smaller clusters are left into the system that could not be recovered and that is why the Euler characteristic goes up. Notice that the higher the polymer concentration the more disconnected is the oleic phase.

5.4.2 Production Curves

The production curves contain information regarding recovery factors and breakthrough. Although they rarely provide any new information, good agreement was found between literature and observations regarding the ganglion dynamic in tertiary flood (95) (96) and suppression of fingering (2) .

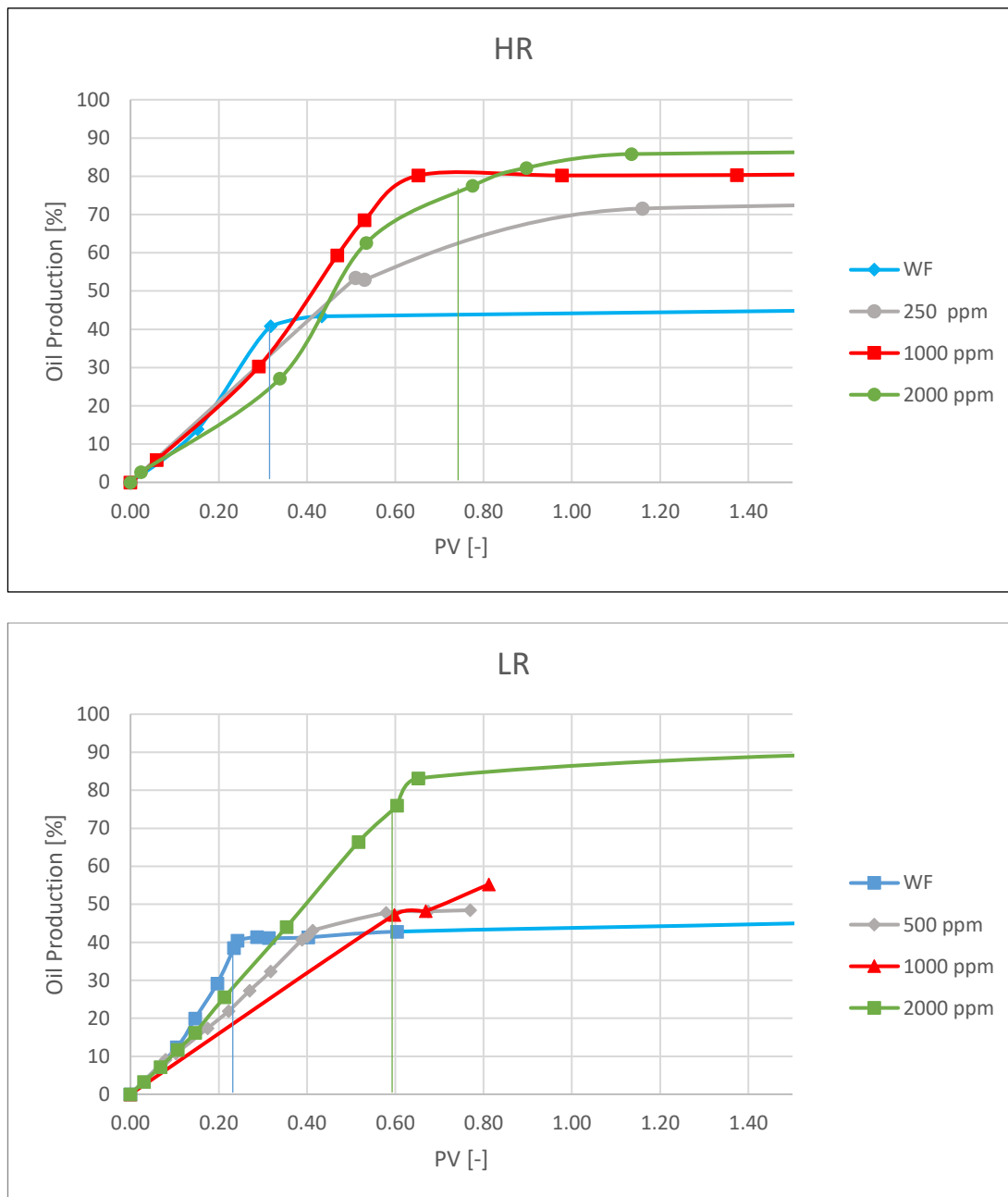


Figure 67: Production curves for (top) HR scenarios and Bottom (LR) scenarios. Notice that the higher the polymer concentration, the slower the breakthrough occurrence and the higher the RF @breakthrough and at the end state. The straight lines are linear interpolation of injected pore volume @breakthrough between the experimental data before and after the breakthrough. The smaller the range of estimation, the more accurate the prediction is obviously. For HR/2000 and LR/2000 this range is [0.53, 0.89] and [0.51-0.65] PV respectively.

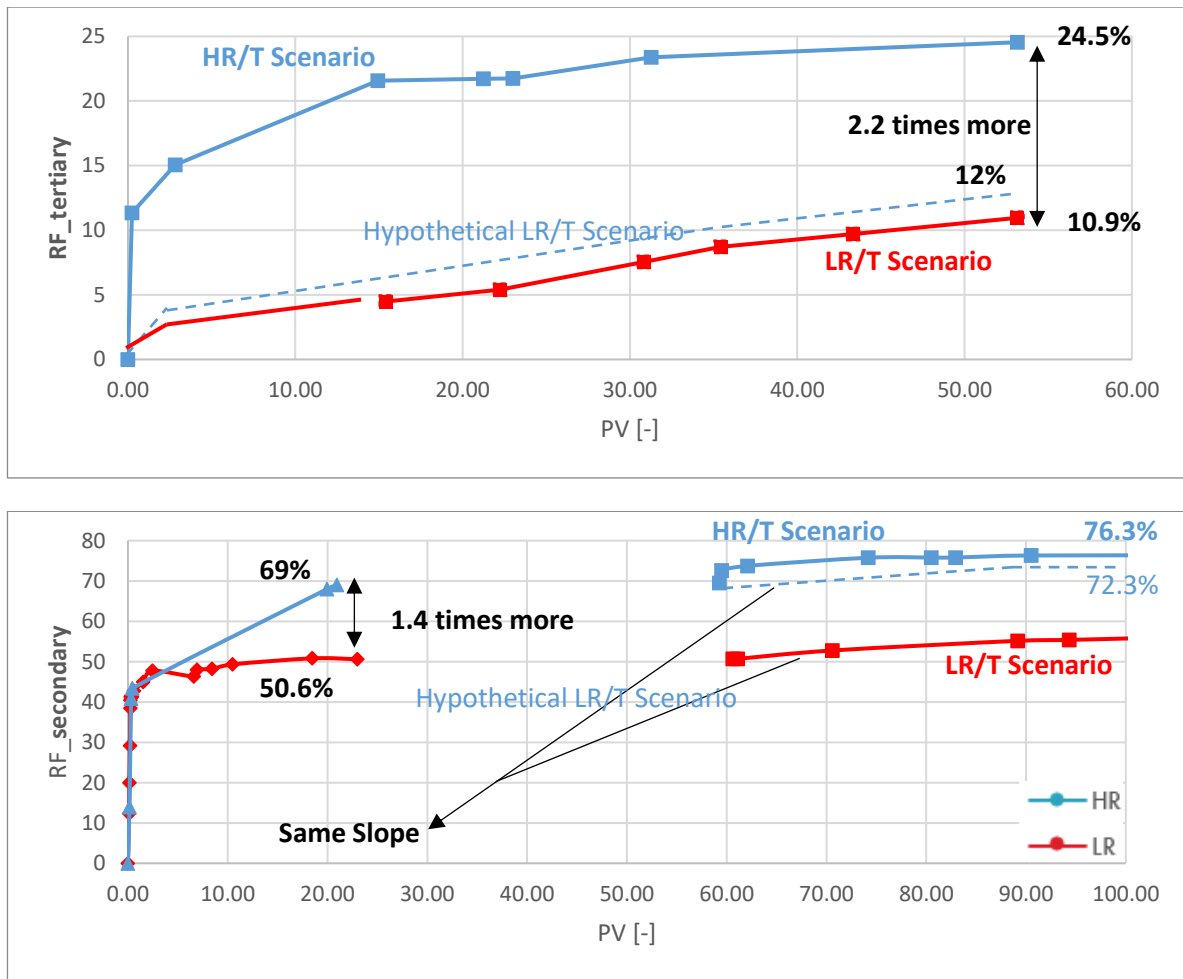


Figure 68: Production curves. Top) Curves are plotted using additionally recovered oil, $RF_{tertiary}$. Bottom) Tertiary following secondary flooding using $RF_{secondary}$ for both EOR phases. We do not have verified data for LR/T within the PV range of [0, 15.4]. A dashed line is then only a sketch of how the curve could look like.

Take a look at [Figure 68](#). The tertiary recovery in HR scenario is almost 2.2 times more than that of LR[0.0019] scenario. But we also know that HR/T starts at the RF of 69%, which is much higher than that of LR/T (50.6). To understand the sensitivity on rate and initial saturation (equal to the ultimate secondary recovery (URF_{sec})), performing a simple calculation is helpful.

We assume that instead of HR[0.01] scenario, a hypothetical LR[0.0019] scenario was conducted with the URF_{sec} 69%, then the slope of the production line ([Figure 68](#): down) for imaginary LR/T should be the same as the real LR scenario that starts at URF_{sec} 50.6%. In this hypothetical case, our HR scenario should have reached the recovery of 72.32% (equal to RF_{tert} 10.4%); however, in reality, it reaches 76.32% (equal to RF_{tert} 24.5%). The difference in tertiary recoveries is 14.1% (58 per cent of ultimate tertiary recovery), which tells us that in the HR scenario, 58% of the total production is owing to the direct influence of high rate. **This supports our previous observation that the ganglion dynamic flow regime governs the production in the HR scenario.**

Core findings and observations of topological analysis.

- ✓ Although within the range of capillary numbers that the experiments were conducted, even low concentrations of polymers maximize the areal sweep, oil production is controlled by mobilization of oleic clusters inside this zone.
- ✓ Cluster fragmentation and oil production have a major effect on the value of Euler characteristics through reducing the oleic phase connectivity.
- ✓ Ganglion dynamic flow was observed in the tertiary flooding.
- ✓ Clusters become immobile around the oil saturation of 23% for HR/T and 43% for LR/T.
- ✓ Xanthan, even in low concentration effectively maximized the areal sweep.
- ✓ The highest ultimate recovery was achieved by experiment LR/2000, although it was very close to the HR/2000.

Chapter 6

6. Conclusion

6.1 Summary

A new quantitative description of the observed flow regimes in secondary flooding was developed by plotting the RF versus the fractal number. The fractal number was extracted using morphological image analysis and it corresponds to the complexity of the advancing front. We have observed that above a critical polymer concentration (a value between 1000 and 2000 [ppm]) the stabilizing effects of polymer agent overcomes the instabilities on the front.

Observations were made concerning the ganglion dynamic in the tertiary flow that was supported by analysing the combination of Euler characteristics and recovery factor. In a related concept, we have seen that in our secondary polymer experiments the oil production will be controlled more by mobilization of oleic clusters inside the swept zone and less by the expansion of areal sweep.

The highest ultimate recovery was achieved by experiment LR/2000 (0.0019 ml/hr, 2000[ppm]), although it was very close to the HR/2000 (0.01 ml/hr, 2000 [ppm]). Clusters became immobile around the oil saturation of 23% for HR/Tertiary and 43% for LR/Tertiary.

Production curves were in good agreement concerning breakthrough and ultimate recovery. We have noticed that xanthan postpones the breakthrough even in low concentration.

Morphological image analysis proved to be extremely useful in obtaining valuable information from the microfluidic experiments. Extraction of interface perimeter as well as areal sweep plus remained oil inside it, and separation of fluid phase from the surrounding pore space are some outstanding examples of its application.

Eventually, the recovery factor is not the only criterion for evaluating displacement. And the EOR screening should not be judged solely based on RF results. This is the case especially after waterflooding.

6.2 Further Work

This thesis offers major opportunities as further works. The bolded ones are:

Modification of Displacement Patterns Plot and Extending It to the 3D

In a generalized version, we can assume that the plot is the zeroth versus first Minkowski functional. With adding another functionality like Euler characteristic as the third axis, we can clearly describe the fluid system in three axes. As for the 2D, more experiments could be conducted so that the borders of the different zones are better depicted. Furthermore, for the current experiments, the extracted images of residual oil plus their respective χ and fractal number are available and ready for further investigation.

After the breakthrough, we can use the fractal number of the interfacial perimeter (including the residual oil). This potentially will depict the ganglion dynamic flow regime.

Characterization of Polymer Retention

Normally we have images shortly before and after the breakthrough. For polymer scenarios with stable frontal advance, initiation of onsets of fingering has been observed close to the outlet. We are not sure if these onsets occur before or after the breakthrough. If it is the former case, the retardation of polymer agents could be the potential reason. For the moment, more data is required to be sure of what is happening.

Moreover, experimental data from two experiments conducted by 250 and 1000 [ppm] Xanthan concentration with 0.0019 ml/hr injection rate are available. Their ultimate recovery factor is considerably higher than what it should be owing to the adsorption of the Xanthan in the medium. The same scenarios should be performed with clean micromodel and their results could be compared to provide further insight into the retention.

Observation of Microemulsion Formation, Capillary Attraction and Repulsion in Menisci

A contact angle alteration has been observed in microfluidics. This does not necessarily mean a wettability alteration scenario but rather a complete displacement of the phase present in the pore. This observation could also be explained by the visco-elastic behaviour of the trapped oil clusters. Anyway, if the experiment takes long enough, the variation in contact angle leads to the wettability not being well defined (78).

These observations were not investigated further due to the time limit to deliver this thesis. However, they are worthy of being investigated.

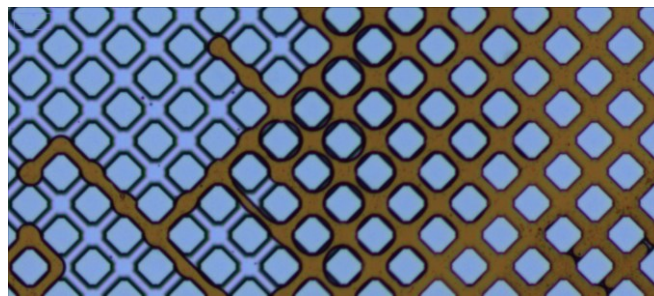


Figure 69: Observation for the formation of the wetting layer for strong water wettability.

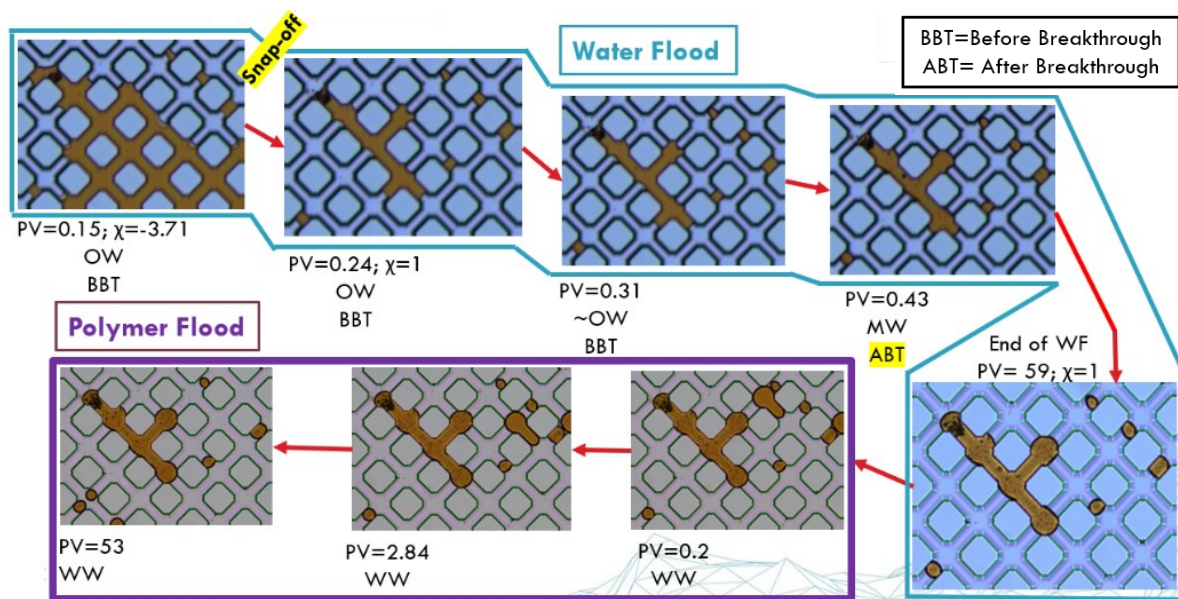


Figure 70: Observation of wettability alteration for HR/WF and subsequent tertiary polymer flood. Notice that according to the contact angle, the wettability changes mainly before the breakthrough. The corresponding χ_N also has been calculated only for the shown cluster.

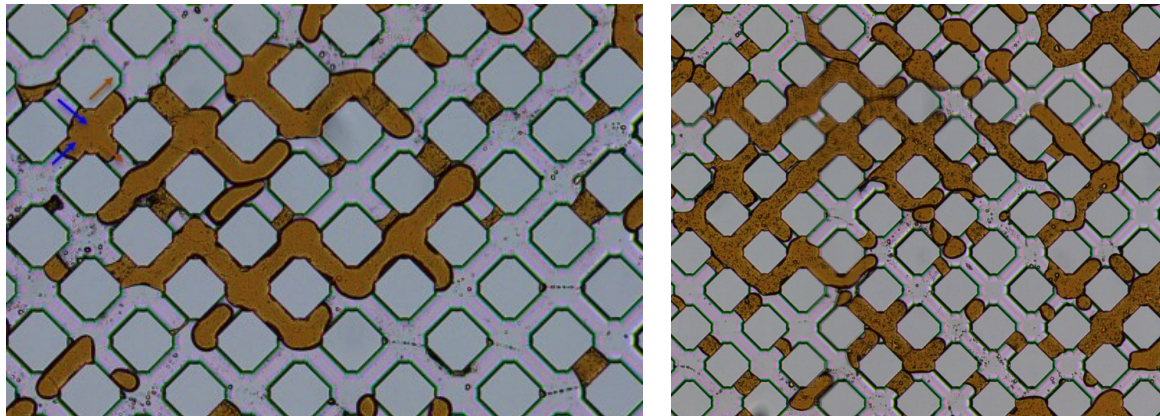


Figure 71: Observation of capillary attraction and repulsion in menisci as well as oil-oil interface

Additionally, provided that contact angles are measured in different experiments, a plot of the degree of heterogeneity versus contact angle could potentially show the displacement regimes (15).

Modelling and Simulation

As already mentioned, by using morphological image analysis, four images could be extracted from every image. For any of these five images, we can calculate a set of $[D, \chi, S]$ (fractal number, Euler characteristic, and saturation). Using these numbers, it should be possible to model the flooding with respect to saturation estimation or breakthrough time provided that we have enough data. A mathematical model can always fit to the set of data and then the question is how to link the model to physics, meaning that we should understand which physical property corresponds to which parameter in the mathematical model. A series of microfluidic experiments with different rates, polymer concentration and pore/throat distribution can be conducted to gather such a data set. A very simple example is given in the following subchapter.

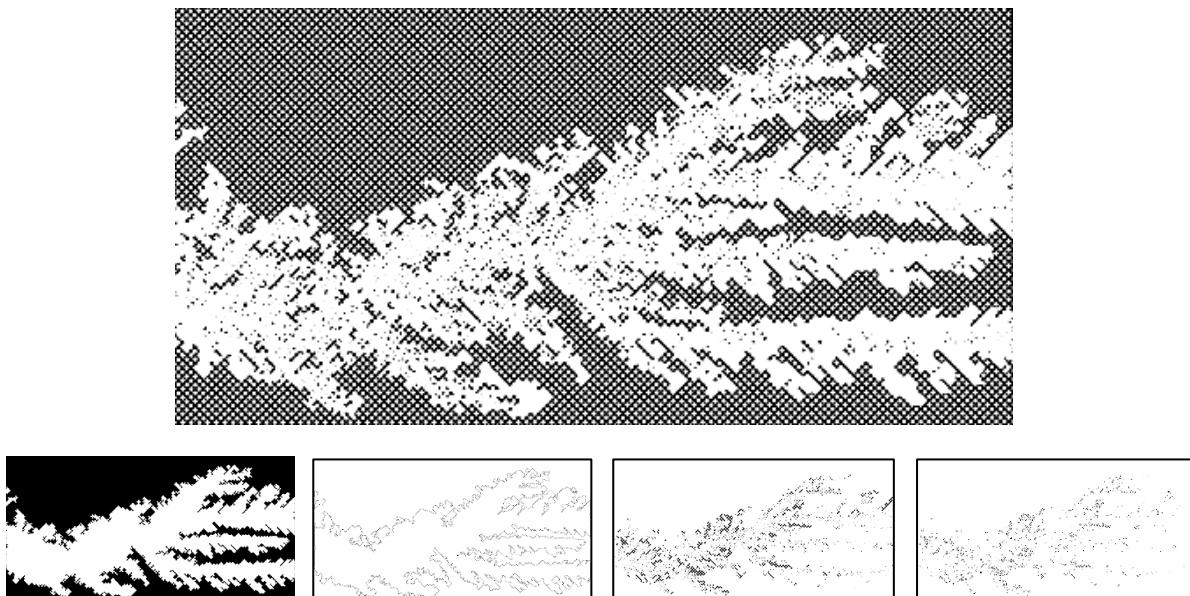


Figure 72: **Top)** the original binary image after opening. **Down)** extraction of the areal sweep, the perimeter of the areal sweep, remained oil inside the areal sweep and its perimeter from left to right, respectively.

Investigation of the Maximum Recovery That Could Be achieved From Secondary Polymer Flooding Using Percolation Theory.

Percolation theory offers a simple tool to understand the flooding process. Blunt has offered an easy model that predicts the saturation of the non-wetting phase at the state of breakthrough (15). Implementing this model on our data will result in a fit of $R^2=0.66$ as being represented below.

**The saturation at which the NW phase first connects across the system(thresholding):
Breakthrough**

L : Porous medium length (sufficiently large)
 d : Dimension of space ; D_{nw} : Fractal dim (NW Phase)
 l : Pore throat length ; S_{nw} : Saturation (NW Phase)

$$S_{nw} \sim \left(\frac{L}{l}\right)^{D_{nw}-d} \int_{r_c}^{r_{max}} \frac{G(r)}{r} dr \sim \left(\frac{L}{l}\right)^{D_{nw}-d}$$

$R^2=66.4\%$

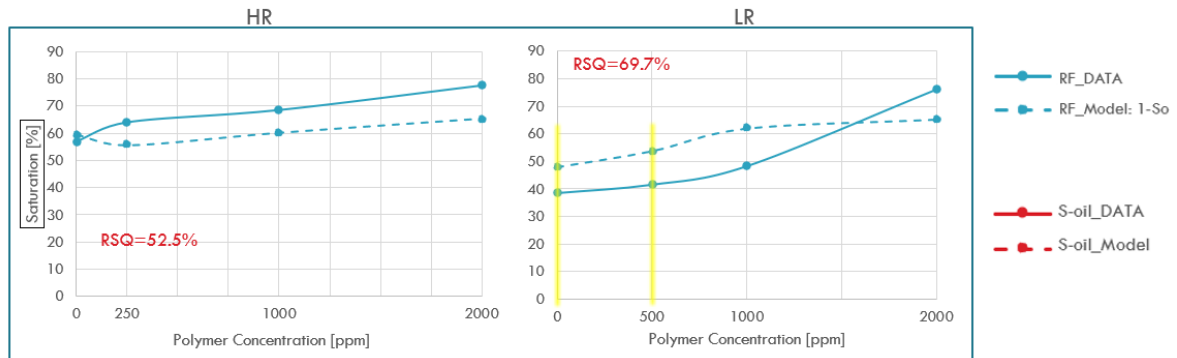


Figure 73: Implementation of Blunt model over the experimental data. Notice that the saturation is governed mainly by porous medium geometry and the deviation from the dimension of the space (which is 2 in microfluidics). The first one is constant. Hence the only parameter controlling the accuracy of the model is the second one. Experiments LR/0 and LR/500 are imbibition and highlighted with the yellow columns.

Now we should be careful not to stretch the application of percolation theory over the point of validity. However, we know that saturation is governed essentially by the combination of areal sweep and remaining oil inside it. $RF = S_{Areal Sweep} - S_{ors}$.

Theoretically, we can predict the saturation accurately provided that:

- 1) We have the correct values for the deviation from the dimension of the space and
- 2) We relate the model to proper physical variables like viscosity ratio ($M\mu$) or even better mobility ratio (but unfortunately, we do not have relative permeabilities) and not directly to polymer concentration nor wettability.

In this sense, by using the experimental recovery factors for different scenarios to calculate the deviation from the following model, we will have the accurate values of the deviation based on the percolation model.

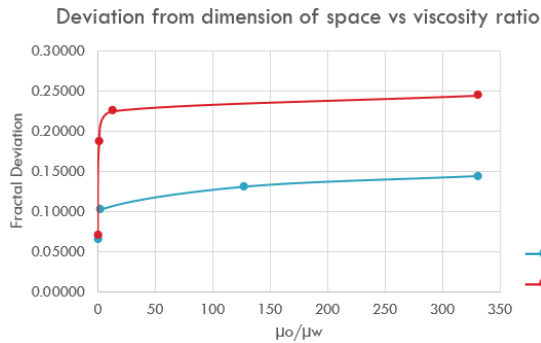
$$S_{BT} \sim \left(\frac{L}{l}\right)^{-D}$$

L : Porous medium length
 l : Pore throat length
 S_{BT} : Saturation @ breakthrough
 D : Deviation from the dimension of space

Equation 13: Percolation model for estimation of the water phase saturation at the breakthrough as a function of porous medium geometry and the deviation from the dimension of the space. The corresponding variables are also stated.

Now if we plot the deviation versus the viscosity ratio for our high rate and low rate scenarios, then it is possible to fit a model into this set of data, that satisfies the two conditions above as well.

Interestingly and yet unsurprisingly, this model will approach a constant value (minimum deviation), if the viscosity ratio approaches zero (very high polymer concentration), indicating that ***no matter how much we increase the polymer concentration, we will not have a recovery factor more than a specific value. For our micromodel and the conducted experiments, this value would ~ 0.89*** as is shown by the following image.



➤ Best mathematical fit:

$$Dev = ae^{bM} + ce^{dM}, \text{ if } M \rightarrow 0, \text{ then } Dev \sim a + c$$

$$\begin{cases} \text{for LR, } D = 0.0297; S_{max@BT} = 0.89 \\ \text{for HR, } D = 0.0507; S_{max@BT} = 0.82 \end{cases}$$

Figure 74: Estimation of the maximum saturation at breakthrough by percolation theory for a uniform micromodel and conducted experiments.

To optimize (or maybe reject) this simple model we need to perform more experiments with a high concentration of Xanthan to obtain more data. Should the model be approved, we can argue that variables used by the model are functions of rate, polymer type and porous medium features. In that sense, its application can be further investigated for the real data field.

Chapter 7

7. References

1. **Thomas, Antonie.** Polymer Flooding. InTech. [Online] 2016. [Cited: 7 February 2019.] <http://dx.doi.org/10.5772/64623>.
2. **Lake, Larry W.** *Enhanced Oil Recovery*. New Jersey : Pearson Education Company, 1989.
3. *Improved Secondary Recovery by Control of Water Mobility* . **Pye, David.J.** 08, s.l. : Society of Petroleum Engineers, 1964, Vol. 16.
4. *Laboratory and field studies of waterflood using polymer solutions to increase oil recoveries*. **Sandiford, B.B.** 08, s.l. : The American Institute of Mining, Metallurgical, and Petroleum Engineers, 1964, Vol. 16.
5. *Rheology and adsorption of aqueous polymer solutions*. **Mungan, N.** 02, s.l. : Petroleum Society of Canada, 1969, Vol. VIII.
6. *Mobility Control With Polymer Solutions* . **Gogarty, W.B.** 02, s.l. : Society of Petroleum Engineers, 1967, Vol. VII.
7. **Hardy, H.H and Beier, Richard. A.** *Fractals in Reservoir Engineering*. Singapore : World Scientific Publishing, 1994.
8. *Fractal patterns from chemical dissolution*. **Daccord, Gerard and Lenormand, Roland.** s.l. : Nature, 1987, Vol. 325.
9. *Invasion Percolation in an Etched Network: Measurement of a Fractal Dimension*. **Lenormand, Roland and Zarcone, Cesar.** 20, Toulouse : PHYSICAL REVIEW LETTERS, 1984, Vol. 54.
10. *Percolation Theory of Two-Phase Relative Permeability*. **Helba, H.H, et al.** 01, s.l. : Society of Petroleum Engineers, 1992, Vol. VII.
11. **Lenormand, R.** Fractals and Porous Media. [book auth.] Alberto Carpinteri and Francesco Mainardi. *Fractals and fractional calculus in continuum mechanics*. New York : Springer-Verlag Wien GmbH, 1997.
12. **Vogel, Hans.org.** Topological Characterization of Porous Media. [ed.] K Mecke and D Stoyan. *Morphology of Condensed Matter. Lecture Notes in Physics*. Heidelberg : Springer, 2002, pp. 75-92.
13. **Ott, Holger, et al.** Fluid-phase topology of complex displacements in porous media. *PHYSICAL REVIEW RESEARCH* . 2020, Vol. 2, 2.
14. *Porous Media Characterization Using Minkowski Functionals: Theories, Applications and Future Directions*. **Armstrong, Ryan.T, et al.** 2018, Transport in Porous Media, pp. 1-34.
15. **Blunt, Martin.J.** *Multiphase Flow in Permeable Media a Pore-Sclae Perspective*. New York : Cambridge University Press, 2017.

16. **Littmann, Wolfgang.** *Polymer Flooding*. s.l. : Elsevier Science & Technology, 1988. 0-444-43001-6.
17. **Satter, Abdus, Iqbal, Ghulam.M and Buchwalter, James.L.** *Practical enhanced reservoir engineering : assisted with simulation software*. Tulsa, Oklahoma : PennWell Corp, 2008. 978-1-59370-056-0.
18. **Lorenzo, Gabriel, et al.** STUDYING THE ROLE OF XANTHAN GUM UPON THE RHEOLOGY AND STABILITY OF OIL/WATER EMULSIONS. [ed.] Michelle Butler. *Xanthan Gum Applications and Research Studies*. New York : Nova, 2016, pp. 111-145.
19. **Willhite, Paul.G and Green, Don.W.** *Enhanced Oil Recovery*. Richardson : Society of Petroleum Engineers, 1998.
20. *The molecular size and shape of xanthan, xylinan, bronchial mucin, alginate, and amylose as revealed by electron microscopy.* **Stokke, Bjørn T, et al.** 1987, Carbohydrate Research, Vol. 160, pp. 13-28.
21. *MOLECULAR WEIGHT OF XANTHAN POLYSACCHARIDE.* **Holzwarth, G. 1,** 1978, Carbohydrate Research, Vol. 66, pp. 173-186.
22. *Adsorption/desorption of polymers from Saudi Arabian limestone.* **Celik, M.S, Ahmad, S and Al-Hashim, Hasan Salman.** 1991, Journal of Petroleum Science and Engineering, Vol. VI, pp. 213-223.
23. *Xanthan.* **Born, Karin, Langendorff, Virginie and Boulenguer, Patrick.** 2013, Biopolymers, Vol. V, pp. 259-269.
24. *A Rheological Study of Xanthan Polymer for Enhanced Oil Recovery.* **Ghoumrassi-Barr, Sofia and Djamel, Aliouche.** 8, s.l. : Journal of Macromolecular Science, Part B: Physics, 2016, Vol. 55. 1525-609X.
25. **Willhite, G.P and Dominguez, J .G.** MECHANISMS OF POLYMER RETENTION IN POROUS MEDIA. [ed.] D.O Shah and R.S Schechter. *Improved Oil Recovery by Surfactant and Polymer Flooding*. New York : Academic Press, INC, 1977, pp. 511-544.
26. *Microvisual investigation of polymer retention on the homogeneous pore network of a micromodel.* **Yun, W and Kovscek, A.R.** 2015, Petroleum Science and Engineering, pp. 115-127.
27. *Qualitative and Quantitative Evaluation of Permeability Changes during EOR Polymer Flooding Using Micromodels.* **Knobloch, Lucas O, et al.** 06, 2018, World Journal of Engineering and Technology, pp. 332-349.
28. *An Enhanced Oil Recovery Micromodel Study with Associative and Conventional Polymers.* **Leoben : University of Leoben, 2008.**
29. **Aghamir-Baha, Saman.** *MEASUREMENT OF POLYMER CONCENTRATION AND OPTIMIZATION OF SLUDGE DEWATERING USING UV-VIS SPECTROSCOPY.* Ottawa : Carleton University, 2014.
30. *Synthesis and Characterization of Polyacrylamide Crosslinked Copolymer for Enhanced Oil Recovery and Rock Wettability Alteration.* **El Hoshoudy, A, et al.** 04, s.l. : International Journal of Oil, Gas and Coal Engineering, 2015, Vol. III.

31. *Hydrophobically associating polymers for enhanced oil recovery - Part A: A review on the effects of some key reservoir conditions*. Afolabi, Richard.O, et al. s.l. : Journal of Petroleum Science and Engineering, 2019, Vol. 180.
32. JIANG, L and KORIVI, N.S. *Microfluidics: technologies and applications*. [ed.] Martin Feldman. *Nanolithography The Art of Fabricating Nanoelectronic and Nanophotonic Devices and Systems*. s.l. : Woodhead Publishing Limited, 2014, pp. 424-443.
33. Nasiri, Arash. *Measuring Particle Velocity Field in Pore Scale (Using Fluorescence)*. Leoben : DPE Department Petroleum Engineering, 2018.
34. *Invasion percolation: a new form of percolation theory*. Wilkinson, D and Willemsen, J.F. 14, Ridgefield : Journal of Physics A: Mathematical and General, 1983, Vol. 16.
35. N.K, Karadimitriou and S.M, Hassanizadeh. A Review of Micromodels and Their Use in Two-Phase Flow Models. *Vadose Zone Journal*. 7 September 2012, p. 21.
36. F.AL, Dullien. *Porous Media: Fluid Transport and Pore Structure*. 2nd. San Diego, California : Academic Press Inc., 1991.
37. Solomon, Chris and Breckon, Toby. *Fundamentals of Digital Image Processing A Practical Approach with Examples in Matlab*. s.l. : Wiley-Blackwell, 2010.
38. Borji, Mostafa. *Alkali-based Displacement Processes in Microfluidic Experiments: Application to the Matzen Oil Field*. Leoben : Montan University Leoben, 2017.
39. Kharrat, Ahmad. *Alkali-based Displacement Processes in Microfluidic Experiments: Advanced Statistical Analyses*. Leoben : Montan University Leoben, 2018.
40. Ferreira, Tiago and Rasband, Wayne. *ImageJ User Guid*. s.l. : National Institutes of Health, 2012.
41. Ohser, Joachim and Katja, Schladitz. *Image Processing. 3D Images of Materials Structures: Processing and Analysis*. s.l. : Wiley-VCH Verlag GmbH & Co. KGaA, 2009, pp. 79-148.
42. Karperien, A. *The Fraclac Guide*. [Online] 2012. [Cited: 16 April 2019.] <https://imagej.nih.gov/ij/plugins/fraclac/FLHelp/StartUpScreen.htm>.
43. *Globally optimal stitching of tiled 3D microscopic image acquisitions*. Preibisch, Stephan, Saalfeld, Stephan and Tomancak, Pavel. 11, 2009, *BIOINFORMATICS* , Vol. 25, pp. 1463-1465.
44. *Biomedical Image Processing*. Sternberg, Stanley.R. 1983, *Computer*, Vol. 16, pp. 22-34.
45. MCCleary, John. *A First Course in Topology: Continuity and Dimension*. s.l. : American Mathematical Society, 2006.
46. *Pore-scale displacement mechanisms as a source of hysteresis for two-phase flow in porous media*. Schülter, S, et al. 3, s.l. : *Water resource research*, 2016, Vol. 52.

47. *Dependence of Residual Nonwetting Liquid on Pore Topology*. Pathak, Prabodh, Davis, Ted.H and Scriven, L.E. 1982, Society of Petroleum Engineers.
48. *Impact of Pore Connectivity and Topology on Gas Productivity in Barnett and Haynesville Shale Plays*. Davudov, Davud, Ghanbarnezhad Moghanloo, Rouzbeh and Yuan, Bin. San Antonio : Unconventional Resources Technology Conference (URTeC), 2016.
49. *Alterations in Pore Topology of Organic-Rich Shale Samples Due to the Removal of Dead Oil, Bitumen, and Kerogen*. Ojha, Shiv.P, et al. 2017, Society of Petrophysicists and Well-Log Analysts, Vol. 58.
50. Bazaikin, Ya, et al. Scale dependency of pore space topology and transport properties of sandstone CT-scans. *SEG International Exposition and 86th Annual Meeting*. September 2016, pp. 3148-3153.
51. Ott, Holger. *CO₂-BRINE PRIMARY DISPLACEMENT IN SALINE AQUIFERS Experiments, Simulations and Concepts*. Aachen : RWTH Aachen University, 2015.
52. Hunt, allen and Ewing, Robert. *Percolation Theory for Flow in Porous Media*. s.l. : Springer, 2009.
53. Schmähling, Jochen. *Statistical characterization of technical*. Heidelberg : Heidelberg University, 2006.
54. *Quantification of Connectivity in Cancellous Bone, with Special Emphasis on 3-D Reconstructions*. ODGAARD, A and GUNDERSEN, H.J.G. 2, 1993, Bone, Vol. 14, pp. 173-182.
55. *Fluid Topology in Pore Scale Two-Phase Flow Imaged by Synchrotron X-ray Microtomography*. Khanamiri, Hosseinzade Hamid and Torsaeter, Ole. 3, s.l. : Water Resources Research, 2018, Vol. 54.
56. *From connected pathway flow to ganglion dynamics*. Rucker, Maya, et al. 10, 2015, Geophysical Research Letters banner, Vol. 42, pp. 3888-3894.
57. Ott, Holger. Geothermal RE/Storage. Sequestration & Geothermal: Subsurface Processes. Leoben : Montan University leoben, 2018.
58. *Introduction to percolation theory*. Stauffer, Dietrich and Aharony, Amnon. West Sussex : Taylor & Francis , 1994. 9780748400270.
59. Weisstein, Eric. Dimension. *Mathworld*. [Online] 03 March 2014. <http://mathworld.wolfram.com/Dimension.html>.
60. Devaney, Robert.L. Fractal Dimension. *BU Math Home Page* . [Online] 2 April 1995. <http://math.bu.edu/DYSYS/chaos-game/node6.html>.
61. Mandelbrot, Benoit.B. *The fractal geometry of nature* . s.l. : Henry Holt and Company, 1983.
62. Dullien, F.A.L. *Porous Media, Second Edition: Fluid Transport and Pore Structure*. s.l. : Academic Press , 1991. 9780122236518 .

63. *Capillary displacement and percolation in porous media*. Chandler, Richard, et al. s.l. : Fluid Mechanics, 1982, Vol. 119.
64. *Capillary Fingering: Percolation and Fractal Dimension*. Lenormand. Saint Etienne : Transport in Porous Media, 1989, Vol. IV.
65. *A relationship between the fractal dimension and scaling groups of unstable miscible displacement*. Gharbi, R.B.C, Qasem, F and Peters, E.J. s.l. : Experiments in fluids, 2001, Vol. 31.
66. Carpinteri, A and Mainardi, F. *Fractals and Fractional Calculus in Continuum Mechanics*. New York : Springer-Verlag Wien, 1997. 978-3-7091-2664-6.
67. Society of Petroleum Engineers. *Slideshare*. [Online] 31 12 2018. [Cited: 05 09 2019.] https://www.slideshare.net/SPEupdates/using-fractals-to-determine-a-reservoirs-hydrocarbon-distribution?qid=6d81e199-c6d1-47b0-aa36-19b9ca6d13a0&v=&b=&from_search=2.
68. *Quantitative Description for the Heterogeneity of Pore Structure by Using Mercury Capillary Pressure Curves* . Pingping, Shen, Li, Kevin and Jia, Fenshu. Beijing : Society of Petroleum Engineers, 1995.
69. *Flow Mechanisms, Relative Permeabilities, and Coupling Effects in Steady-State Two-Phase Flow through Porous Media. The Case of Strong Wettability*. Avraam, D.G and Payatakes, A.C. 3, s.l. : Industrial & Engineering Chemistry Research, 1999, Vol. 38.
70. *Methods of Measuring the Concentration of Wealth*. Lorenz, M.O. 70, s.l. : American Statistical Association, 1905, Vol. 9.
71. *Power-Law Distributions in Empirical Data*. Clauset, Aaron, Shalizi, Cosma.Rohilla and Newman, M.E.J. IV, s.l. : Society for Industrial and applied Mathematics, 2009, Vol. 51.
72. *Percolation effects in immiscible displacement*. Wilkinson, David. II, s.l. : Physical Review A, 1986, Vol. 34.
73. *Pore scale micro computed tomography imageing: Nonwetting phase cluster size distribution during drainage and imbibition*. Georgiadis, Apostolos, et al. 3, s.l. : Physical Review, 2013, Vol. 88.
74. Ringrose, Philip and Bentley, Mark. *Reservoir Model Design A Practitioner's Guide*. s.l. : Springer, 2015. 978-94-007-5497-3.
75. *Real-time 3D imaging of Haines jumps in porous media flow*. Berg, Steffen, et al. 10, s.l. : Proceedings of the National Academy of Sciences, 2013, Vol. 110. 1091-6490.
76. Bear, Jacob. *Dynamics of Fluids in Porous Media*. New York : Dover Publications , 1972. 978-87-630-0230-1 .
77. *The penetration of a fluid into a porous medium or Hele-Shaw cell containing a more viscous liquid*. Saffman, Philip.G and Taylor, Geoffrey.I. 1242, s.l. : Royal Society, 1958, Vol. 242. 2053-9169.

78. *Numerical models and experiments on immiscible displacements in porous media*. Lenormand, Roland, Touboul, Eric and Zarcone, Cesar. s.l. : Journal of Fluid Mechanics, 1988, Vol. 189.
79. *On Capillary Slowdown of Viscous Fingering in Immiscible Displacement in Porous Media*. Daripa, Prabir and Pasa, G. s.l. : Transport in porous media, 2008, Vol. 75.
80. *Viscous Fingering in porous Media*. Homsy, G.M. s.l. : Annual Reviews, 1987, Vol. 19.
81. *Dimensional analysis of pore scale and field scale immiscible displacement*. Hilfer, R and Ören, P.E. s.l. : Transport in Porous Media, 1996, Vol. 22.
82. *Stability of miscible displacement in porous media: Rectilinear flow*. Tan, C.T and Homsy, G.M. 11, s.l. : Physics of Fluids, 1986, Vol. 29. 10.1063/1.865832 .
83. *A Method for Predicting the Performance of Unstable Miscible Displacement in Heterogeneous Media* . Koval, E.J. 2, s.l. : Society of Petroleum Engineers, 1963, Vol. 3.
84. *Linear stability of radial displacements in porous media: Influence of velocity-induced dispersion and concentration-dependent diffusion*. Riaz, Amir, Pankiewitz, Christian and Meidburg, Eckart. s.l. : AIP publishing: Physics of fluids, 2004, Vol. 16. 10.1063/1.1775431.
85. *Linear stability analysis of immiscible two-phase flow in porous media with capillary dispersion and density variation*. Riaz, Amir and Tchelepi, Hamdi.A. s.l. : API Publishing: Physics of fluid, 2004, Vol. 16. 10.1063/1.1812511.
86. Micronit. Micronit. *Mincronit microfluidics*. [Online] Micronit Microtechnologies B.V, 2017. [Cited: 05 February 2020.] <https://store.micronit.com/microfluidic-chips/3-pack-eor-chips-uniform-network>.
87. *Leica Microsystems*. [Online] Leica Microsystems, 2020. [Cited: 13 Feb 2020.] <https://www.leica-microsystems.com/>.
88. *Laboratory Investigation of the Effect of Brine Composition on Polymer Solutions-Part 2: Xanthan Gum (XG) Case*. Nashawi, Ibrahim S. 1991, Society of Petroleum Engineers.
89. Jungbunzlauer. *www.jungbunzlauer.com*. [Online] 20 September 2018. https://www.jungbunzlauer.com/fileadmin/content/_PDF/PRINT_PROJECTS/Folder/JBL_FO_Xanthan_Gum_2017-043.pdf.
90. Particle Analyser. *bonej.org*. [Online] 29 May 2020. [Cited: 18 June 2020.] <https://bonej.org/particles>.
91. *Euler Number and Connectivity Indexes of a Three Dimensional Digital Picture*. Toriwaki, Junichiro and Yonekura, Tatsushiro. s.l. : Forma, 2002, Vol. 17.
92. *Power-law distributions in binned empirical data*. Virkar, Yogesh and Clauset, Aaron. 1, s.l. : Annals of Applied Statistics, 2014, Vol. 8. arXiv:1208.3524.
93. Darby, Ronald. *Chemical Engineering Fluid Mechanics* . s.l. : Marcel Dekker, 2001. 9780585418971.

94. Arnold, Pit. *Experimental investigation of interfacial tension for alkaline flooding*. Leoben : Montan University of Leoben, 2018.
95. *Dynamics of Oil Ganglia During Immiscible Displacement in Water-Wet Porous Media*. Payatakes, A.C. 1, s.l. : Annual Review of Fluid Mechanics, 1982, Vol. 14.
96. Qingjie, Liu, Pingping, Shen and YuShu, Wu. *Characterizing Two-Phase Flow Relative Permeabilities in Chemical Flooding Using a Pore-Scale Network Model*. Berkeley, California : Lawrence Berkeley National Laboratory, 2004. 10.2172/929035.
97. *Dependence of Polymer Retention on Flow Rate*. Marker, John M. 11, 1973, Journal of Petroleum Technology, Vol. 25, pp. 1307-1308.
98. *Polymer/Surfactant Transport in Micellar Flooding* . C.S, Chiou and Kallerhals, G.E. 05, 1981, Society of Petroleum Engineers, Vol. 21, pp. 603-612.
99. *Polymer Retention in Porous Media*. Huh, C, Lange, E.A and Cannella, W.G. 1990, Society of Petroleum Engineers, pp. 567-586.
100. *Polymer Retention and Adsorption in the Flow of Polymer Solutions Through Porous Media* . Cohen, Y. 02, 1986, SPE Reservoir Engineering, Vol. 1, pp. 113-118.
101. *Experimental and Theoretical Study of Polymer Flow in Porous Media* . Sorbie, K.S, Parker, A and Clifford, PJ. 03, 1987, Society of Petroleum Engineers, Vol. 2, pp. 281-304.
102. Sorbie, K.S. *Polymer-Improved Oil Recovery*. 1st. Edinburgh : Springer Science; Business Media, LLC, 1991.
103. *Novel Insight into Polymer Injectivity for Polymer Flooding*. Yerramilli, Sanjay S and Yerramilli, Ramesh C. 2013, Society of Petroleum Engineers, p. 23.
104. Chauveteau, G and Lecourtier, J. Propagation of Polymer Slugs Through Adsorbent Porous Media. *ACS Annual Meeting*. 16-18 April 1985.
105. Lecourtier, J and Chauveteau, G. Adsorption des Polyacrylamides et du Xanthane sur des Surfaces Minerales. *European EOR Symposium*. 16-18 April 1985.
106. *Field vs. Laboratory Polymer-Retention Values for a Polymer Flood in the Tambaredjo Field* . Manichand, Renuka N and Seright, Randal. 03, 2014, Society of Petroleum Engineers, Vol. 17, pp. 1-12.
107. Vollmert, B. *Grundriss der Makromolekularen Chemie*. 1st. Berlin : SPRINGER-VERLAG BERLIN HEIDELBERG GMBH, 1962.
108. Sheng, James J. *Modern Chemical Enhanced Oil Recovery theory and Practice*. 1st. Burlington, Vermont : Elsevier, 2011.
109. *The Role of Adsorption in Polymer Propagation Through Reservoir Rocks* . Zaitoun, A and Kohler, N. 1987, Society of Petroleum Engineers, pp. 327-340.

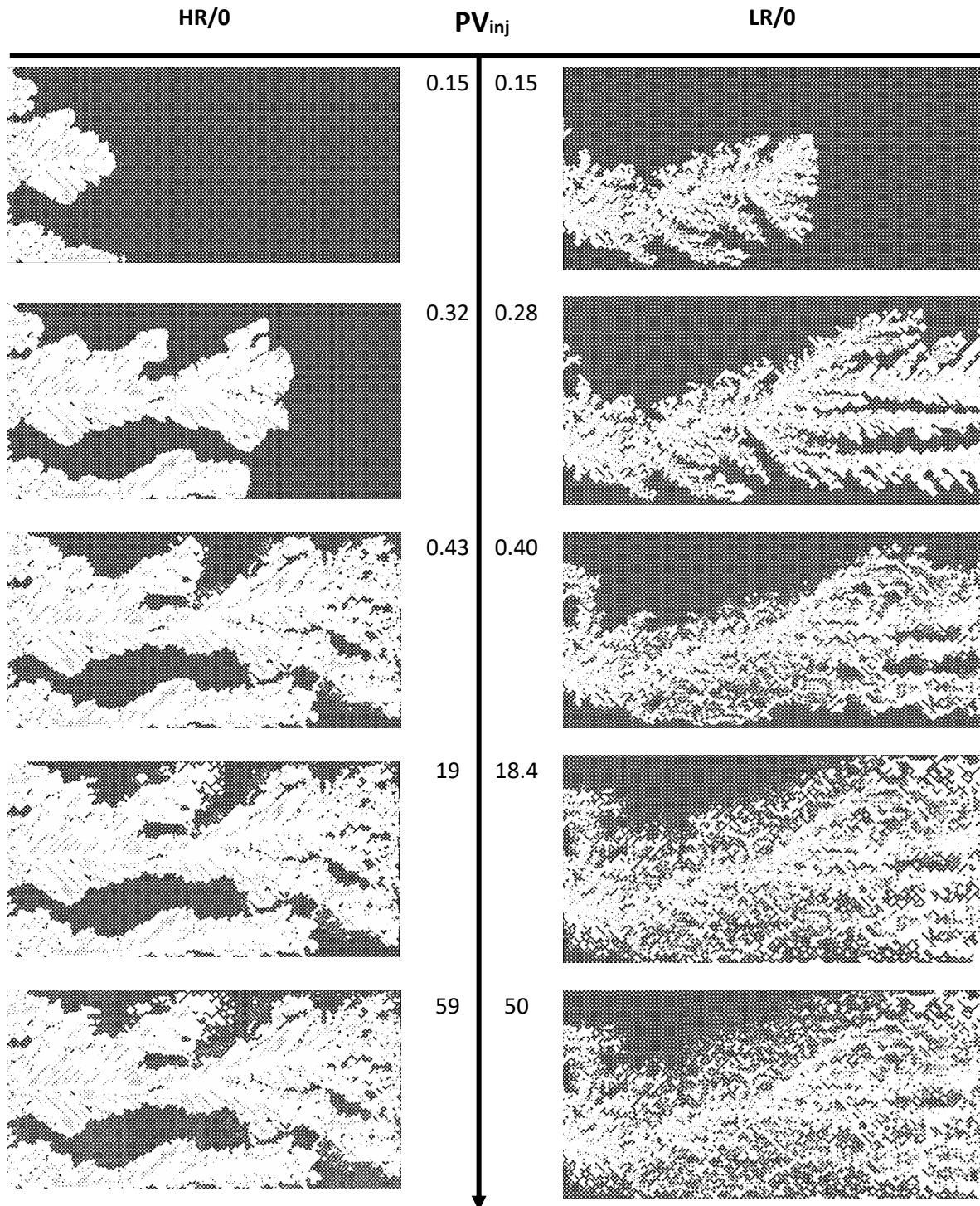
110. *Review on Polymer Flooding: Rheology, Adsorption, Stability, and Field Applications of Various Polymer Systems*. Kamal, Muhammad S, Ibelwaleed, A Hussein and Sultan, Abdullah. 3, 2015, Polymer Reviews, Vol. 55, pp. 491-530.
111. *Estimation of Polymer Retention from Extended Injectivity Test*. Juri, J.E, et al. 2015, Society of Petroleum Engineers.
112. Zhang, Guoyin and Seright, Randall. *Effect of Concentration on HPAM Retention in Porous Media*. s.l. : Society of Petroleum Engineers, 2014.
113. Boekhout, S.G. *DEVELOPING A WORKFLOW FOR A STUDY OF POLYMER FLOODING IN HETEROGENEOUS RESERVOIRS*. Delf : Delft University of Technology, 2015.
114. *Effect of Adsorbed Water on Wetting Properties of Borosilicate Glass, Quartz, and Sapphire*. K.Bernett, Marianne and Zisman, W.A. 03, s.l. : Journal of Colloid and Interface Science, 1968, Vol. 29.
115. *Quantification of Connectivity in Cancellous Bone, with Special Emphasis on 3-D Reconstructions*. Odghaard, A and Gundersen, H.J.G. 07 August 1992, Bone, pp. 173-182.
116. *Viscous Fingering in Heterogeneous Porous Media* . Araktingi, U.G and Orr, Franklin. 01, s.l. : Society of Petroleum Engineers, 1993, Vol. 1. doi:10.2118/18095-PA.

Chapter 8

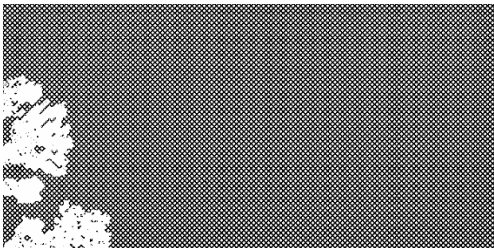
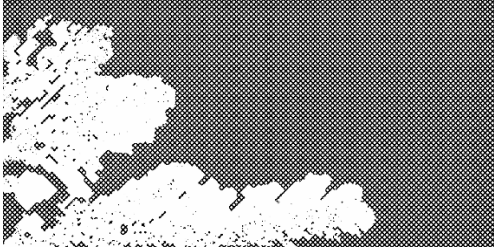
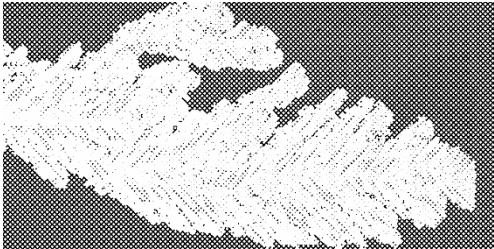
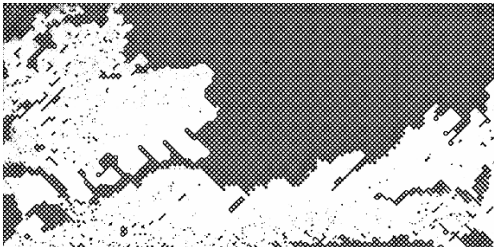
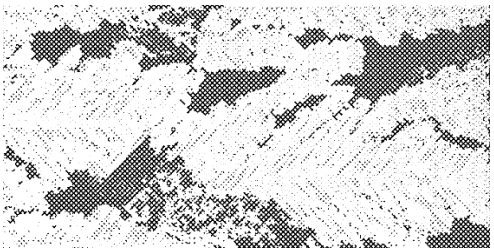
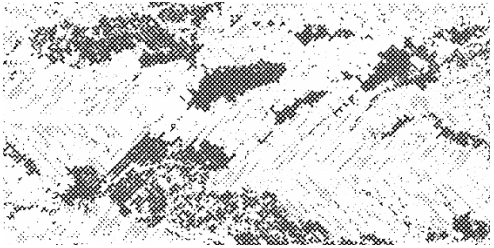
8. Appendix

8.1 Visualization of All Scenarios

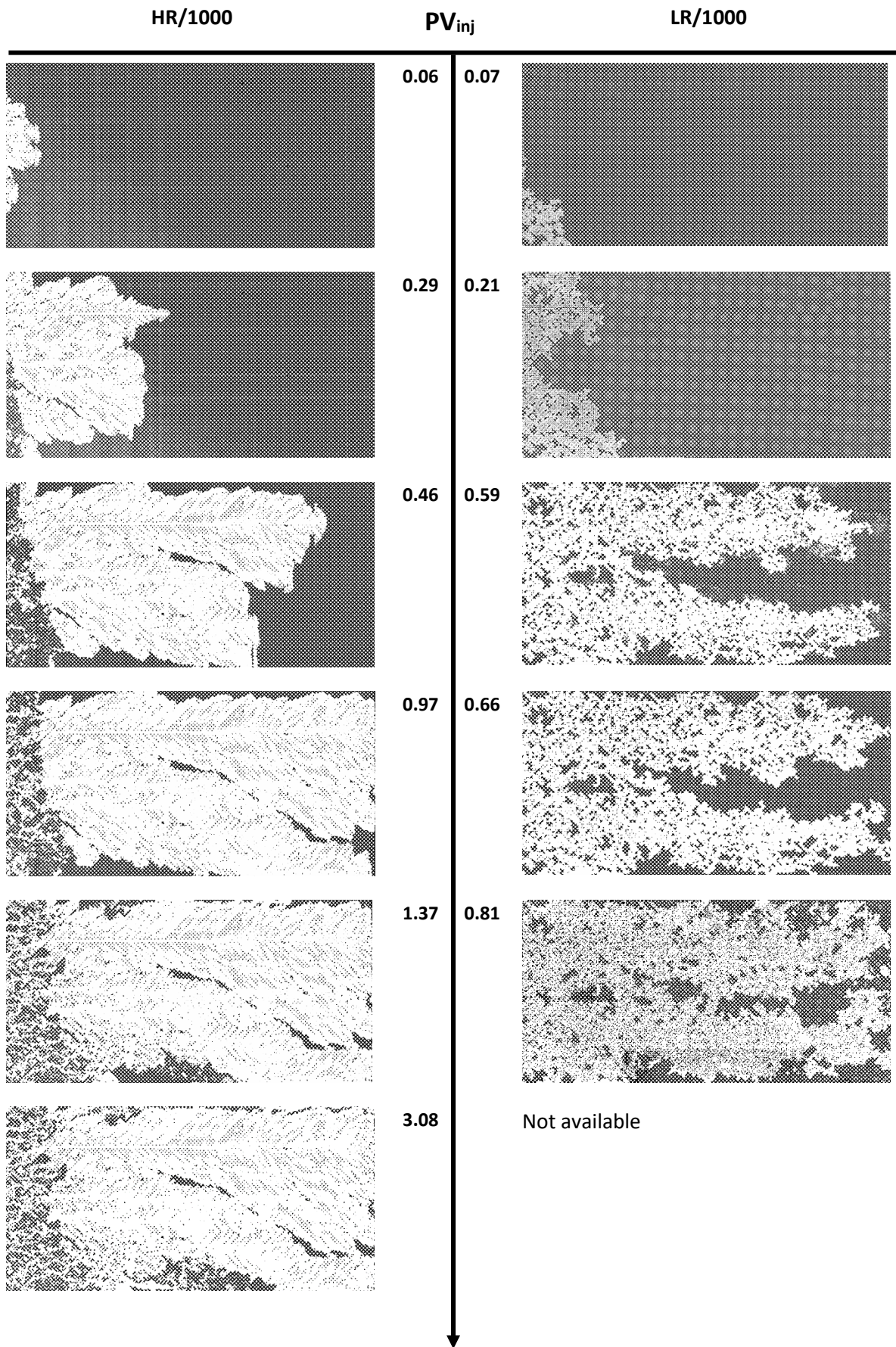
Waterflood Scenarios



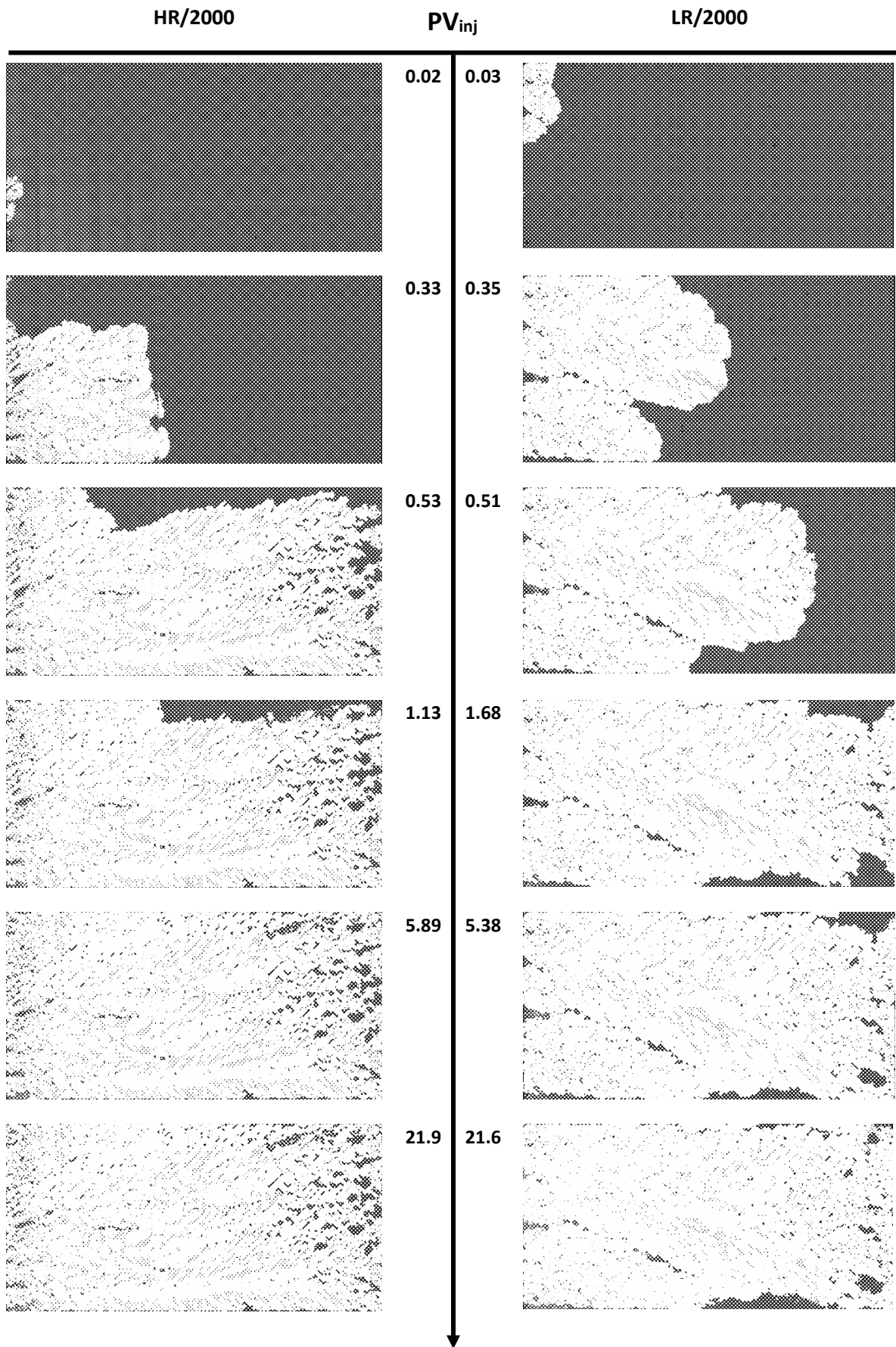
Polymer Floods HR/250 And LR/500 Scenarios

HR/250	PV_{inj}	LR/500
Not available	0.1	
Not available	0.32	
	0.50	0.57
Not available	0.77	
	1.12	Not available
	47.1	Not available

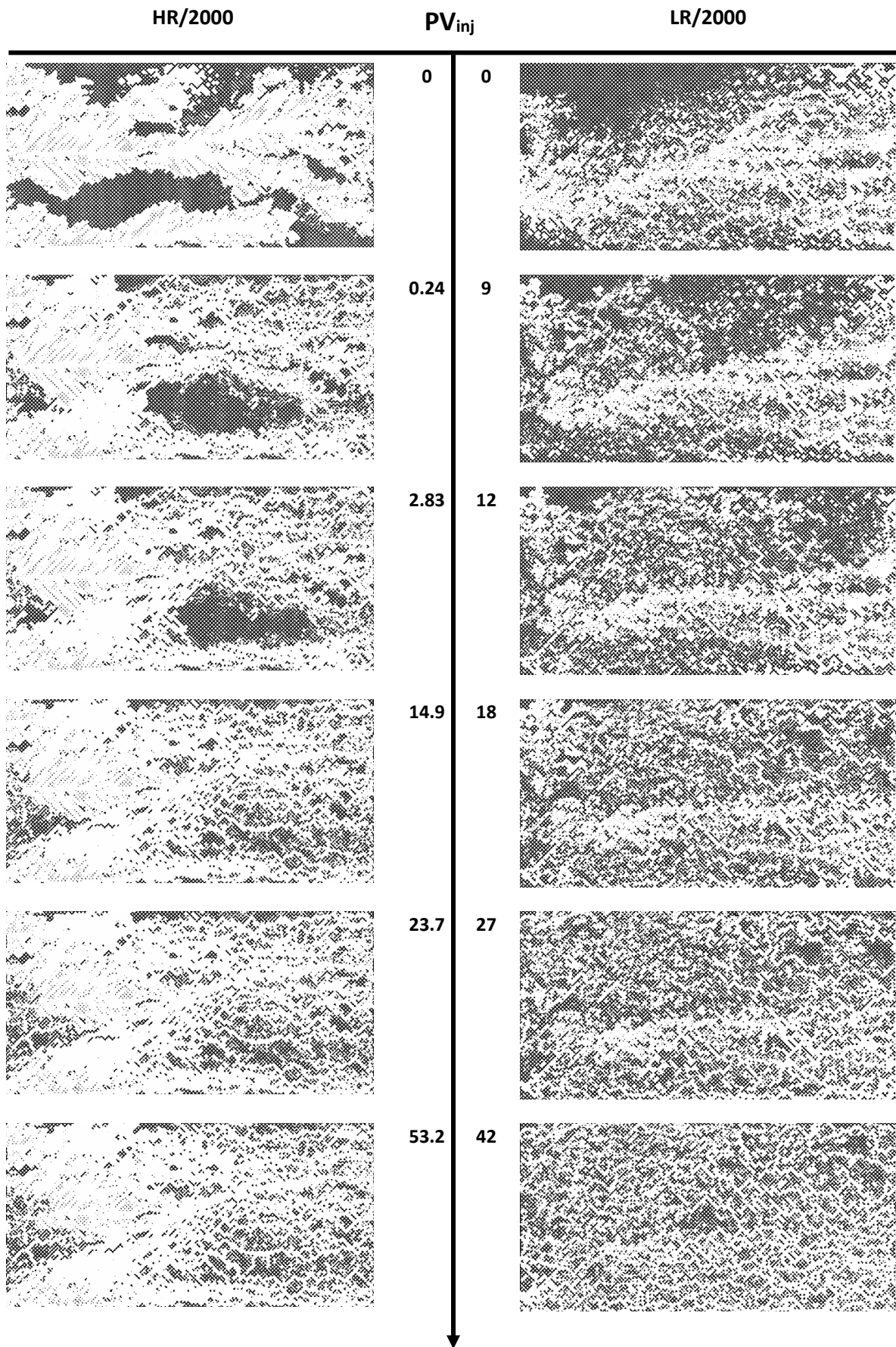
Polymer Floods 1000 Scenarios



Polymer Flood 2000 Scenarios

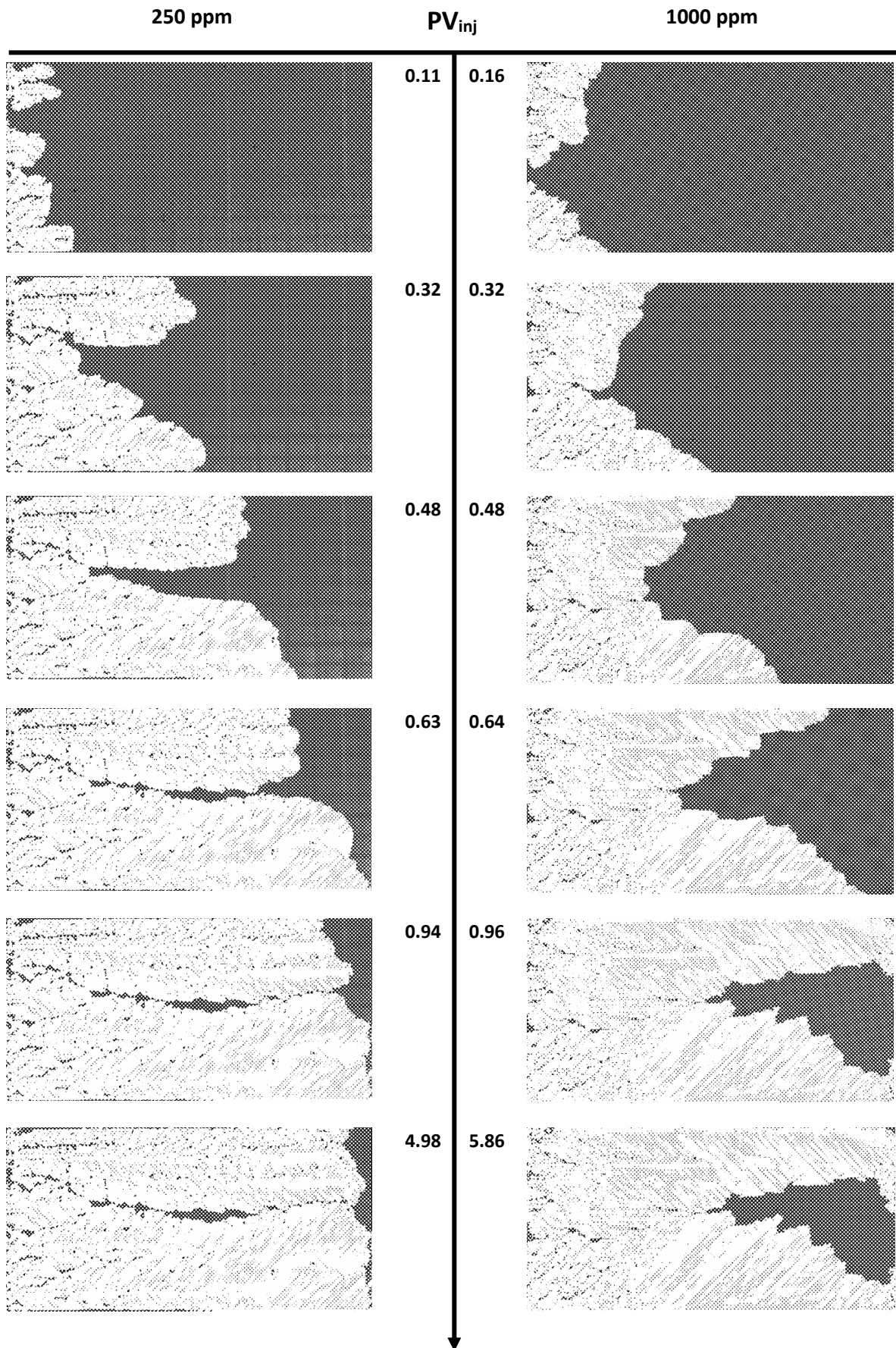


Tertiary flood Scenarios

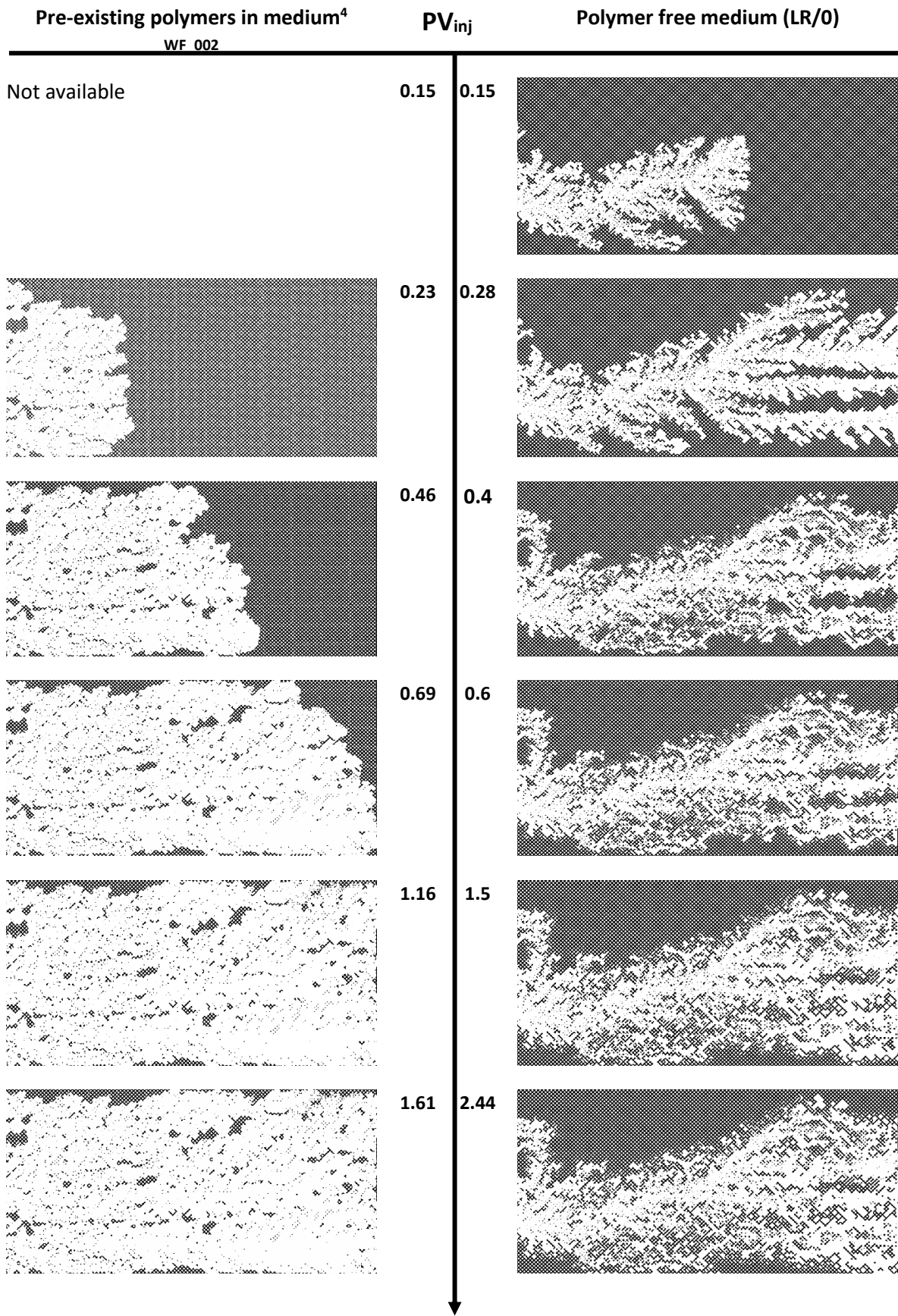


8.2 Polymer Retention Experiments

Flooding Experiments of POL_011(0.0019/250 ppm) and POL_010 (0.0019/1000 ppm)



Comparison Between Waterfloods at Low Rate



⁴ The micromodel was initially saturated with polymer solution then it was cleaned (not systematically so that polymer could remain in the porous medium) and then saturated with oil before conducting the WF.

